

Supporting Information

Promoting photoswitching in mismatching mixed-linker multivariate Zr6 MOFs.

*Carmen Rosales-Martínez, Diego López-Alcalá, Marcelo Assis, Celia Castillo-Blas,
José J. Baldoví and Isabel Abánades Lázaro**

Table of Contents

S.1. General Experimental Remarks	2
S.2. Materials and Synthesis.....	3
S.3. Characterisation.....	4
S.3.1 Powder X-Ray Diffraction (PXRD).....	4
S.3.2 Proton Nuclear Magnetic Resonance (¹ HNMR)	9
S.3.3 Computational structures.....	14
S.3.4 Thermogravimetric analysis (TGA)	22
S.3.5 Nitrogen Adsorption and Desorption Measurements	30
S.3.6 Scanning Electron Microscopy (SEM)	40
S.3.7 Z-potential	44
S.3.8 Dynamic Light Scattering (DLS)	48
S.3.9 Lattice Strain	55
S.3.10 Vibrational spectroscopy	56
S3.10a. Fourier transformed Infra-Red (FT-IR).....	56
S3.10b. Raman.....	60
S.3.11 Band Gap.....	62
S.3.11a Band Gap (dark)	62
S.3.11b Electronic band gap calculations.....	64
S.3.11c Band Gap (after light irradiation)	66
S.3.11d Band Gap (comparison before and after light irradiation)	68
S.3.11e UV-Vis in the dispersion	72
S.3.12 Photoluminescence.....	79

S.1. General Experimental Remarks

Powder X-Ray Diffraction (PXRD): PXRD patterns were collected in a PANalytical X'Pert PRO diffractometer using copper radiation with an X'Celerator detector, operating at 40 mA and 45 kV, with a step size of 0.017°. Pawley refinements were carried out using TOPASv7.

Thermogravimetric Analysis (TGA): were carried out with a Mettler Toledo TGA/SDTA 851 apparatus between 25 and 800 °C under ambient conditions (10 °C·min⁻¹ scan rate and an air flow of 9 mL·min⁻¹).

Nuclear Magnetic Resonance Spectroscopy (NMR): NMR spectra were recorded on either a Bruker AVIII 300 MHz spectrometer and referenced to residual solvent peaks.

Gas Uptake: N₂ adsorption and desorption isotherms were performed in a Tristar II Plus Micromeritics sorptometer, at 77 K and 273 K, respectively. Activation was set at 120°C, under vacuum, for 24 hours on the already activated samples.

Scanning Electron Microscopy (SEM) and single point energy-dispersive X-Ray analysis (EDX): particle morphologies, dimensions and point energy-dispersive X-Ray analysis were studied with a Hitachi S-4800 scanning electron microscope at an accelerating voltage of 20 kV.

Energy-dispersive X-Ray analysis (EDX) mapping: the mapping of different elements was studied using a SCIOS 2 field emission scanning electron microscope with focused ion beam at an accelerating voltage of 20 kV.

Fourier Transform Infrared Spectroscopy: IR spectra of solids were collected using a Shimadzu Fourier Transform Infrared Spectrometer, FTIR-8400S, fitted with a Diamond ATR unit.

Dynamic Light Scattering and Z-potential: Colloidal analysis and Z-potential were performed by Dynamic Light Scattering (DLS) with a Zetasizer Ultra potential analyser equipped with Non-Invasive Backscatter optics (NIBS) and a 50 mW laser at 633 nm.

Photoluminescence measurements: Photoluminescence (PL) emissions were measured at room temperature using a MonoSpec 27 Jarrel-Ash monochromator coupled with a Hamamatsu R446 photomultiplier using excited by an Innova Argon-ion laser. ($\lambda_{exc} = 350.7$ nm; 2.57 eV, 200 mW). The PL emission spectra were deconvoluted using Voigt-type functions with PeakFit™ software, fixing five distinct components located at 406-415, 443, 518, 574, and 629 nm for all spectra.

UV-Vis: UV-Vis diffuse reflectance spectroscopy (DRS) was performed on a Jasco V-670 spectrophotometer using an integrated Labsphere in the range 200-900 nm.

Lattice strain: The lattice strain parameter can be obtained by:

$$\varepsilon = \frac{\beta}{(4\tan\theta)} \quad \text{Eq. 1}$$

$$\beta = \sqrt{\beta_{obs}^2 + \beta_{st}^2} \quad \text{Eq.2}$$

where β_{obs} is full width at half maximum (FWHM), β_{st} is FWHM of LaB₆ standard and, θ is the Bragg angle.

Raman spectroscopy. Raman spectra of samples were collected using a spectrophotometer JASCO NRS-3100, using an argon-ion laser with $\lambda=633$ nm (7 mW) over the 500–2000 cm⁻¹ range.

S.2. Materials and Synthesis

All reagents unless otherwise stated were obtained from commercial sources and were used without further purification.

General remarks: In 8 mL vials, zirconyl chloride (0.056 mmol, 1 equivalent) and a total of two equivalent of linkers (0.113 mmol), composed of Biphenyl-4,4'-dicarboxylic acid (BPDC) and Azobenzene-4,4'-dicarboxylic Acid (AzDC) were dispersed upon sonication (5 minutes) in a mixture of DMF (5mL) and Acetic acid (0.25 mL). The reaction mixtures were placed in an oven at 120°C. After 24 hours, the reaction mixtures were cooled down to room temperature. Table S1 shows the amount of each linker for the different samples, from which from the total of 2 equivalents (0.113 mmol) the molar percentage was varied.

Table S1: Synthetic conditions.

Sample	zirconyl chloride (mmol)	zirconyl chloride (mg)	Total linkers (mmol)	BPDC (mmol)	BPDC (mg)	AzDC (mmol)	AzDC (mg)
0% AzDC	0.06	18.23	0.11	0.00	0.00	0.11	30.40
25% AzDC	0.06	18.23	0.11	0.03	6.81	0.08	22.80
50% AzDC	0.06	18.23	0.11	0.06	13.63	0.06	15.20
75% AzDC	0.06	18.23	0.11	0.08	20.44	0.03	7.60
100% AzDC	0.06	18.23	0.11	0.11	27.25	0.00	0.00

Activation protocols: The resultant powder was collected by centrifugation (5000 rpm, 5 min) and washed with DMF (X3) and MeOH (x3) through dispersion-centrifugation cycles. The samples were activated by stirring the samples in MeOH for approximately 24 hours, and further dried under vacuum at 120°C overnight before characterization.

S.3. Characterisation

S.3.1 Powder X-Ray Diffraction (PXRD)

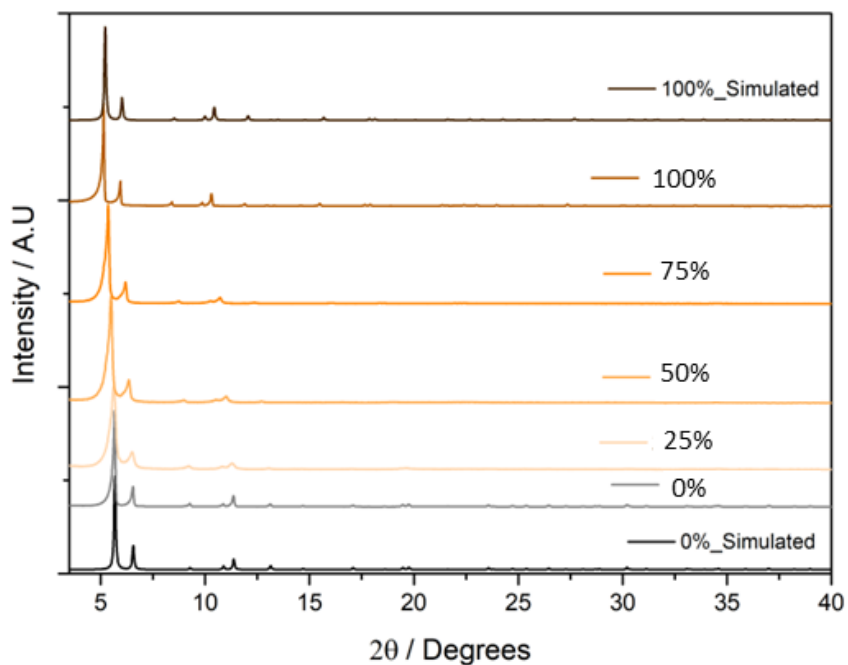


Figure S1: PXRD patterns of MTV MOFs compared to pristine MOFs synthesized under analog conditions and their simulated PXRD patterns from reported cifs. ^[1]

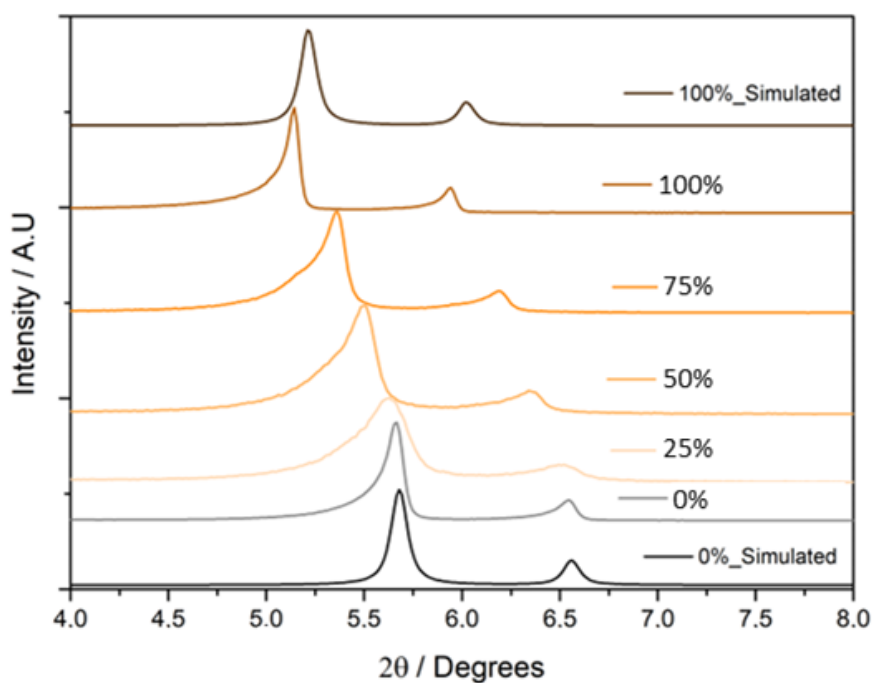


Figure S2: PXRD patterns of MTV MOFs compared to pristine MOFs synthesized under analog conditions and their simulated PXRD patterns from reported cifs. ^[1]

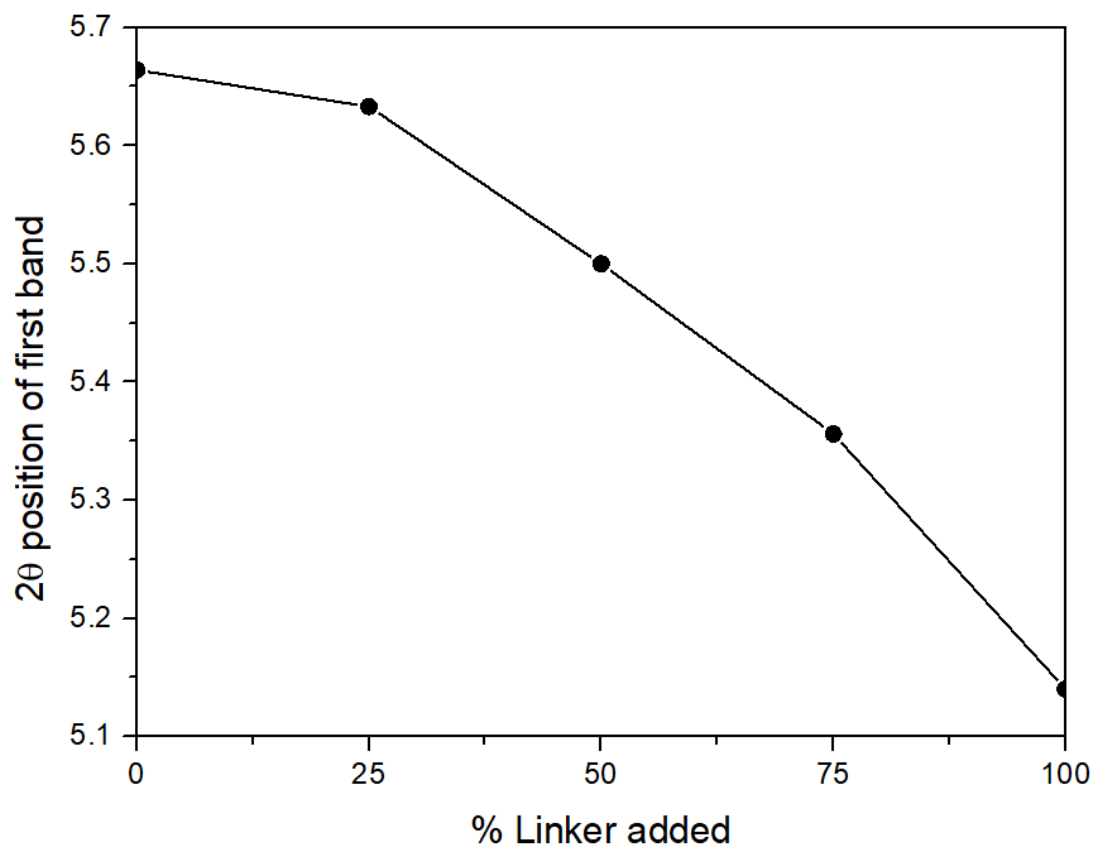


Figure S3: Variation of the position of the first Bragg reflection as a function of AzDC linker added to the synthesis.

Table S2: Summary of Pawley refinements

Material	R_p	R_{wp}	Space group	Zero	Lattice parameter	Profile parameters	Finger-Cox correction (asymmetry)	Lattice parameter reported from literature
0%	12.45 %	19.95 %	<i>Fm-3m</i>	-0.0243 (7)	$a = 26.806$ (8)	$U = 5.463$ (7) $V = -0.15$ (3) $W = 0.0305$ (14)	$H/L = 0.023$ (10) $S/L = 0.024$ (10)	0%AzDC (UiO-67) ^[1] $a = 26.9276$ (2)
25%	7.66 %	10.39 %	<i>Fm-3m</i>	-0.0016 (32)	$a = 26.966$ (7)	$U = 5.98$ (76) $V = -0.50$ (15) $W = 0.559$ (12)	$H/L = 0.0303$ (17) $S/L = 0.0231$ (18)	
50%	15.81 %	13.62 %	<i>Fm-3m</i>	-0.050 (3)	$a = 27.396$ (13)	$U = 6.28$ (22) $V = 0.809$ (23) $W = -0.0356$ (9)	$H/L = 0.0352$ (2) $S/L = 0.0131$ (3)	100% AzDC (UiO-AZDC) ^[1] $a = 29.3248$ (8)
75%	14.54 %	18.07 %	<i>Fm-3m</i>	0.0724 (10)	$a = 29.383$ (18)	$U = 7.85$ (1.17) $V = 5.54$ (33) $W = -0.188$ (13)	$H/L = 0.0372$ (8) $S/L = 0.0251$ (5)	
100%	16.32 %	19.89 %	<i>Fm-3m</i>	-0.0197 (3)	$a = 29.5466$ (26)	$U = 2.26$ (9) $V = -0.549$ (23) $W = 0.0492$ (11)	$H/L = 0.0452$ (12) $S/L = 0.0234$ (15)	

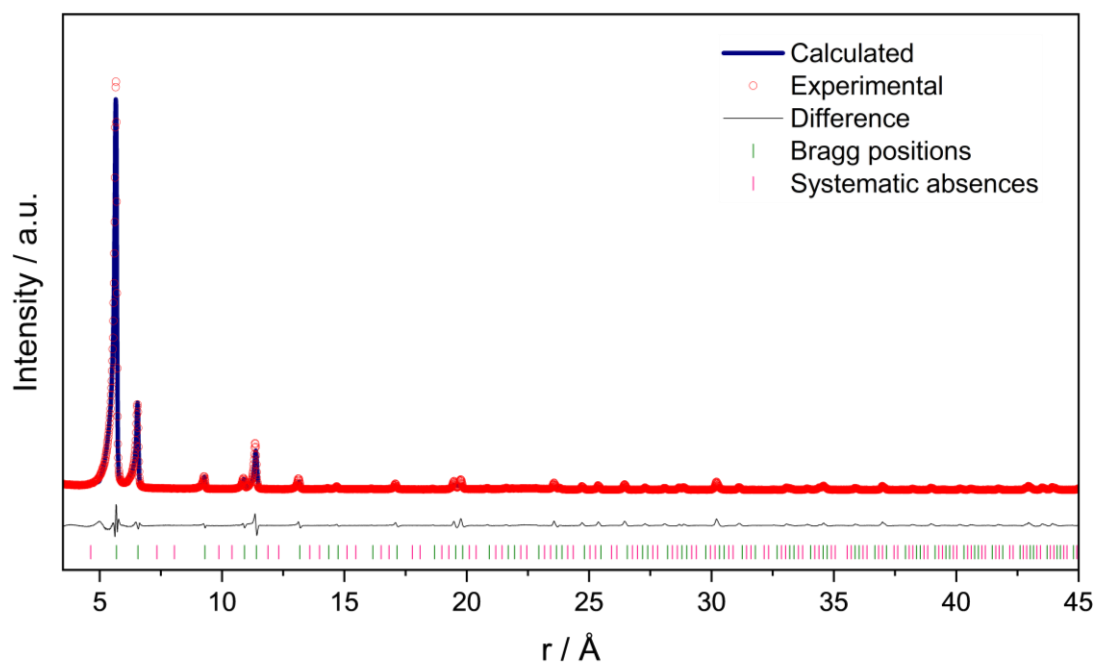


Figure S4. Pawley refinements of 0% AzDC, UiO-67.

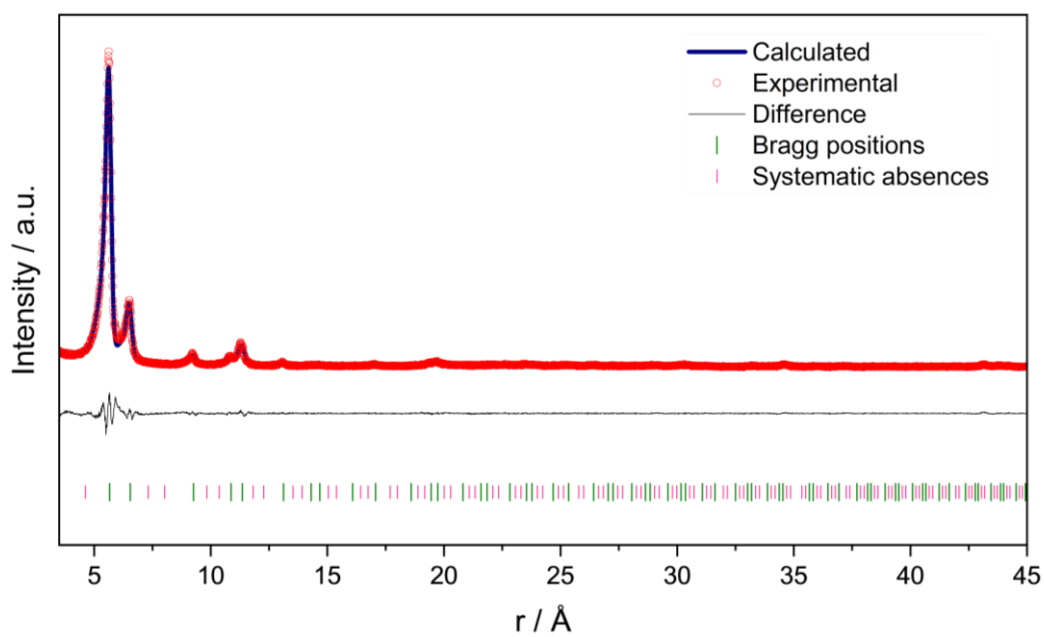


Figure S5. Pawley refinements of 25% AzDC.

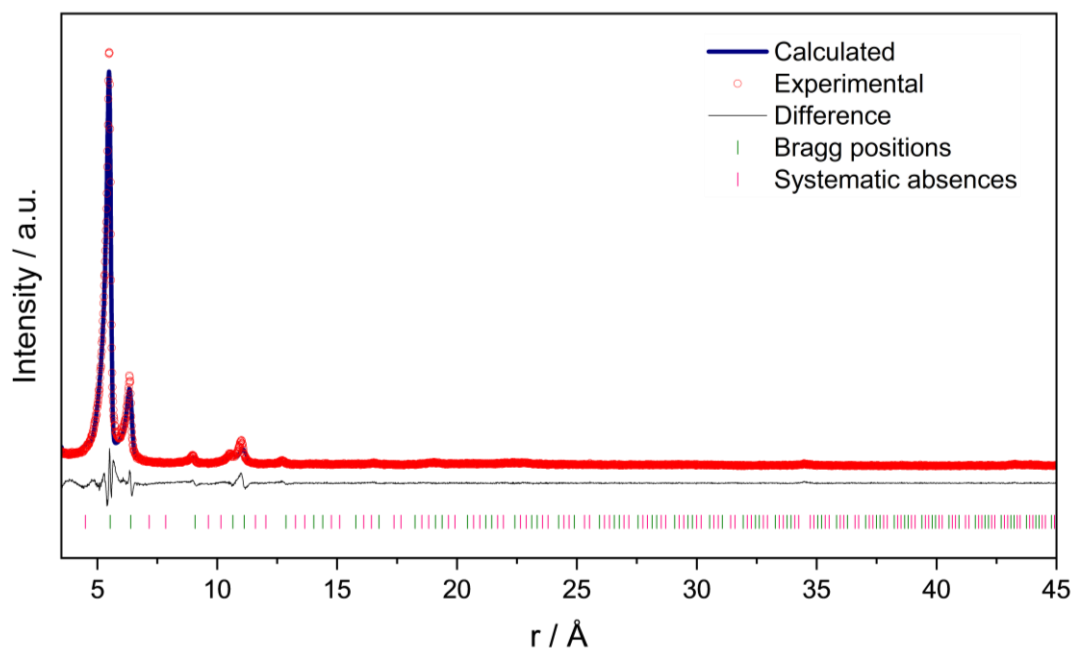


Figure S6. Pawley refinements of 50% AzDC.

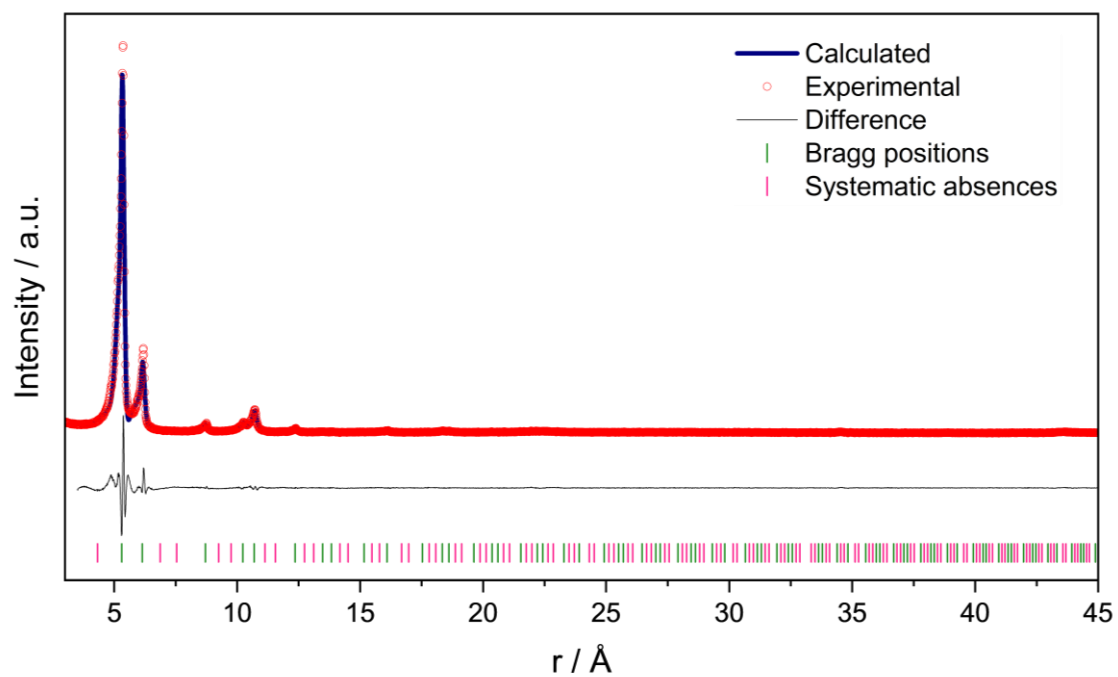


Figure S7. Pawley refinements of 75% AzDC.

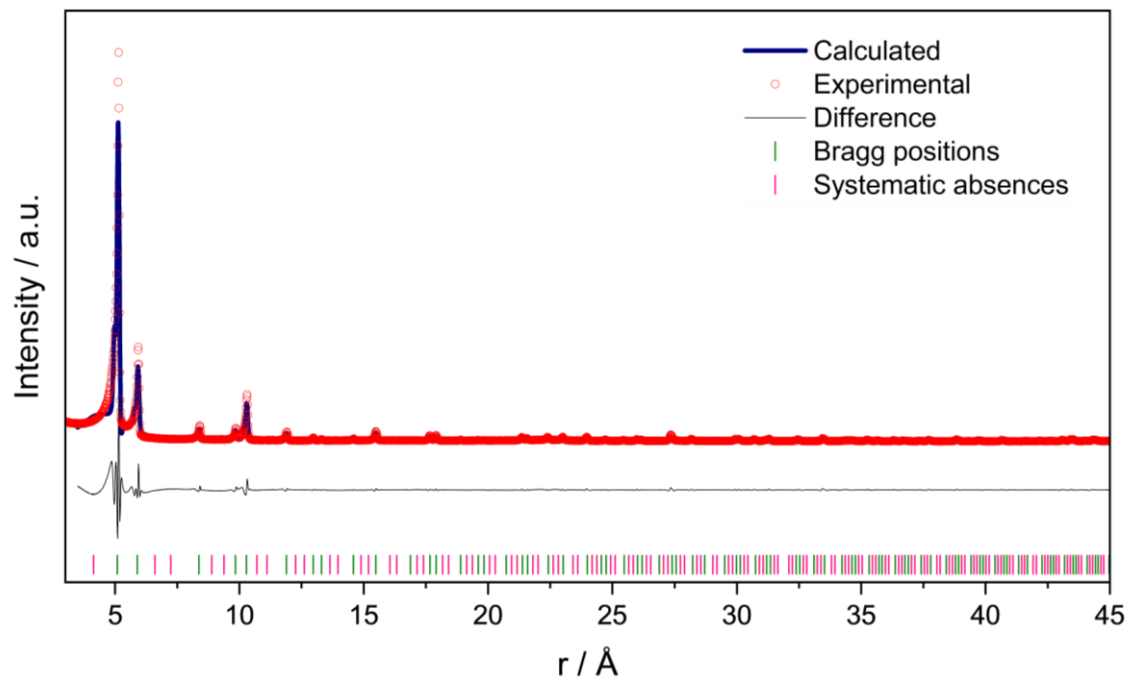


Figure S8. Pawley refinements of 100% AzDC.

S.3.2 Proton Nuclear Magnetic Resonance (^1H NMR)

Incorporation of L1 and defect-compensating species is expressed as the **molar ratio** (R_{L1}) between L1 and L2, $R_{L1} = \frac{L1}{L2}$ and as the **molar percent** of modulator (mol%) compared to bpdc, $L1\% = \frac{L1}{L1+L2} * 100$.

Note that the signal at ca. 7.9 is DMF (Figure S9), which is removed after dispersing the samples in MeOH for 24 hours (Figure S10),

Please note that minor shifting of these signals can be observed due to the use of deuterated sulphuric acid to digest the MOFs for ^1H NMR analysis.

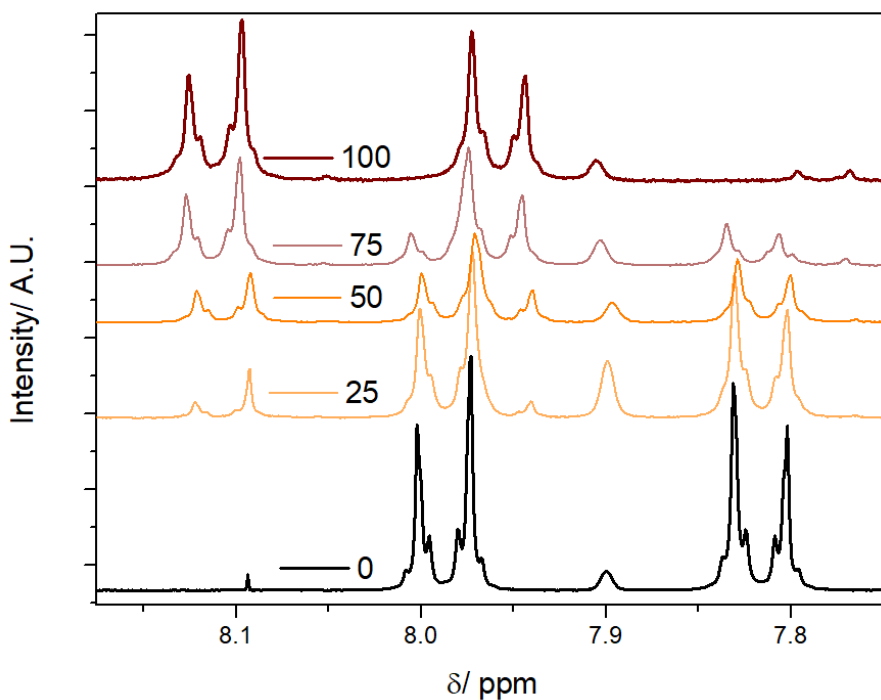


Figure S9: Amplification of ^1H NMR profiles acid-digested samples, showing the varying ratios of linkers.

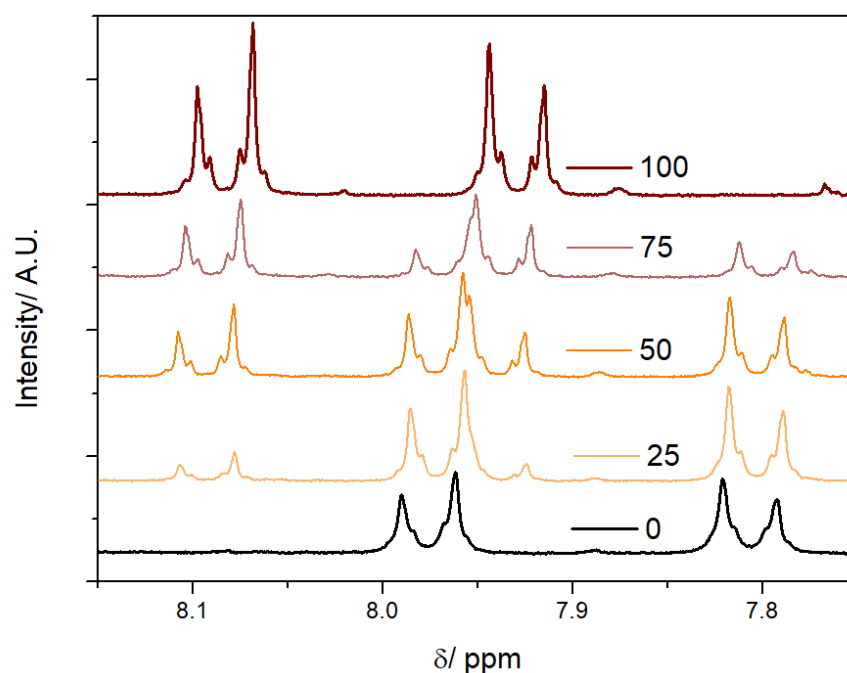


Figure S10: Amplification of ^1H NMR profiles acid-digested samples, showing the varying ratios of linkers of the activated samples after 24 hours of immersion in MeOH.

Table S3: Linker composition extracted from the acid-digested NMR samples. Note that the AcOH content refers to the samples prior to 24 hours MeOH stirring, whereas the MeOH content to the samples post 24h of MeOH stirring. For the 100% AzDC sample the ratios are given per AzDC instead of BPDC.

Sample	AzDC mol%	AzDC/BPDC	AcOH/BPDC	MeO-/BPDC
0	0	0	0.104	0.283
25	13.31	0.15	0.144	0.188
50	39.01	0.64	0.215	0.338
75	69.42	2.27	0.253	0.323
100	100	infinite	0.320	0.245

Table S4: Average and standard deviation of the molar percent of linker incorporated, characterized for different batches.

Sample	AzDC mol%	SD mol%
0	0	0
25	19.22	5.91
50	41.24	2.23
75	65.57	3.85
100	100	100

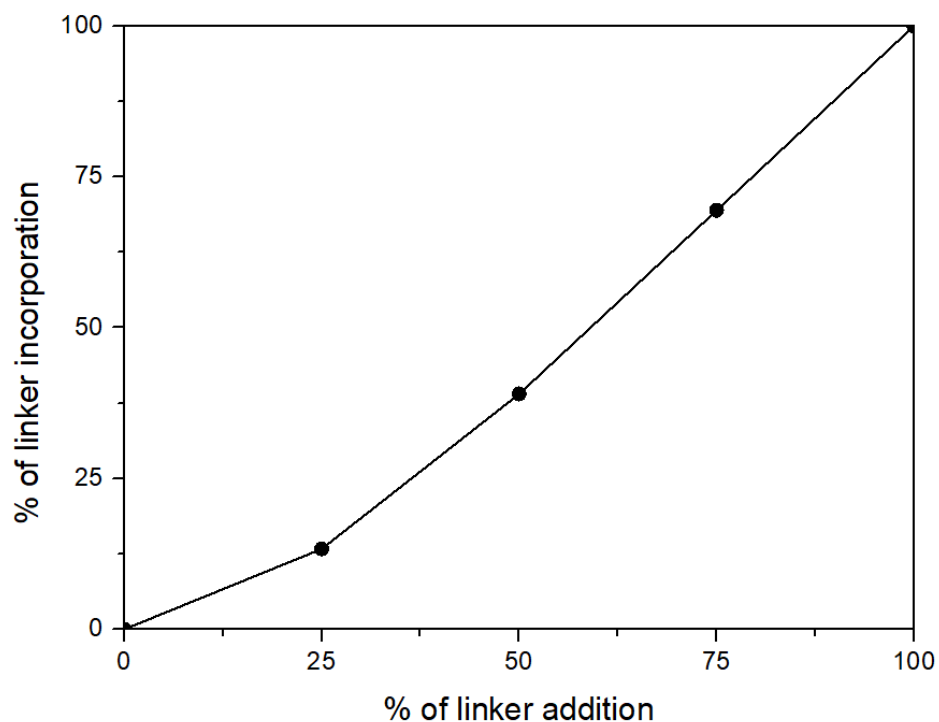


Figure S11: Variation of AzDC linker incorporation (molar percent) as a function of AzDC added to the synthesis.

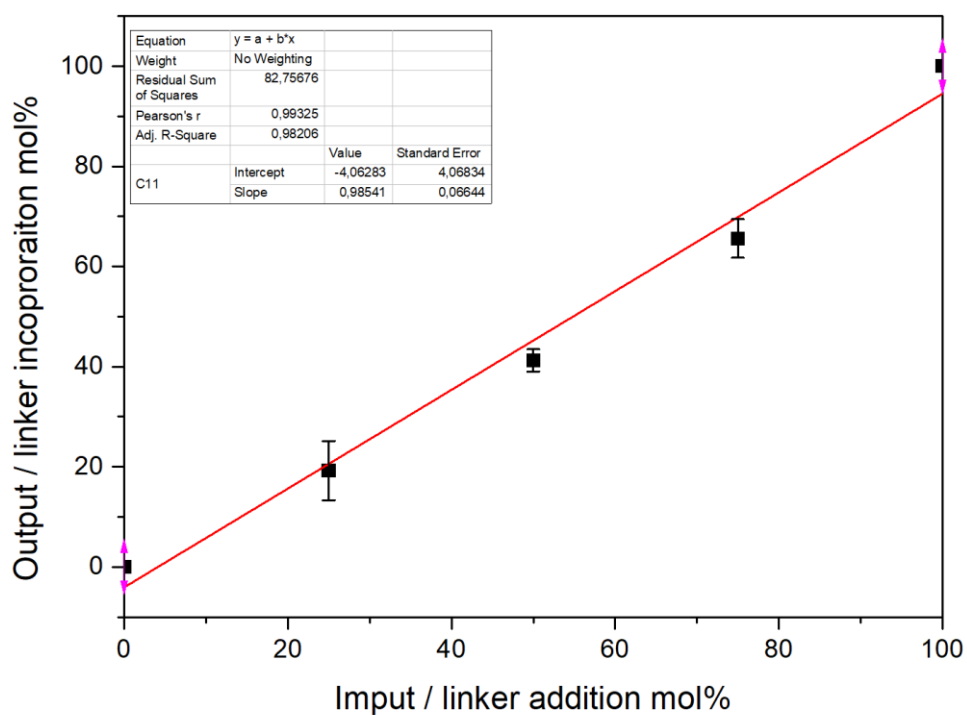


Figure S12: Variation of AzDC linker incorporation (molar percent) as a function of AzDC linker added to the synthesis, demonstrating reproducibility in incorporation for different batches.

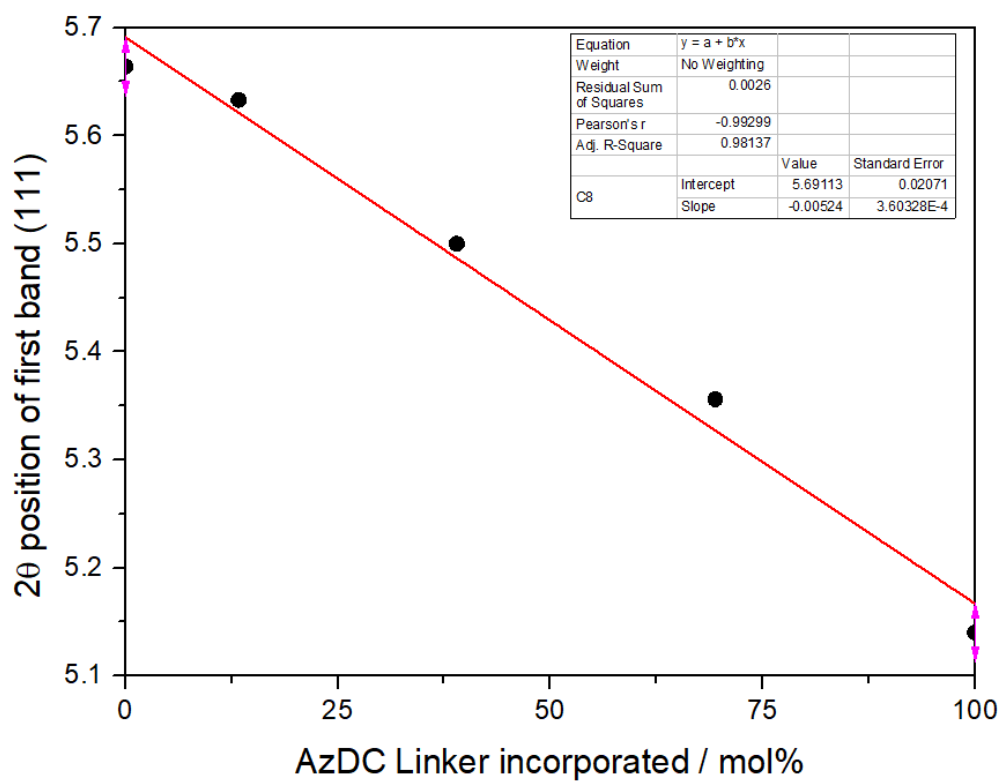


Figure S13: Variation of the position of the first Bragg reflection as a function of AzDC linker incorporated.

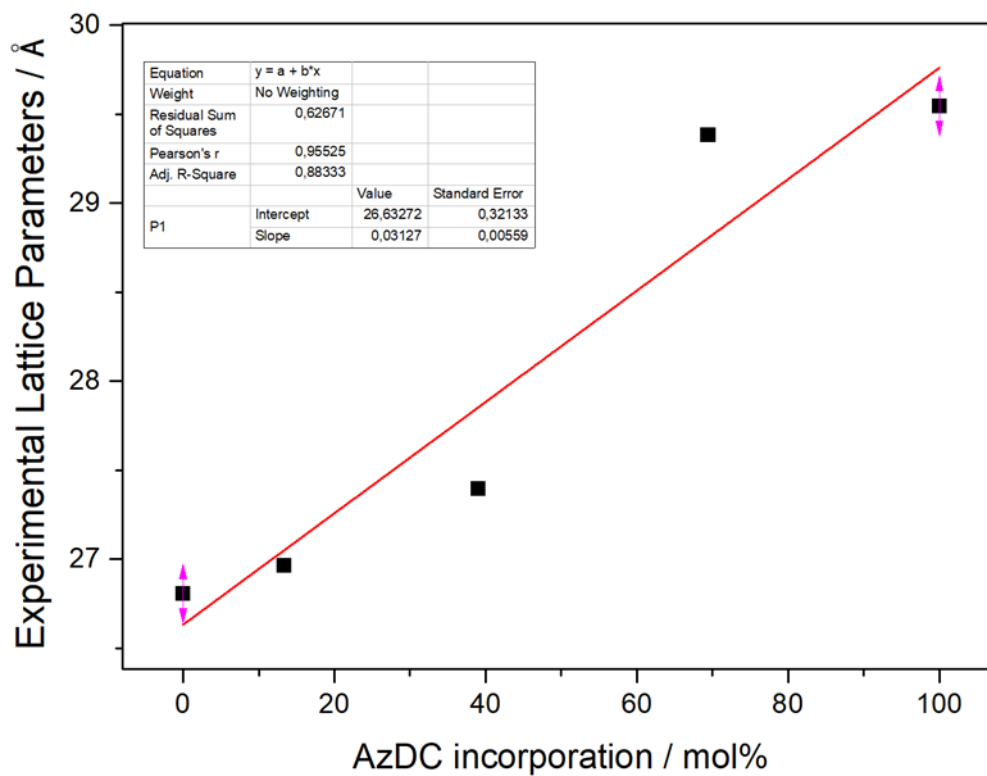


Figure S14: Variation of the unit cell parameters as a function of AzDC linker incorporated in molar percentage.

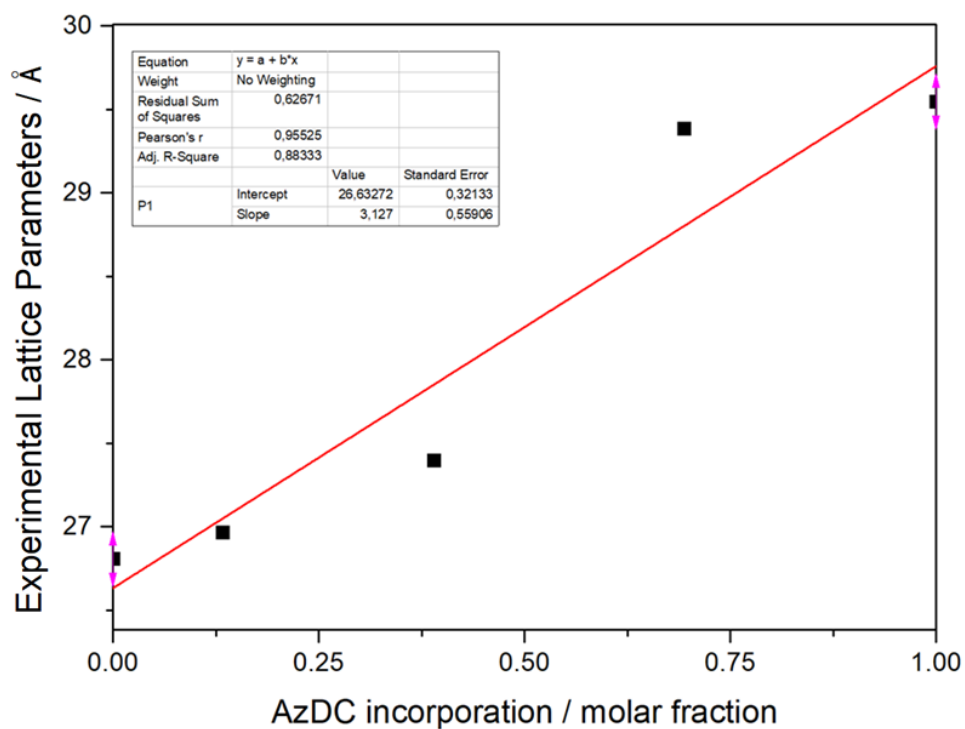


Figure S15: Variation of the unit cell parameters as a function of AzDC linker incorporated in molar fraction, as calculated for the Vegard's law.

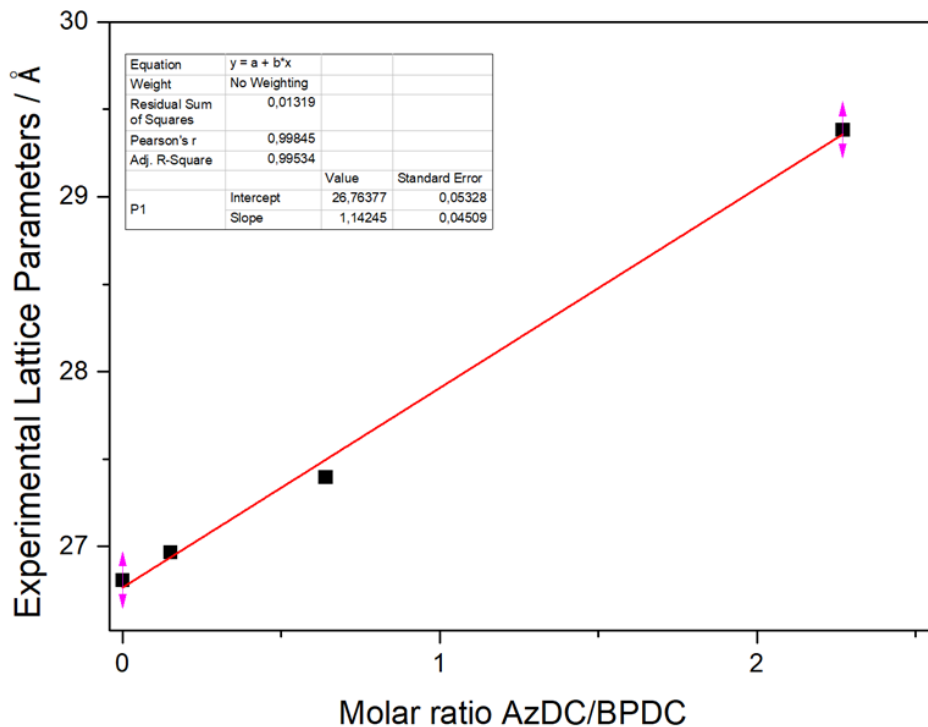


Figure S16: Variation of the unit cell parameters as a function of AzDC linker incorporated in molar ratio.

S.3.3 Computational structures

We performed first-principles spin-polarized density functional theory (DFT) calculations using the mixed Gaussian and plane wave basis as implemented in the CP2K/QUICKSTEP package version 2023.2.^[2,3] The exchange-correlation was taken into account using the generalized gradient approximation (GGA) in combination with the Perdew–Burke–Ernzerhof (PBE) functional.^[4] Norm-conserving Goedecker–Teter–Hutter (GTH) pseudopotentials^[5,6] and DZVP-MOLOPT-SR-GTH basis sets^[7] were used in all the calculations. A 600 Ry plane wave cutoff was used to expand the electronic density in all the calculations. Dispersion corrections to consider van der Waals interactions were implemented by applying semi-empirical Grimme-D3 corrections.^[8] All structures were fully optimized using the limited memory Broyden-Fletcher-Goldfarb-Shanno (L-BFGS) algorithm.

We constructed the MTV series with AzDC linker percentages of 25, 50, 75 and 100% in the unit cell and we fully relaxed both atomic coordinates and cell parameters. To validate our methodology, we constructed the same structures but starting from the 100% AzDC linker and allowed them to relax in the same way as in the previous case. We noticed that we obtained the same structures after relaxation using both approaches, confirming that our proposed methodology is able to describe the MVT Zr₆MOFs series. The introduction of the consecutive linkers was performed in the same plane of the unit cell, as this approach provided the lower symmetry loss and enhanced the performance of the simulations.

Table S5: Parameters extracted from the calculated structures.

% AzDC	Lattice parameter / Å	111 reflection band / 2Θ	Cell volume / Å³
0	27.063	5.656	19821
25	28.668	5.331	23562
50	29.092	5.257	24621
75	29.416	5.198	25454
100	29.864	5.124	26634

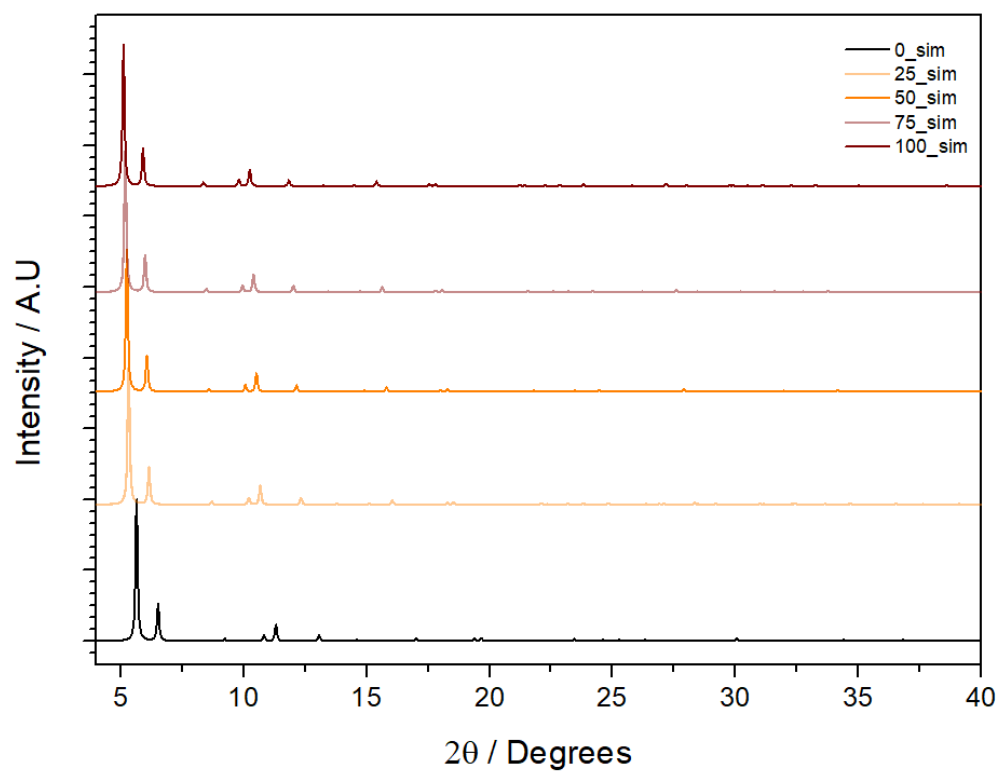


Figure S17: Simulated PXRD patterns of the calculated structures.

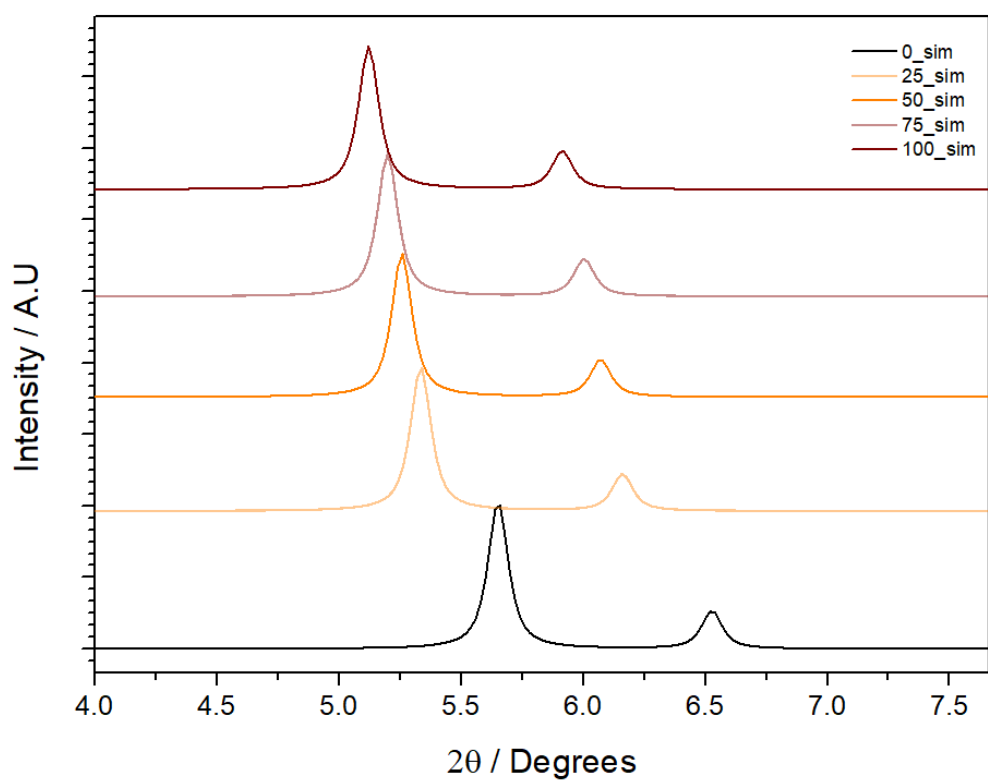


Figure S18: Amplification of the simulated PXRD patterns of the calculated structures.

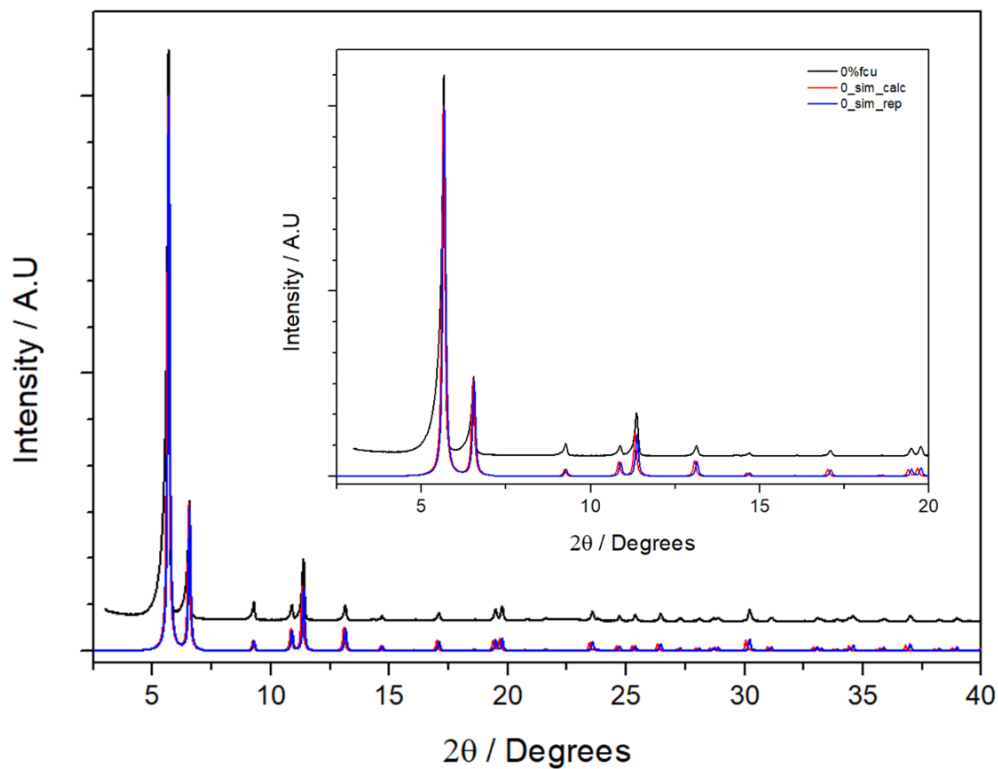


Figure S19: Comparison of the PXRD patterns of 0% AzDC MOFs. Black experimental, red simulated from calculated structures, blue simulated from cif. ^[1]

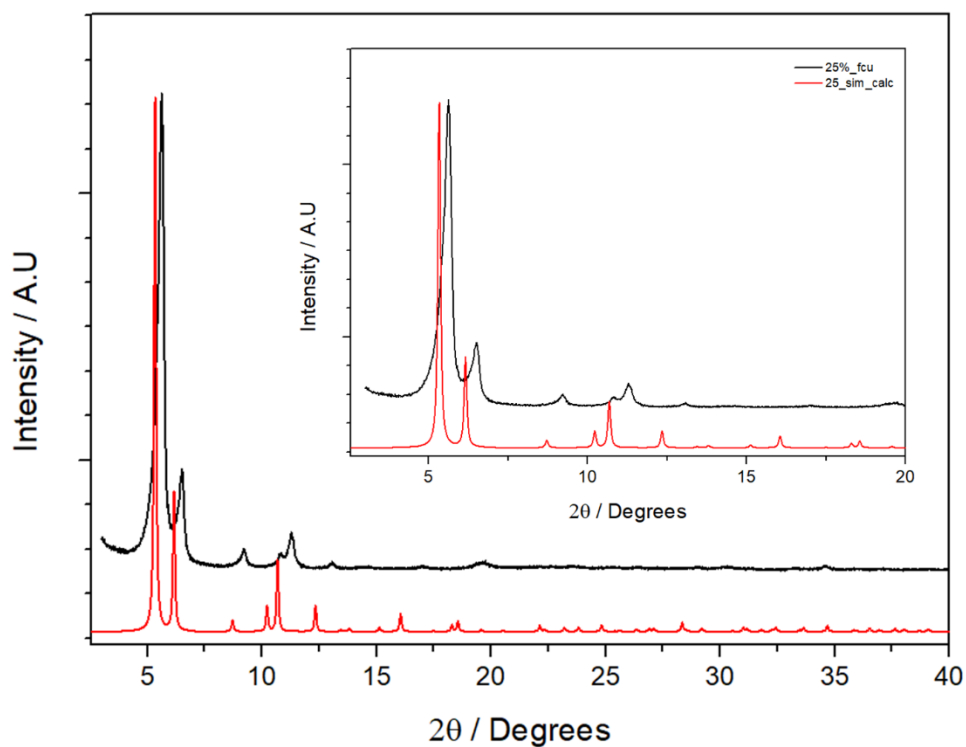


Figure S20: Comparison of the PXRD patterns of 25% AzDC MOFs. Black experimental, red simulated from calculated structures.

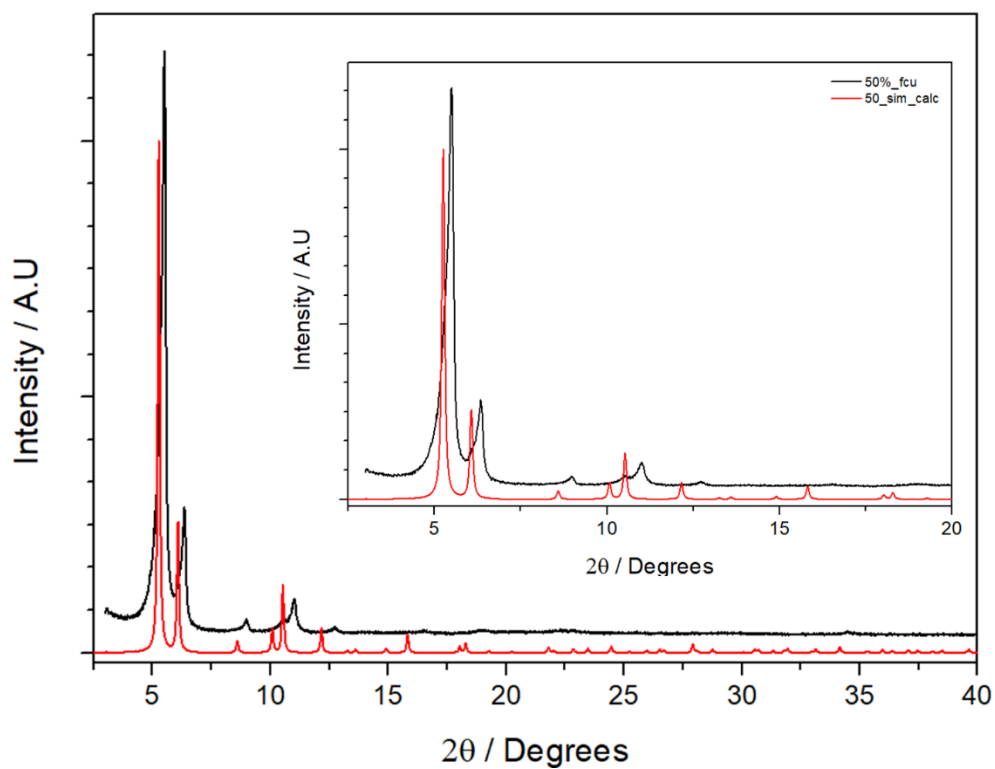


Figure S21: Comparison of the PXR D patterns of 50% AzDC MOFs. Black experimental, red simulated from calculated structures.

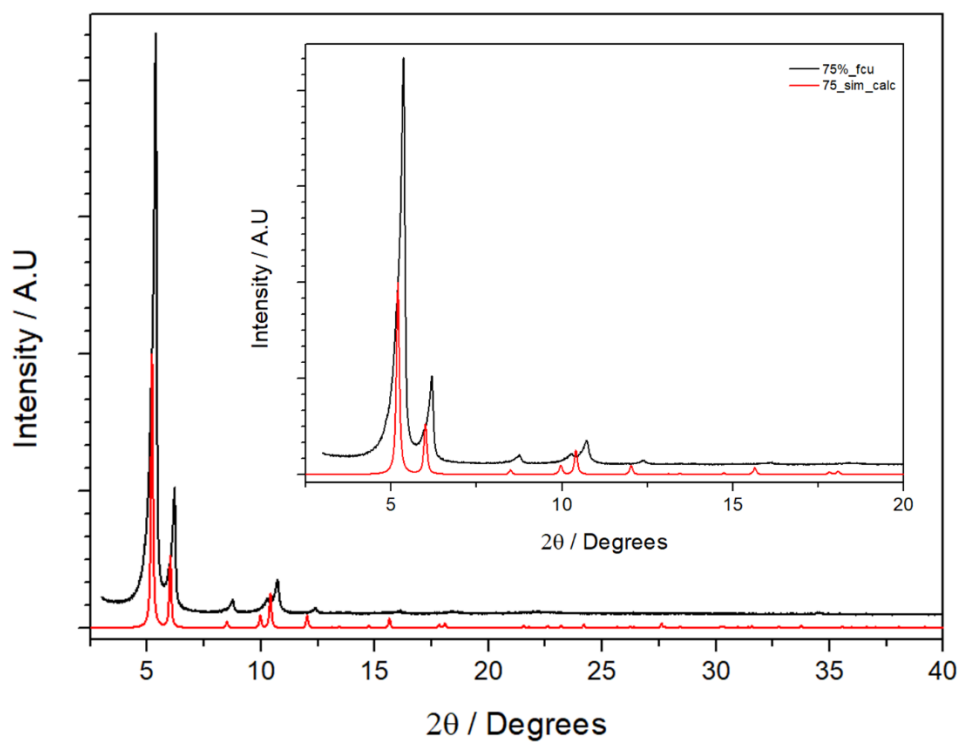


Figure S22: Comparison of the PXR D patterns of 75% AzDC MOFs. Black experimental, red simulated from calculated structures.

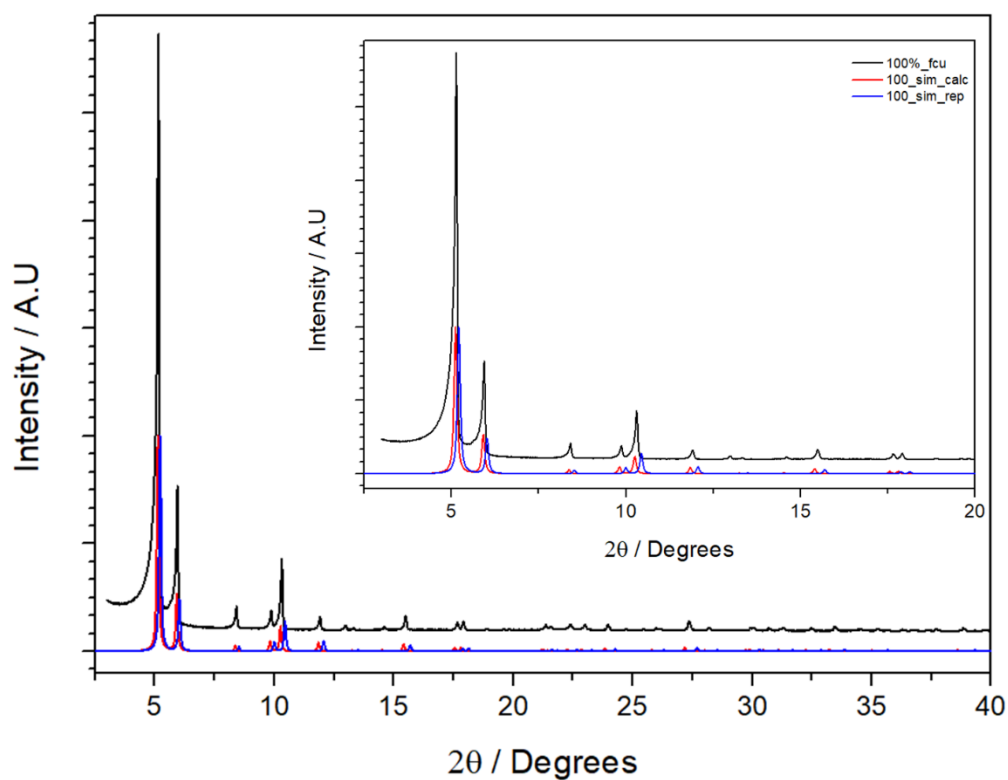


Figure S23: Comparison of the PXRD patterns of 0% AzDC MOFs. Black experimental, red simulated from calculated structures, blue simulated from cif, ^[1] showing a significantly better matching between the calculated structure and experimental structure.

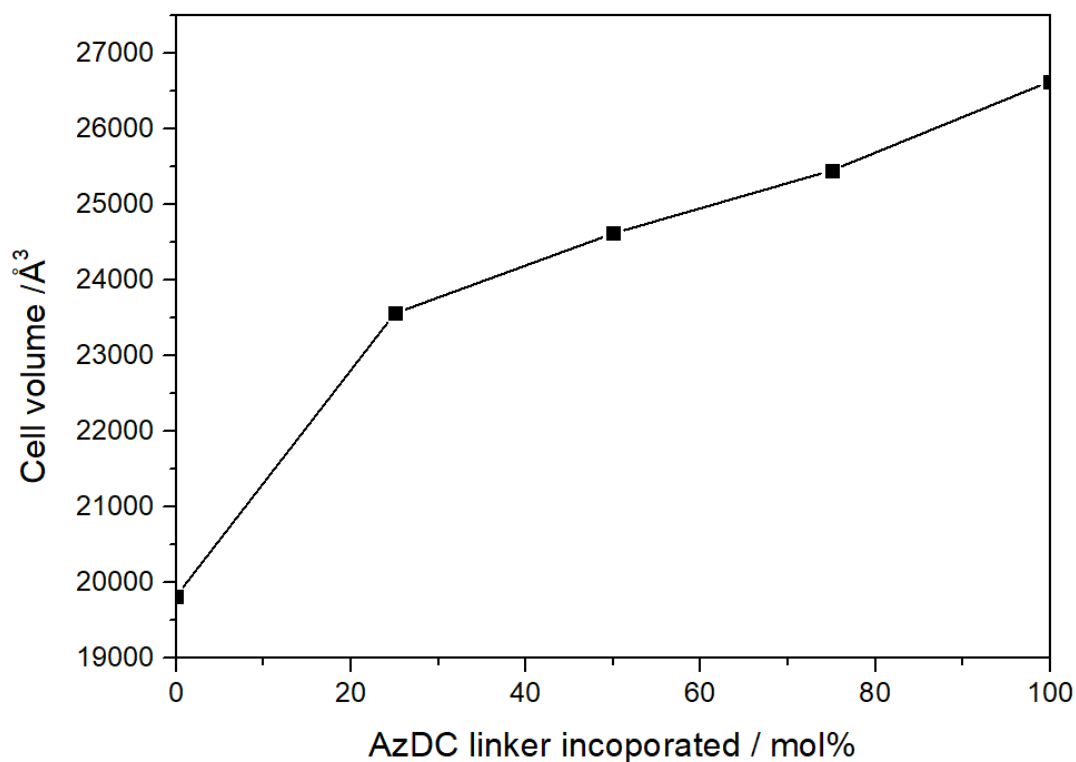


Figure S24: Relation between the cell volume and the molar percentage of AzDC in the calculated structures.

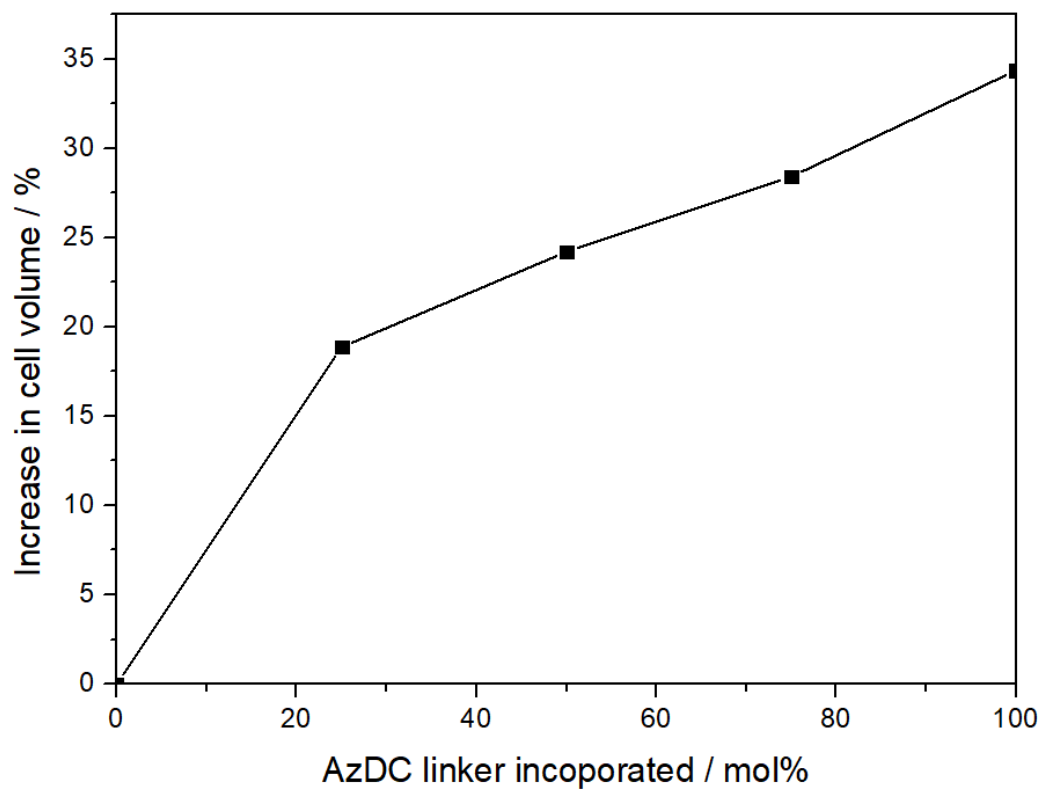


Figure S25: Relation between the increase in cell volume and the molar percentage of AzDC in the calculated structures.

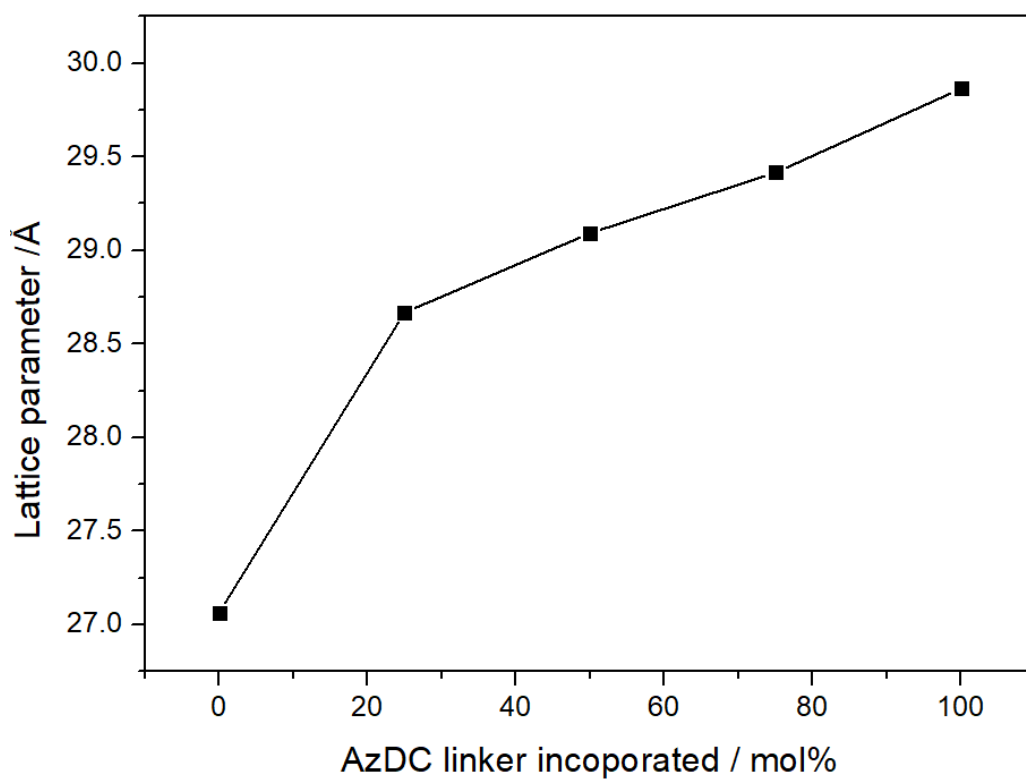


Figure S26: Relation between the lattice parameter and the molar percentage of AzDC in the calculated structures.

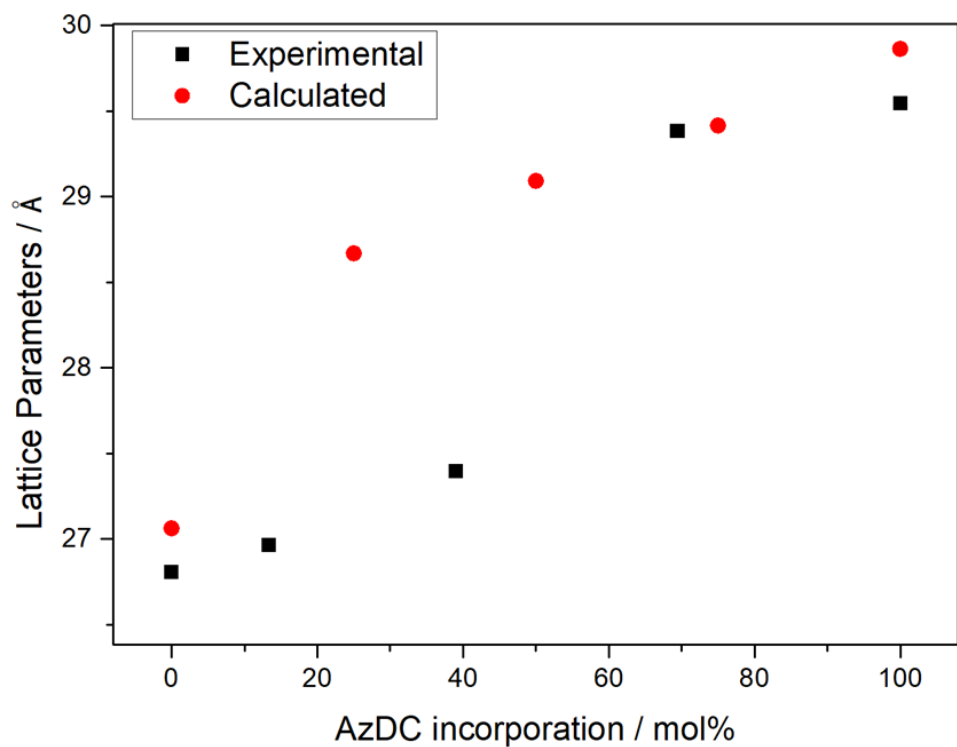


Figure S27: Relation between the experimental and calculated unit cell parameters and the molar percentage of AzDC in calculated and experimental structures.

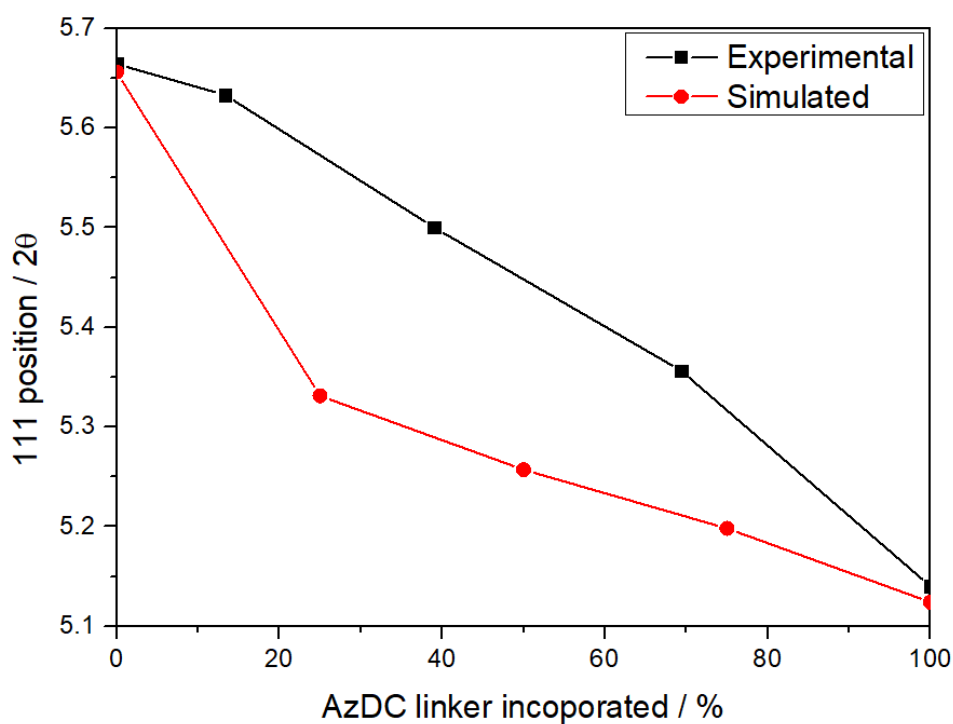


Figure S28: Relation between the position of the first reflection band and the % of AzDC for calculated and experimental structures.

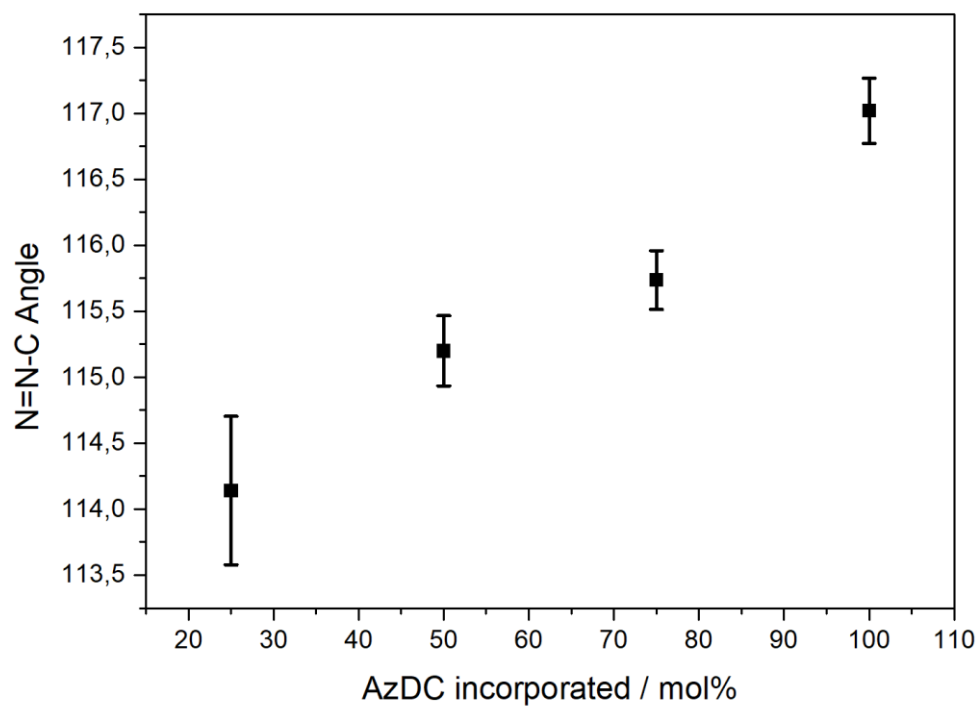


Figure S29: Relation between the N=N-C angle and the percentage of AzDC incorporated in calculated structures.

S.3.4 Thermogravimetric analysis (TGA)

We have estimated the composition of MTVM MUV-10 through the combination of TGA with molar ratios determined by ¹HNMR, assuming that both linkers are bonded through both carboxylates in the $Zr_6(O)_4(OH)_4(L1)_x(L2)_y(MeO^-)_A(OH/H_2O)_D$ using previously reported methodology.^[9] As the linkers decomposes at similar temperatures. the experimental ratio between the molecular weight of the dehydrated MOF (DH MOF) and its residue is expressed as follows.

$$(R_{\text{expDH}}) = \frac{M_w [\text{DH MOF}]}{M_w [\text{Residue}]} = \frac{M_w [ZrO(L1)_x(L2)_y(O)_{\frac{(2-2x-2y)}{2}}]}{M_w [ZrO_2]}$$

Since.

$$x L1 = y L2 * \left(\frac{L1}{L2}\right) \text{NMR ratio}$$

Then.

$$R_{\text{expDH}} = \frac{M_w [ZrO(L1)_x(L2)_{xNMR}(O)_{(1-xL1-xNMR L2)}]}{M_w [ZrO_2]}$$

$$x L1 = \frac{(R_{\text{expDH}} * M_w [ZrO_2]) - M_w ZrO - M_w [O]}{M_w [L1] + NMR * M_w [L2] - (1 + NMR) * M_w [O]}$$

Once X (L1) has been obtained.

$$y L2 = x L1 * \left(\frac{L1}{L2}\right) \text{NMR ratio}$$

$$a \text{Methoxy} = X * \left(\frac{MeO^-}{L1}\right) \text{NMR ratio}$$

The number of OH/H₂O pairs needed to compensate the charge can be calculated using the following equation. taking into account the charge of the different species:

$$4Zr = \left(\frac{4}{6}\right) * OH + \left(\frac{4}{6}\right) * O + 2XL1 + y2L2 + XNMRMeO + OH$$

$$\text{Then } OH = 4 - 2XL1 - 2yL2 - aMeO$$

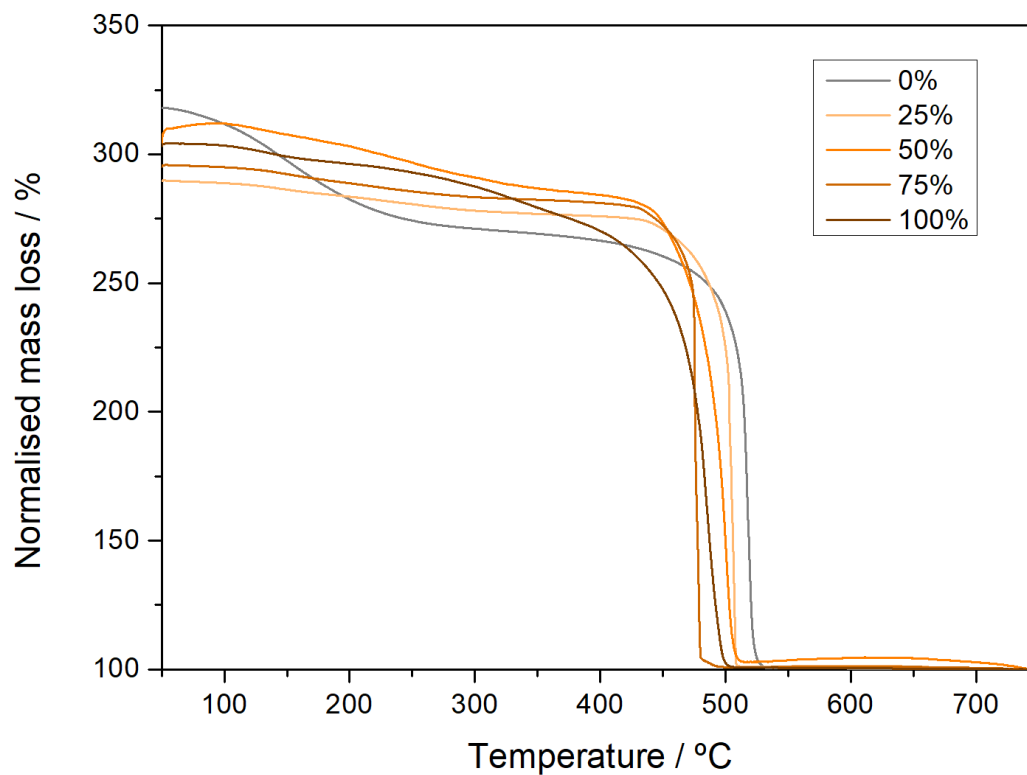


Figure S30: Comparison of the thermal decomposition profiles of the samples. with residue normalized to 100%.

Table S6: Values of the linkers' thermal decomposition temperatures of the different samples.

Sample	Thermal decomposition (start of linker decomposition)
0%	475
25%	461
50%	443
75%	438
100%	419

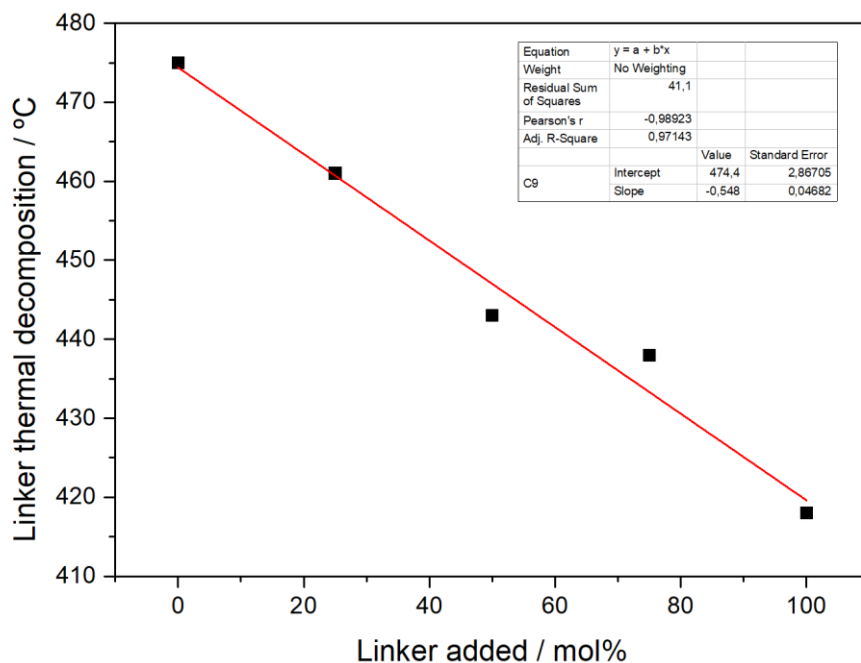


Figure S31: Thermal decomposition temperature of the linker decomposition step (start. inflection point) as a function of the molar percent of linker added to the synthesis.

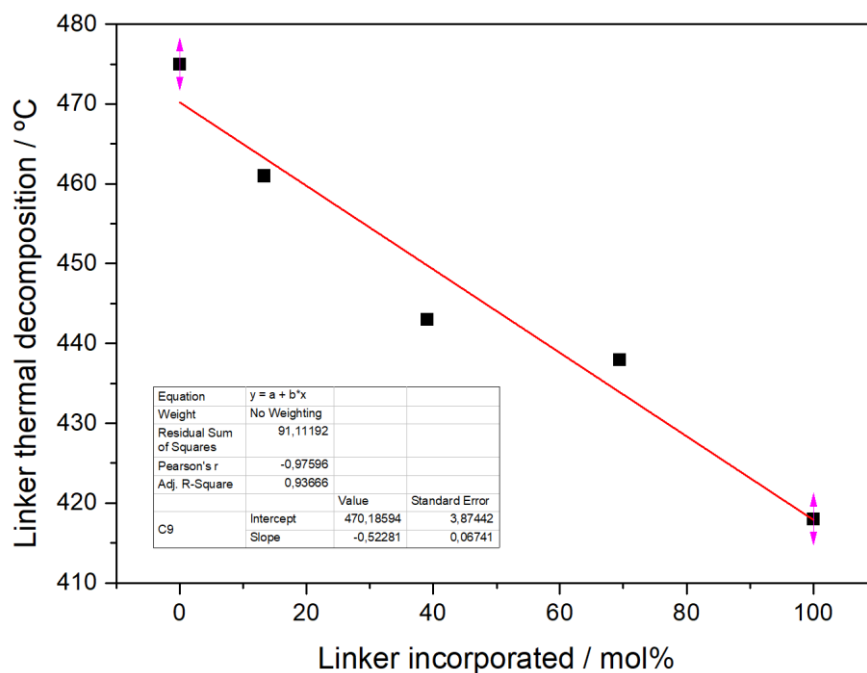


Figure S32: Thermal decomposition temperature of the linker decomposition step (start. inflection point) as a function of the molar percent of linker incorporated.

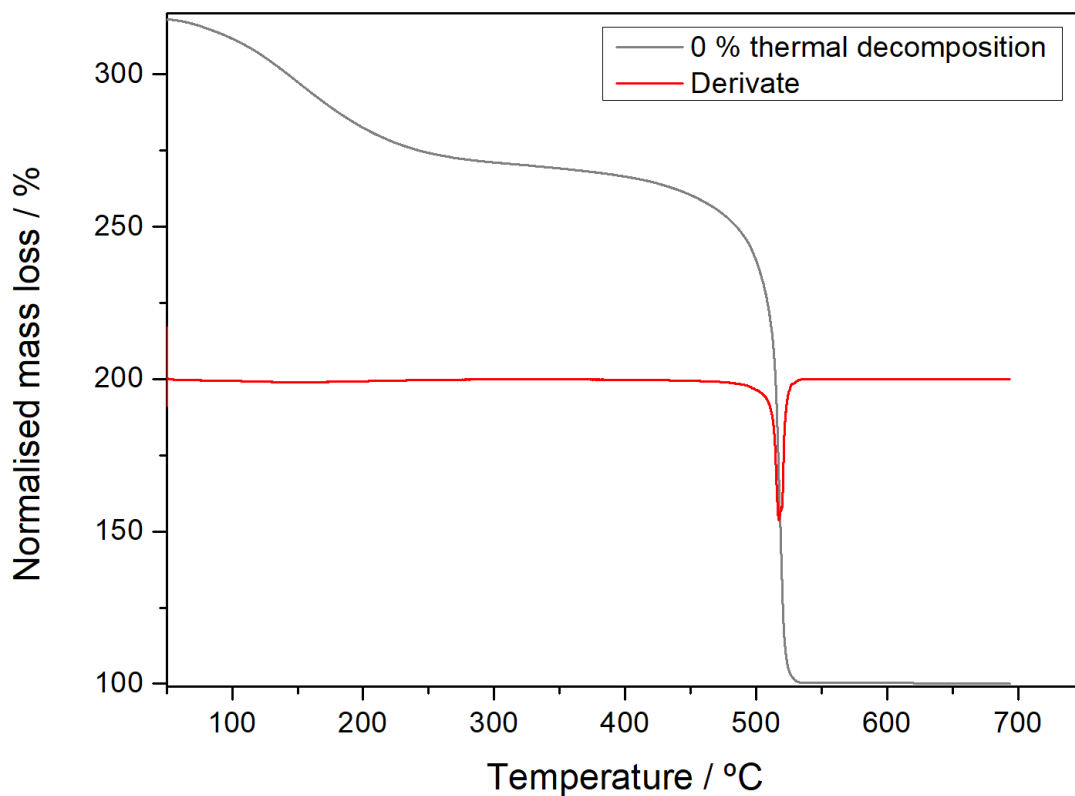


Figure S33: Thermal decomposition profile of the 0% sample. with residue normalized to 100%. alongside the 1st derivative of the thermal decomposition.

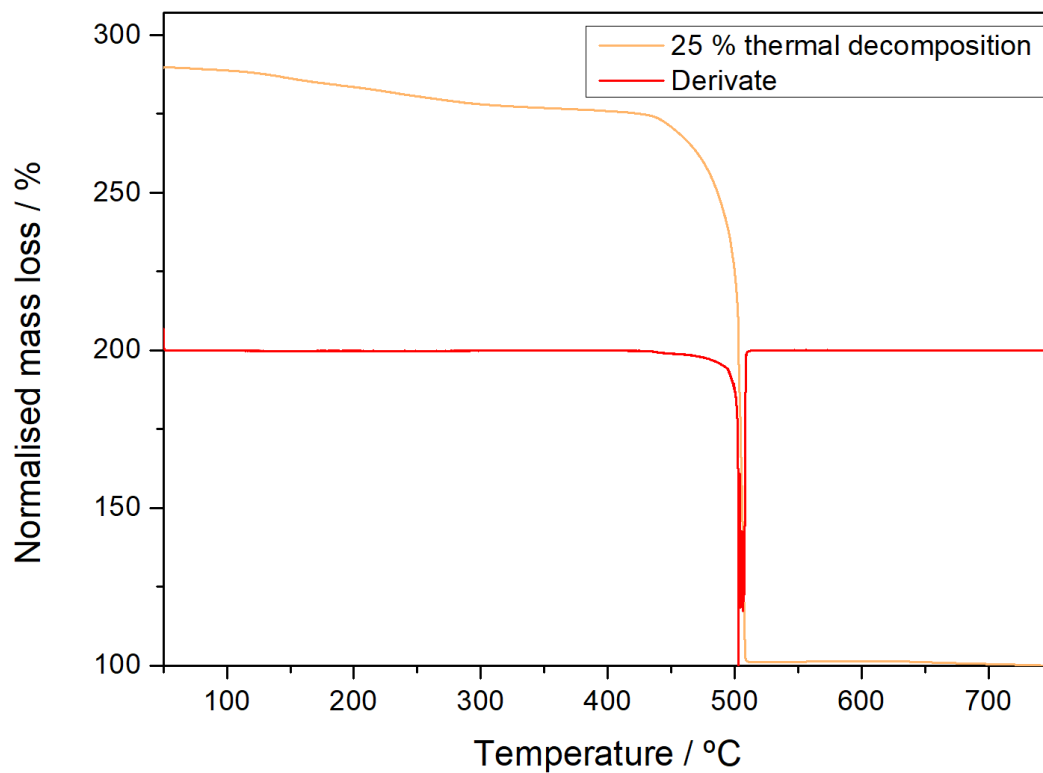


Figure S34: Thermal decomposition profile of the 25% sample. with residue normalized to 100%. alongside the 1st derivative of the thermal decomposition.

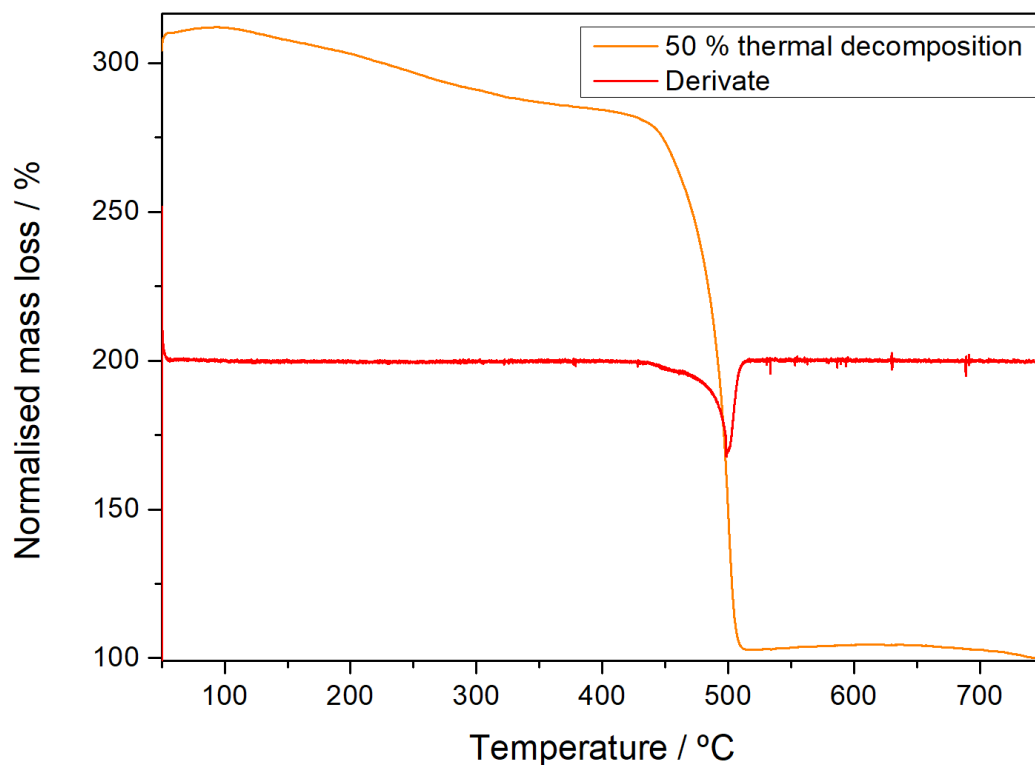


Figure S35: Thermal decomposition profile of the 50% sample. with residue normalized to 100%. alongside the 1st derivative of the thermal decomposition.

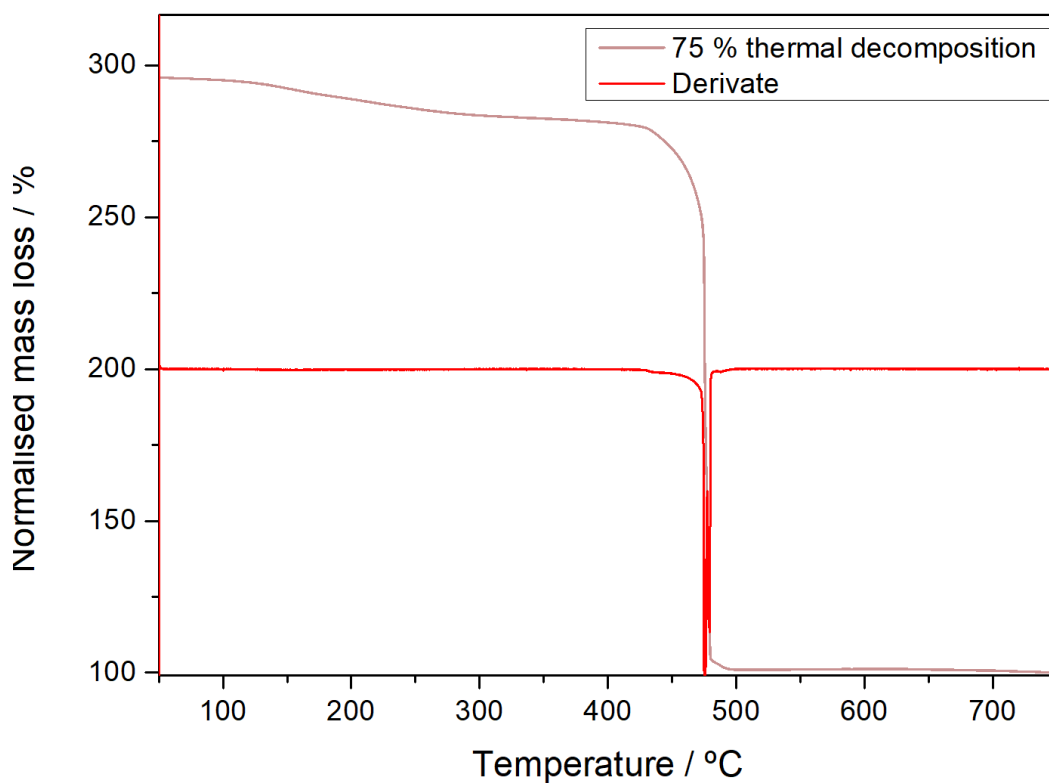


Figure S36: Thermal decomposition profile of the 75% sample. with residue normalized to 100%. alongside the 1st derivative of the thermal decomposition.

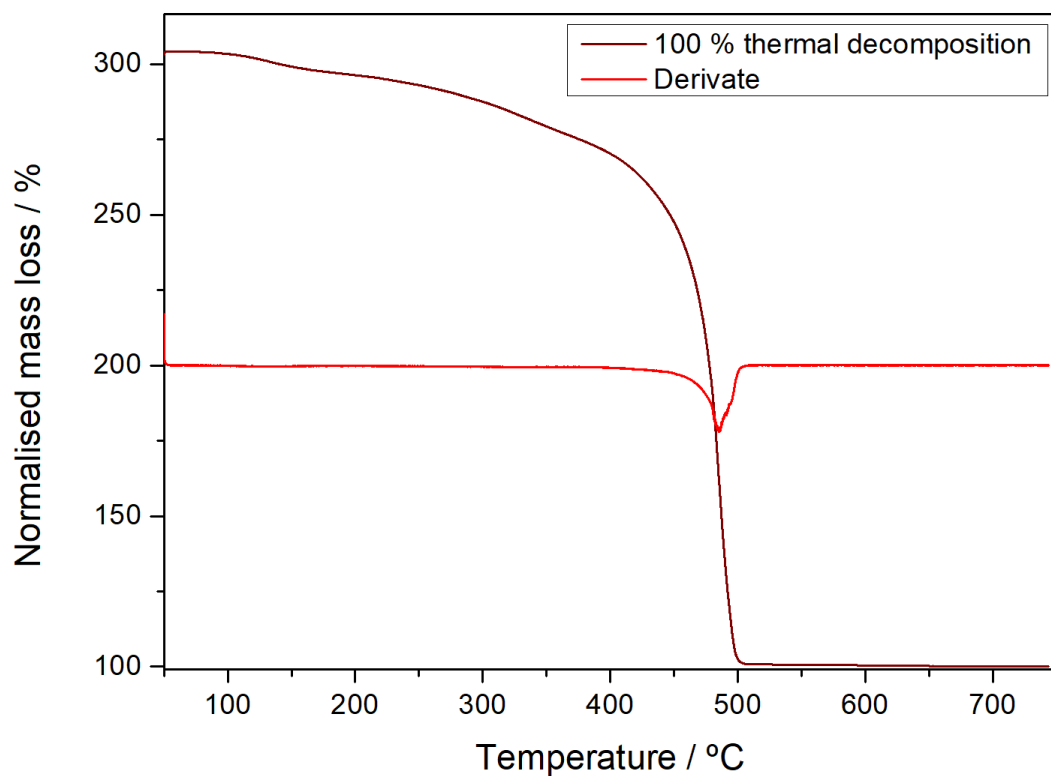


Figure S37: Thermal decomposition profile of the 100% sample, with residue normalized to 100%, alongside the 1st derivative of the thermal decomposition.

Table S7: Composition values extracted from TGA analysis.

Sample	R _{exp}	R _{expDH}	BPDC/Zr	AzDC/Zr	L tot	MeO- /Zr	MeO- /ML	ML %
0%	317	266	0.912	0.000	0.912	0.258	2.93	8.78
25%	286.42	269	0.792	0.122	0.913	0.149	1.71	8.65
50%	309.76	276	0.562	0.360	0.922	0.190	2.44	7.78
75%	280	280	0.278	0.632	0.910	0.090	1.00	8.98
100%	301	271	0	0.835	0.835	0.204	1.24	16.47

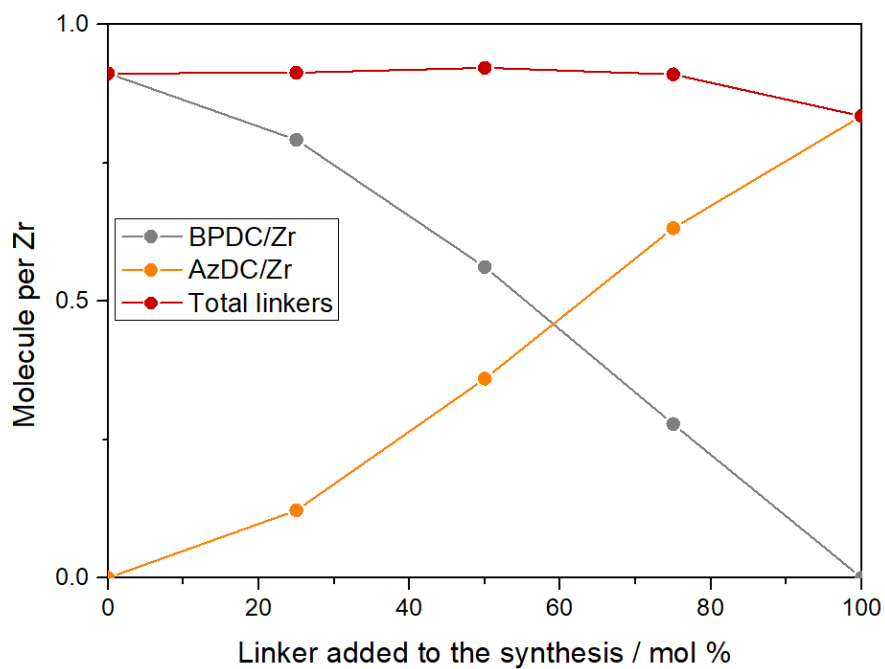


Figure S38: Composition of the MOFs (per Zr) as a function of the percentage of linker added to the synthesis.

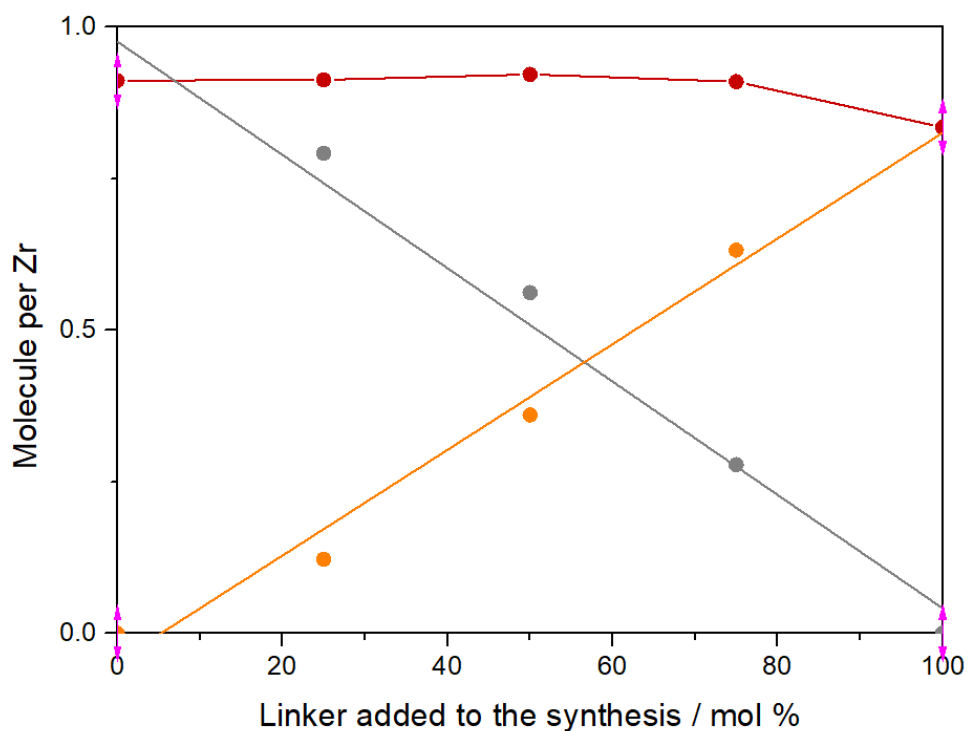


Figure S39: Composition of the MOFs (per Zr) as a function of the percentage of linker added to the synthesis.

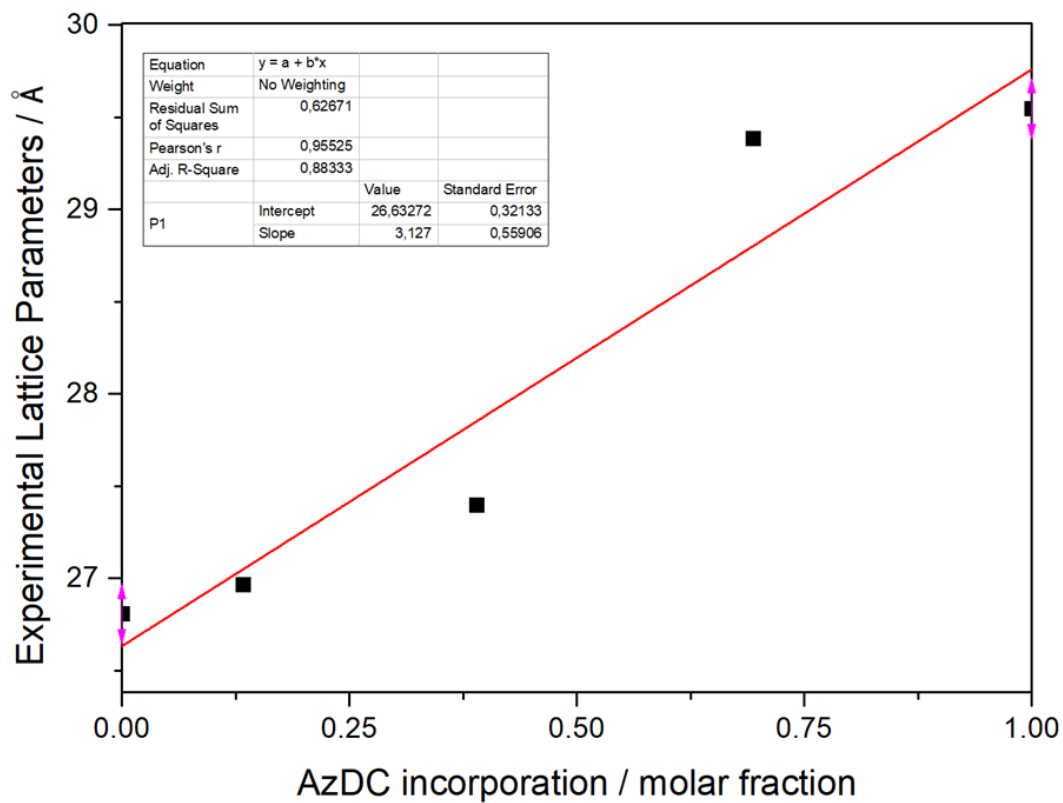


Figure S40: Variation of the unit cell parameters with the AzDC per Zr in the structure.

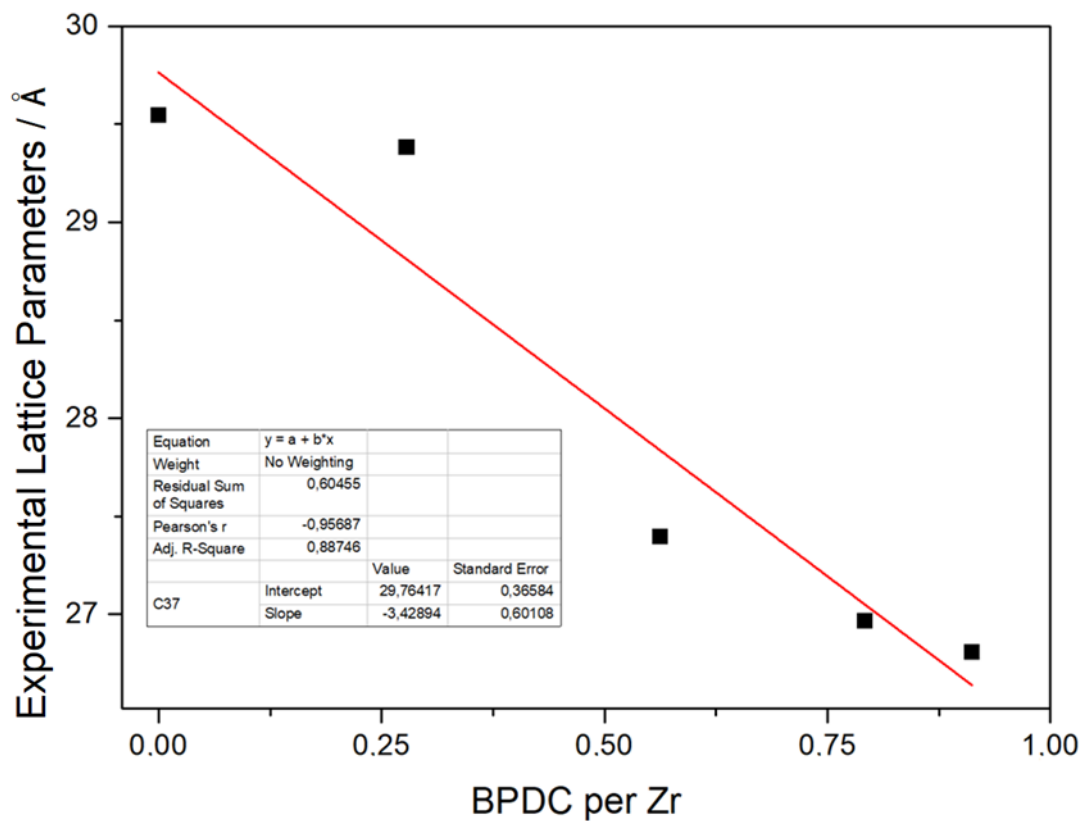


Figure S41: Variation of the unit cell parameters with the BPDC per Zr in the structure.

S.3.5 Nitrogen Adsorption and Desorption Measurements

Table S8: Tabulated data extracted from N₂ adsorption and desorption measurements of MTVMOFs showing a general increase in surface area, microporosity and total pore volumes.

Sample	S _{BET}	S _{MICRO}	S _{EXT}	V _{TOTAL}	V _{MICRO}	V _{MESO}
	(m ² /g)	(m ² /g)	(m ² /g)	(cm ³ /g)	(cm ³ /g)	(cm ³ /g)
0%	2586	2348	239	1.006	0.838	0.168
25%	2780	2597	183	1.067	0.963	0.104
50%	3137	2847	290	1.007	0.894	0.113
75%	2692	2391	301	1.031	0.841	0.19
100%	3511	2972	539	1.243	0.896	0.347

Note that in all cases S_{BET} corresponds to Brunauer–Emmett–Teller surface area. S_{micro} to micropore surface area. S_{ext} to the external surface area. V_{micro} to micropore volume. V_{meso} to mesopore volume and V_{total} to total pore volume.

V_{micro} was calculated using the *t*-plot model with the Harkins and Jura thickness curve based on the BET surface areas. V_{total} was calculated at $P/P_0 = 0.9$. before the inter-particle space and $V_{meso} = V_{total} - V_{micro}$. The pore size distributions were calculated by applying different models, for which the smaller error was for N₂ DFT model.

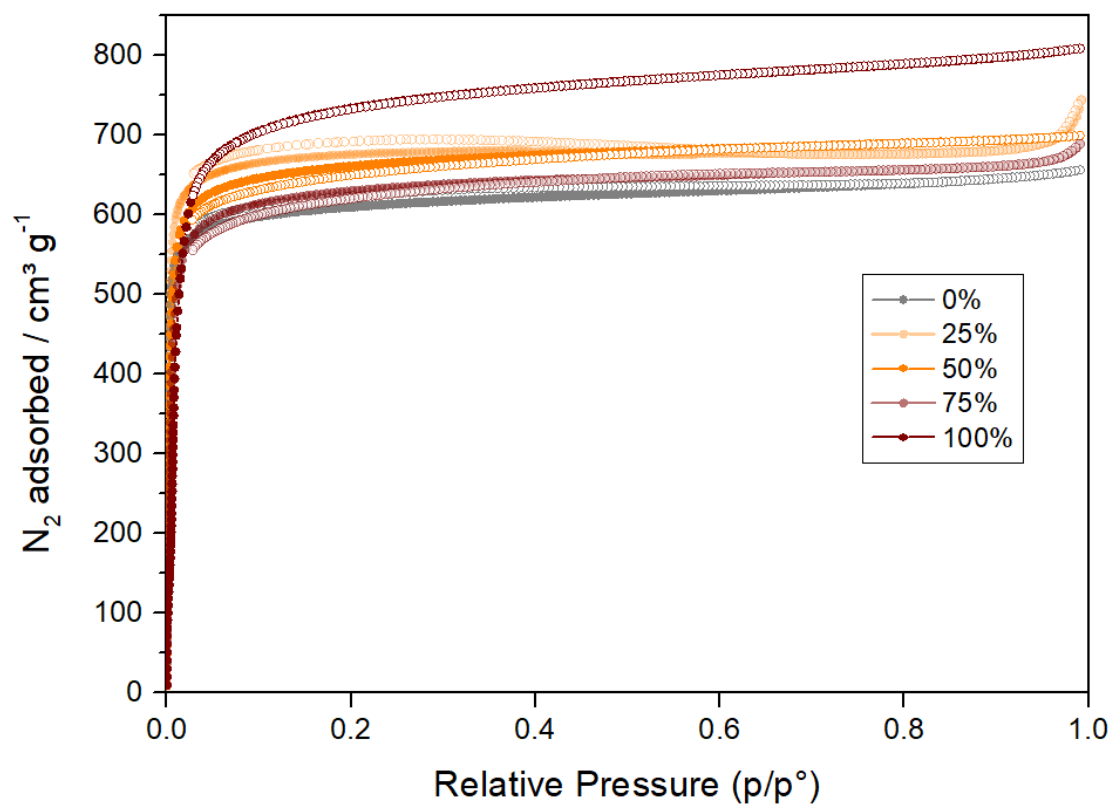


Figure S42: N₂ adsorption and desorption isotherms of MTVMOFs compared to pristine UiO-67 (0%) and UiO-AzDC (100%).

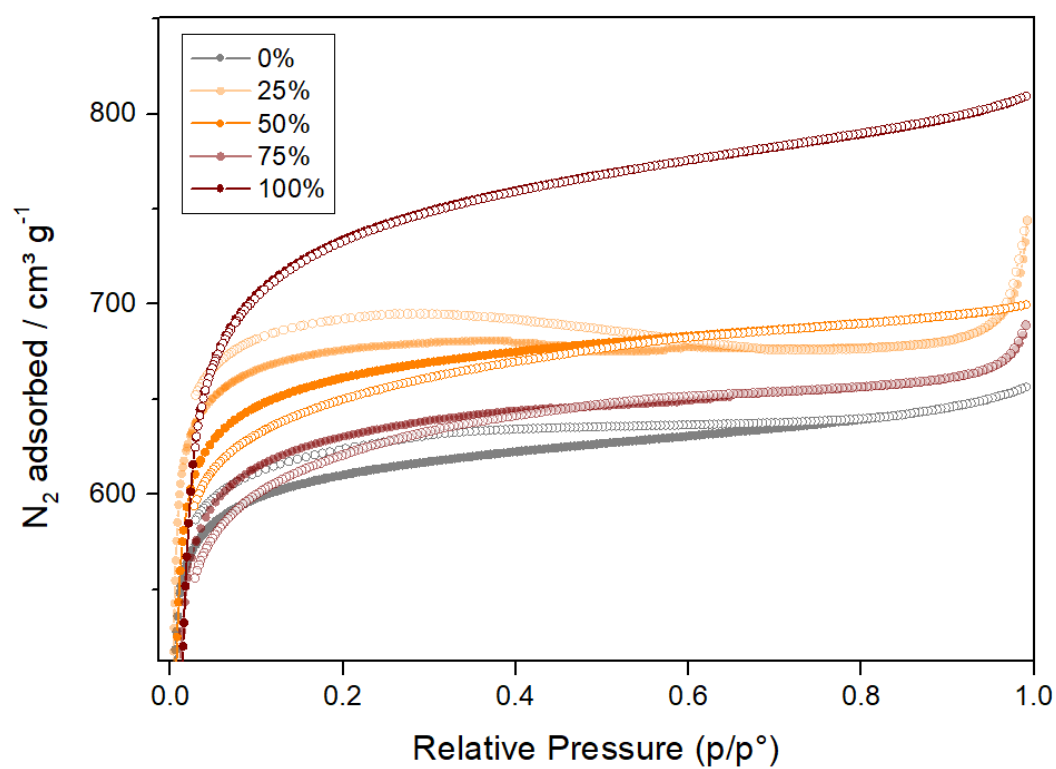


Figure S43: Amplification of the N₂ adsorption and desorption isotherms of MTVMOFs compared to pristine UiO-67 (0%) and UiO-AzDC (100%).

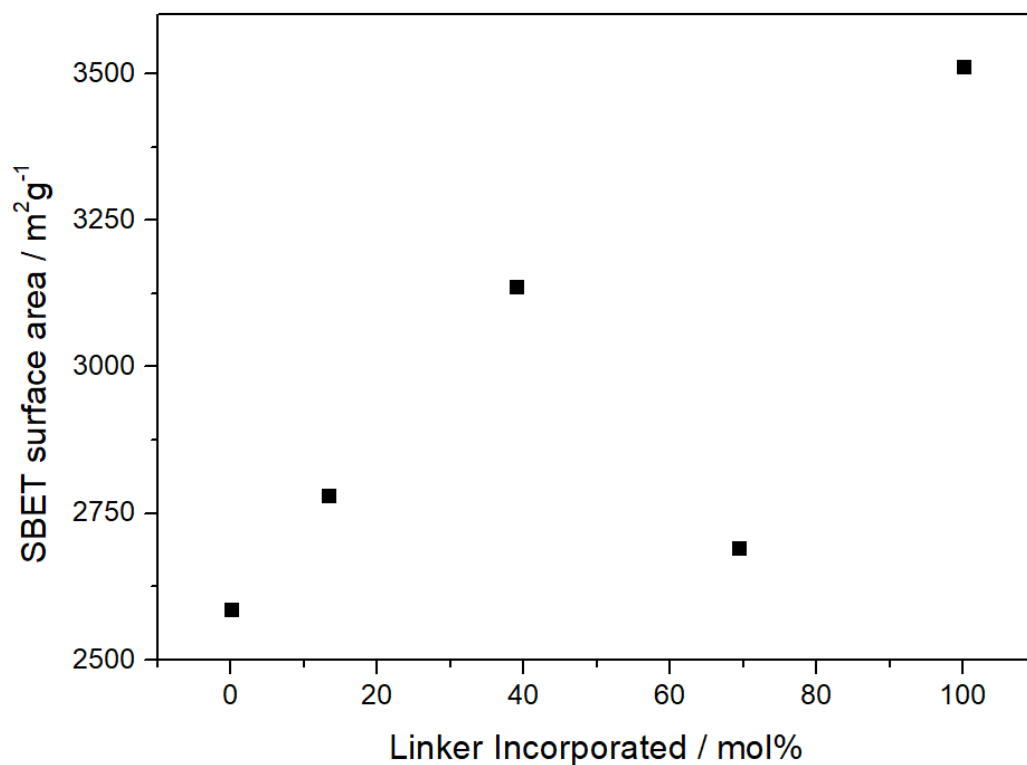


Figure S44: Representation of the SBET as a function of the molar percent of linker incorporated.

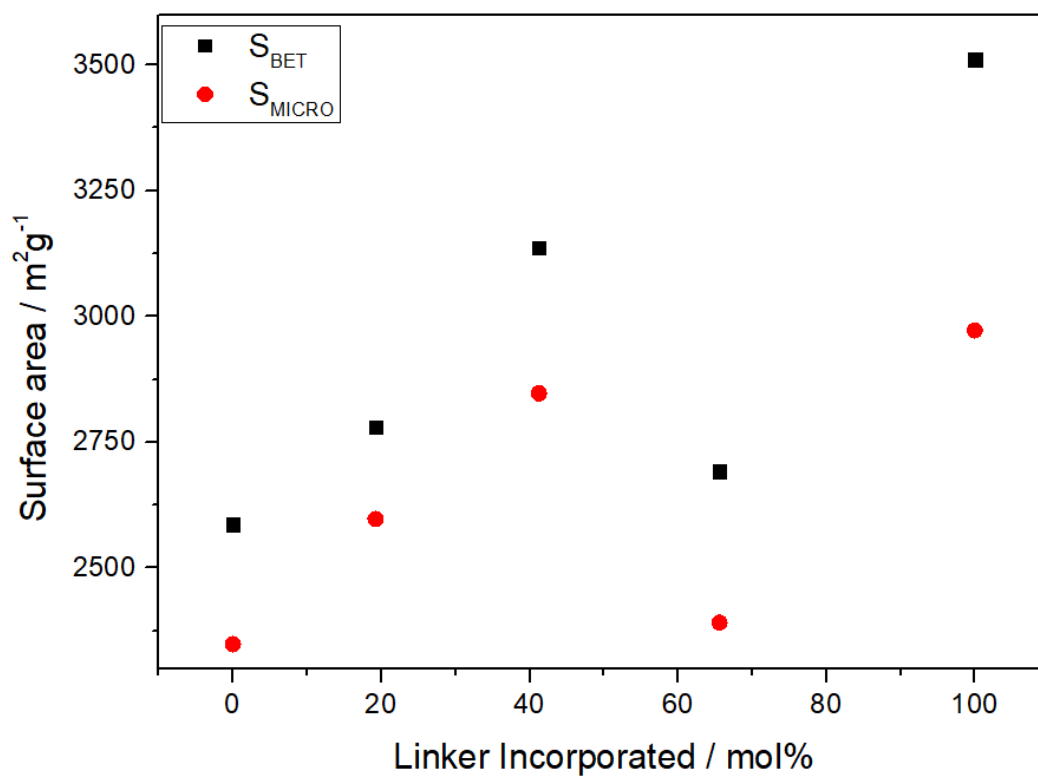


Figure S45: Representation of the SBET and SMICRO as a function of the molar percent of linker incorporated.

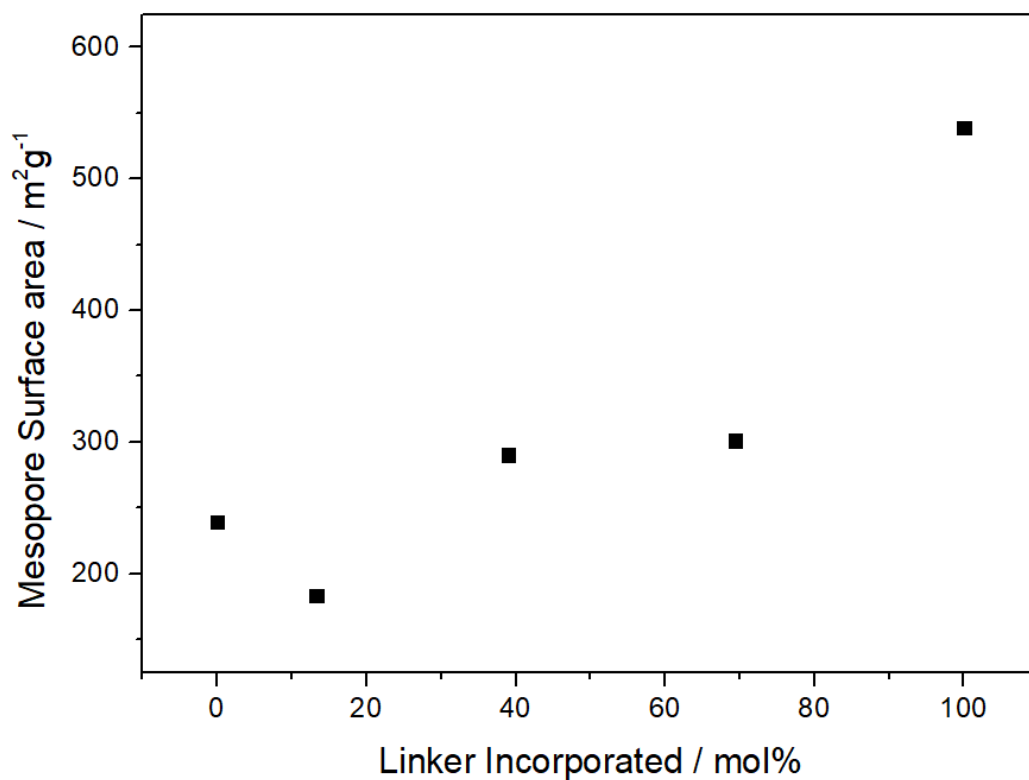


Figure S46: Representation of the mesopore surface area as a function of the molar percent of linker incorporated.

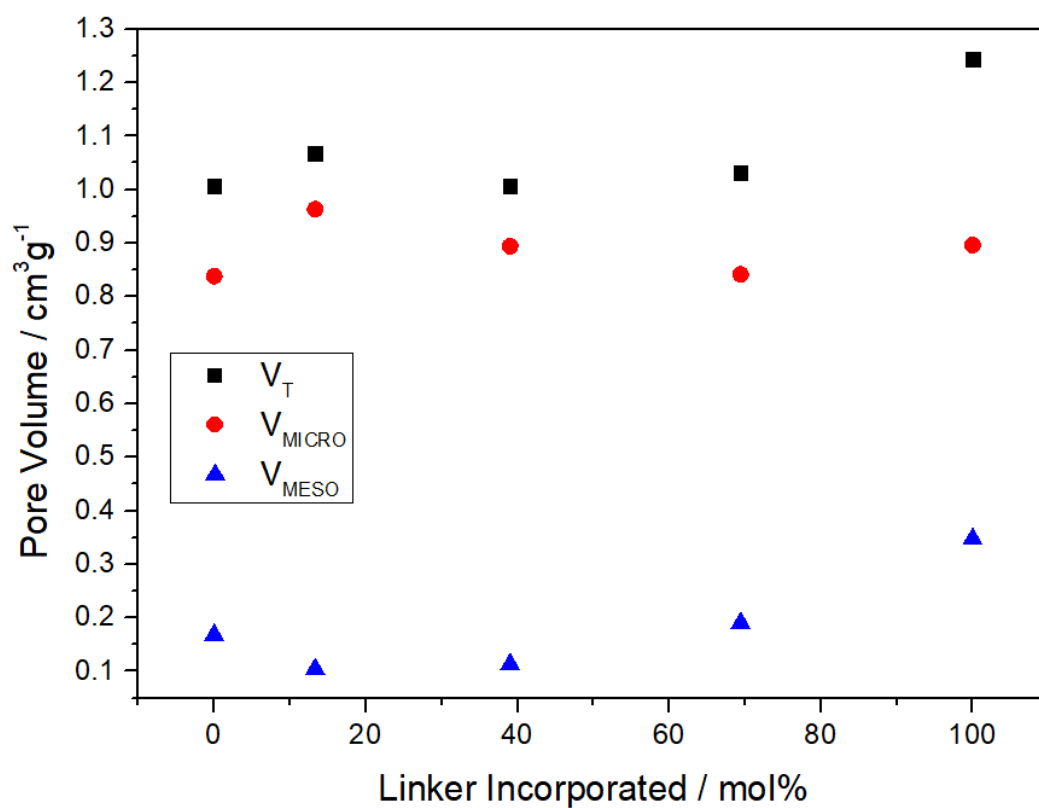


Figure S47: Representation of the pore volumes as a function of the molar percent of linker incorporated.

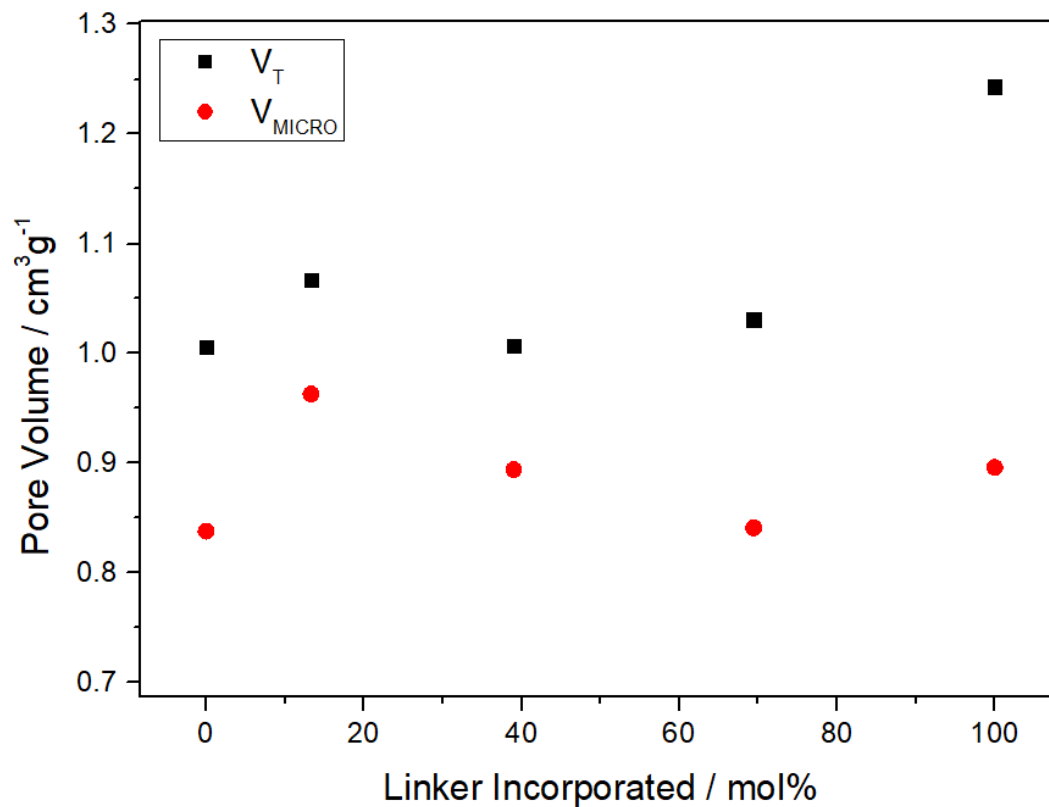


Figure S48: Representation of the total pore and micropore volumes as a function of the molar percent of linker incorporated.

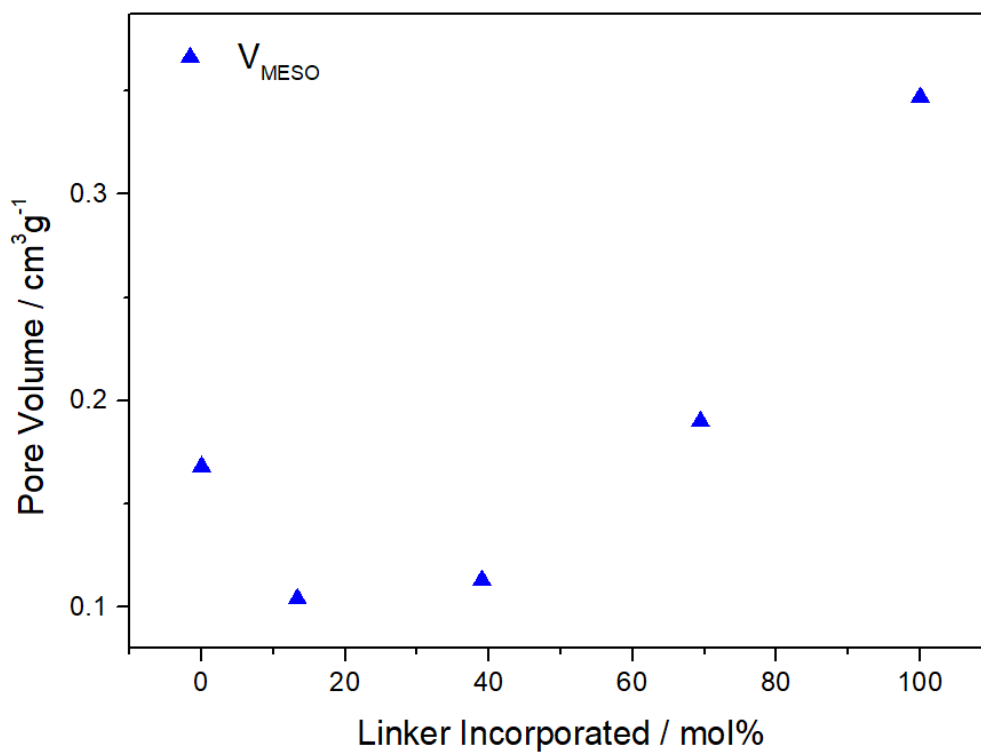


Figure S49: Representation of the mesopore volumes as a function of the molar percent of linker incorporated.

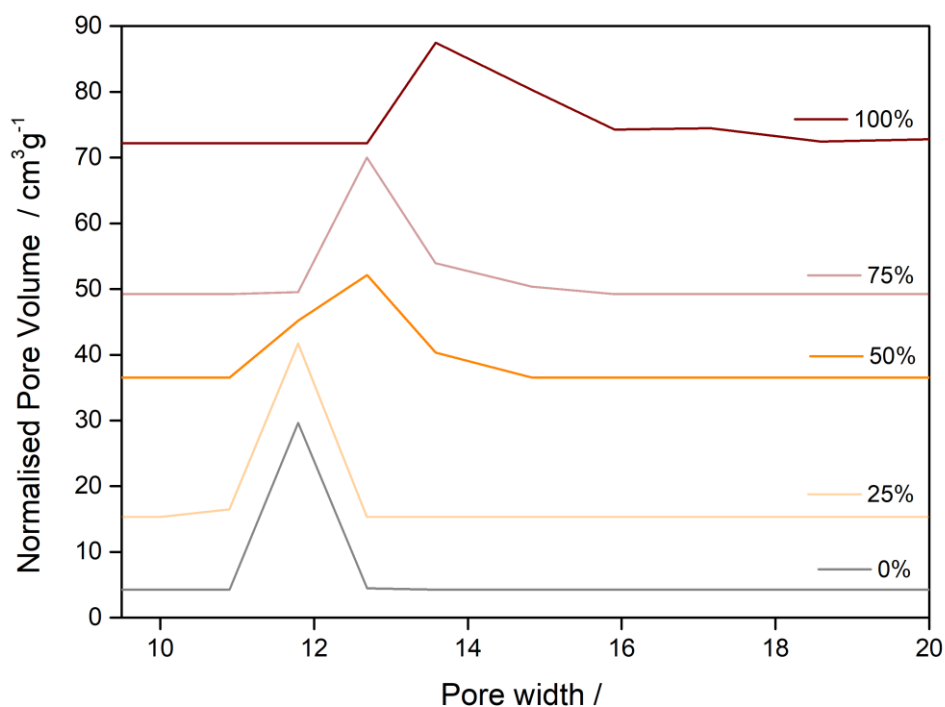


Figure S50: Comparison of pore size distributions of MTVMOFs compared to pristine UiO-67(0%) and UiO-AzDC (100%). Model: N₂ DFT Model.

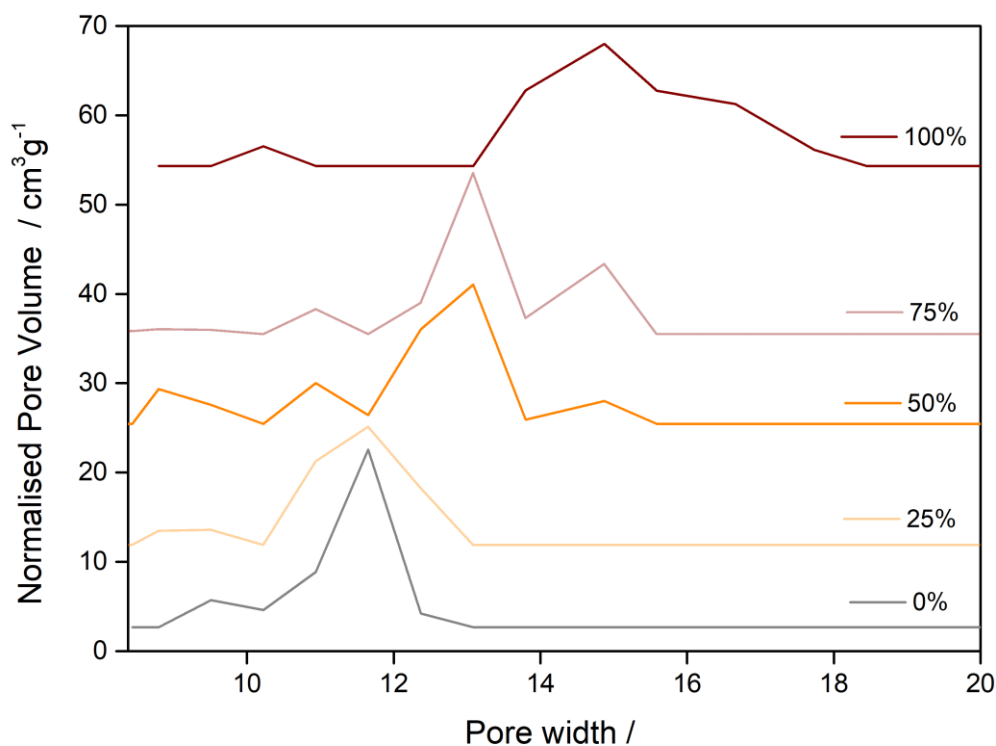


Figure S51: Comparison of pore size distributions of MTVMOFs compared to pristine UiO-67(0%) and UiO-AzDC (100%). Model: N₂-Tarazona NLDFT. Esf = 30.0K.

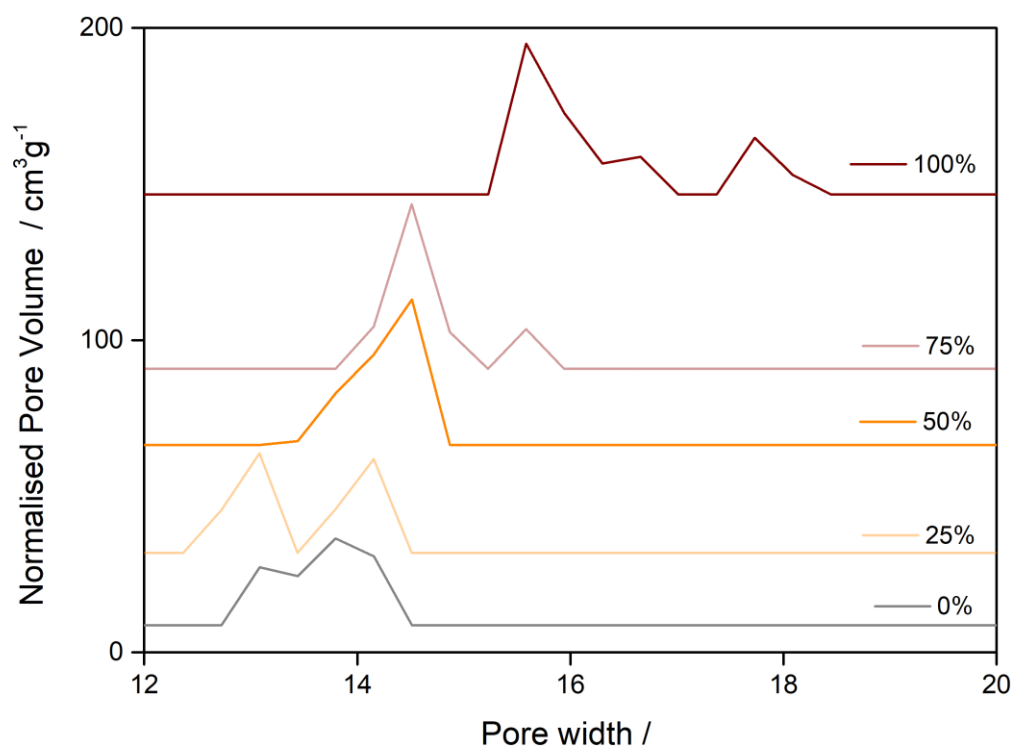


Figure S52: Comparison of pore size distributions of MTVMOFs compared to pristine UiO-67(0%) and UiO-AzDC (100%). Model: NLDFT Pillary Clay.

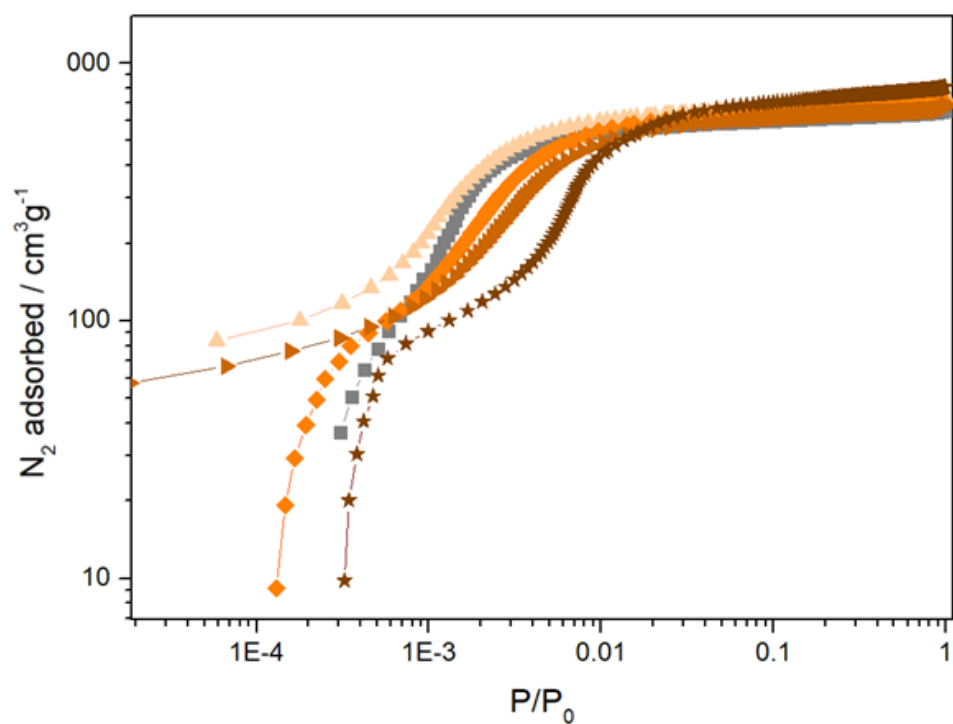


Figure S53: Logarithmic representation N_2 adsorption and desorption isotherms, denoting the differences in the micropore region.

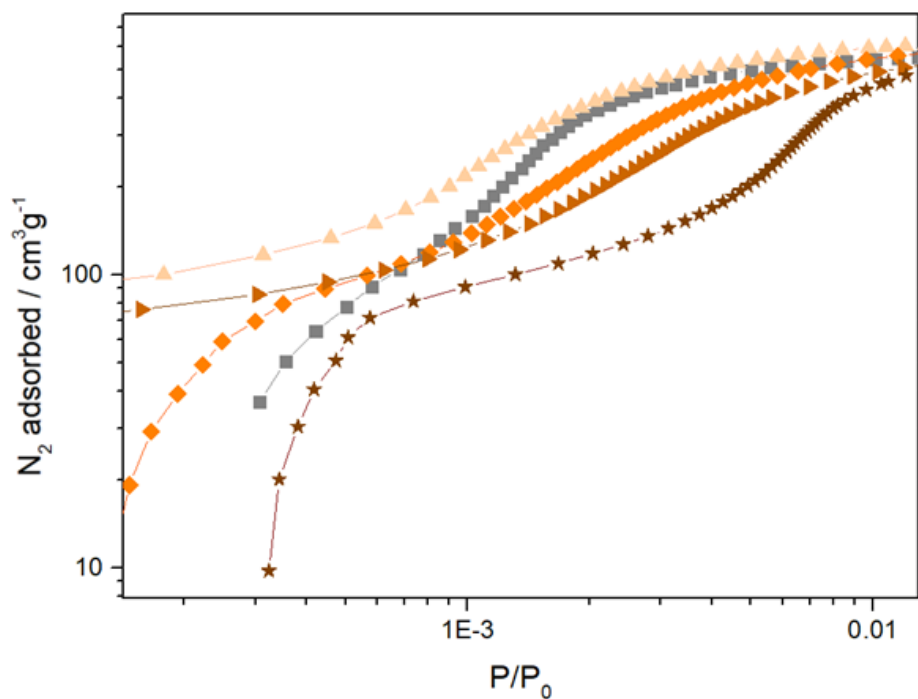


Figure S54: Amplification of the logarithmic representation N_2 adsorption and desorption isotherms, denoting the differences in the micropore region.

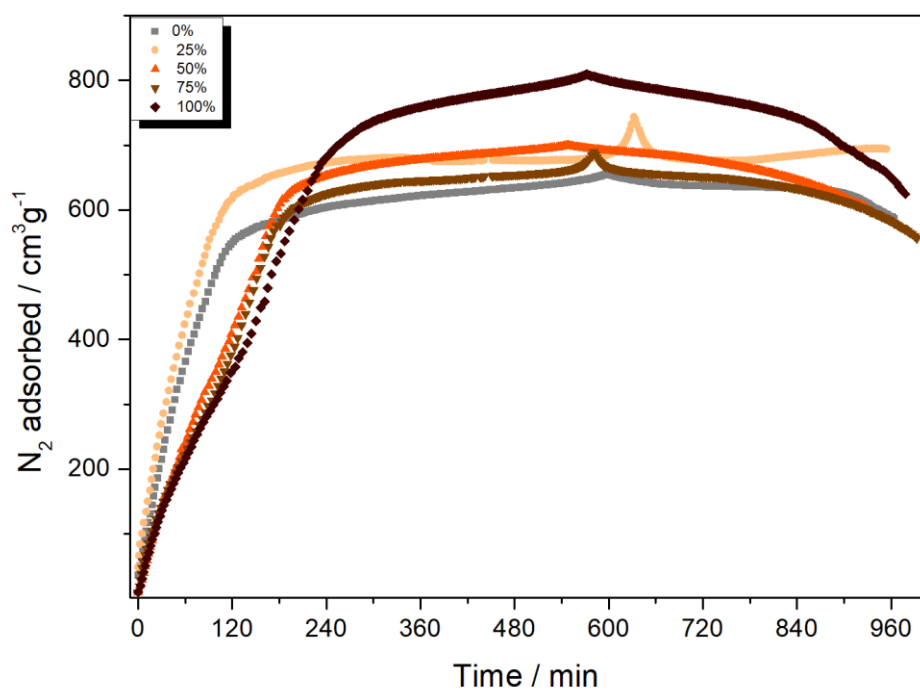


Figure S55: Kinetic profiles of the N_2 adsorption and desorption isotherms.

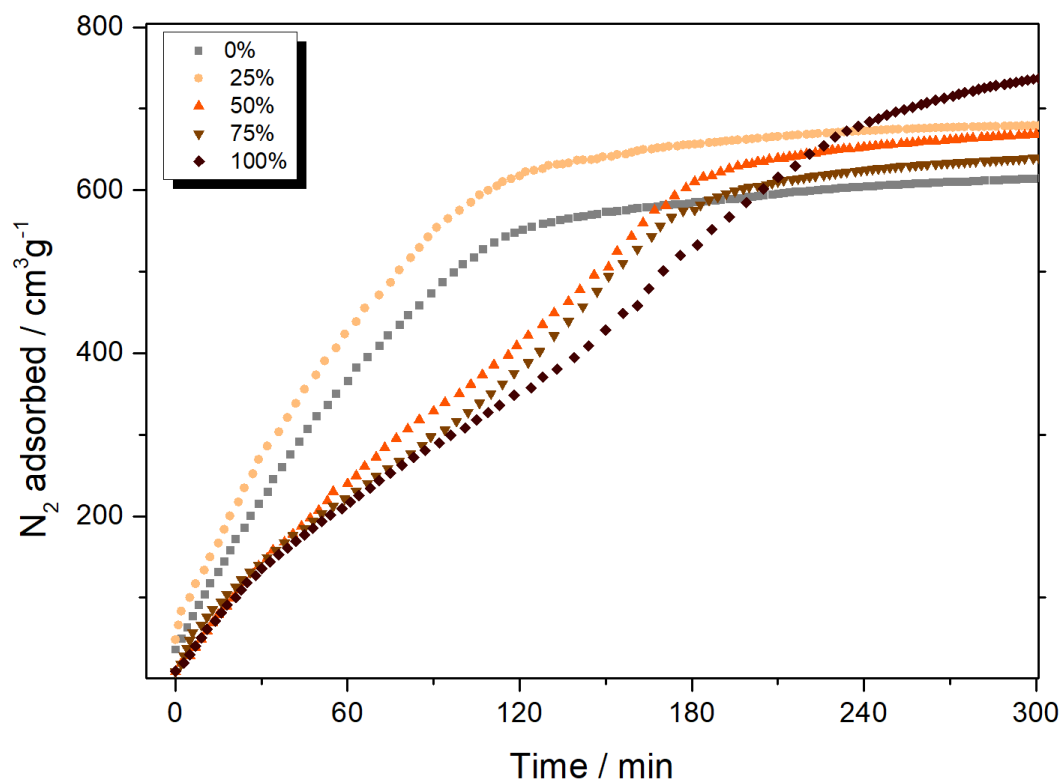


Figure S56: Kinetic profiles of the N₂ adsorption and desorption isotherms.

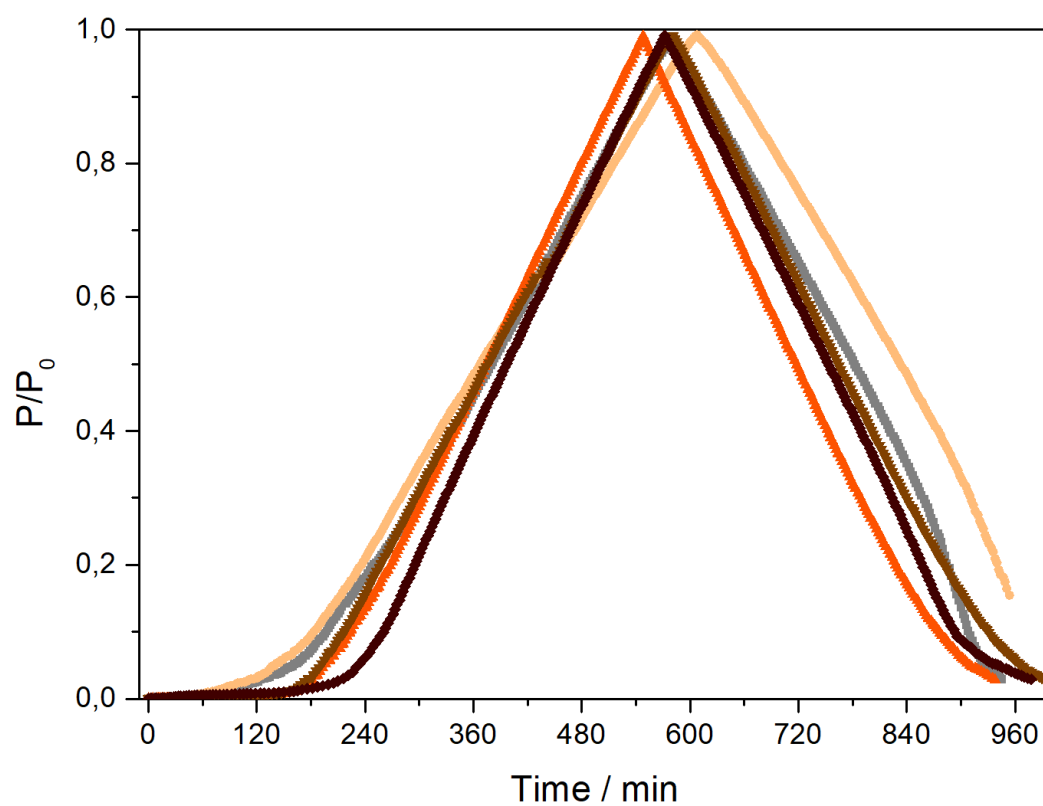


Figure S57: Kinetic profiles of the N₂ adsorption and desorption isotherms.

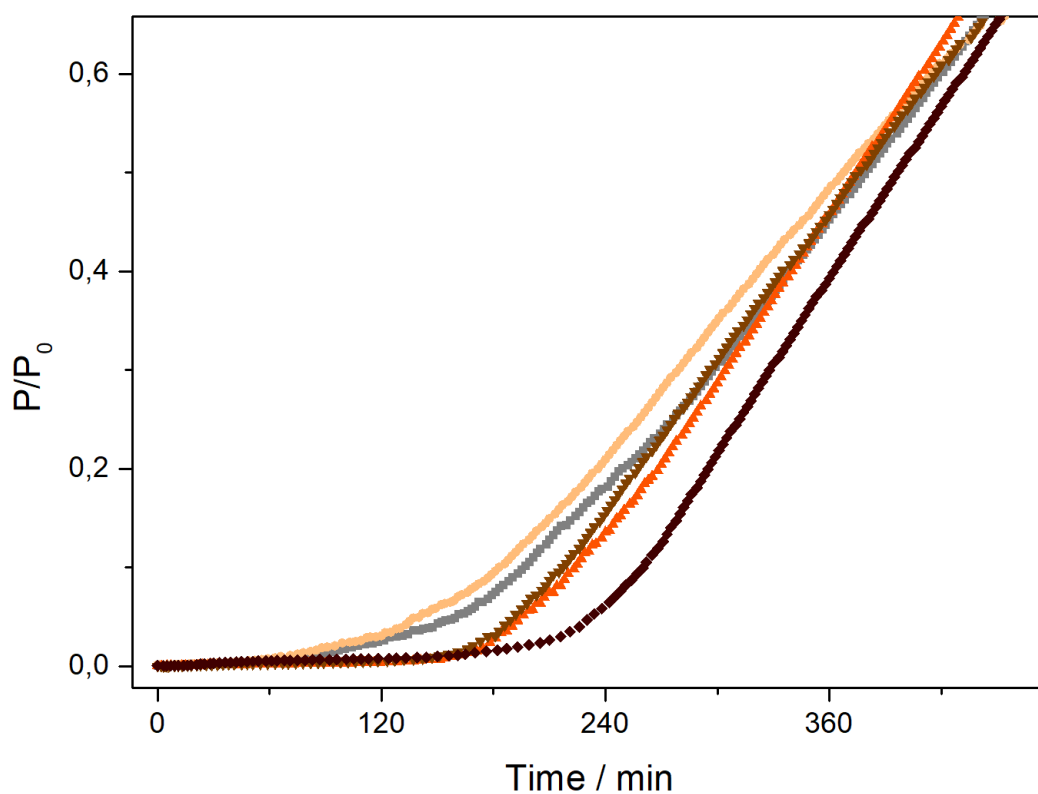


Figure S58: Kinetic profiles of the N_2 adsorption and desorption isotherms.

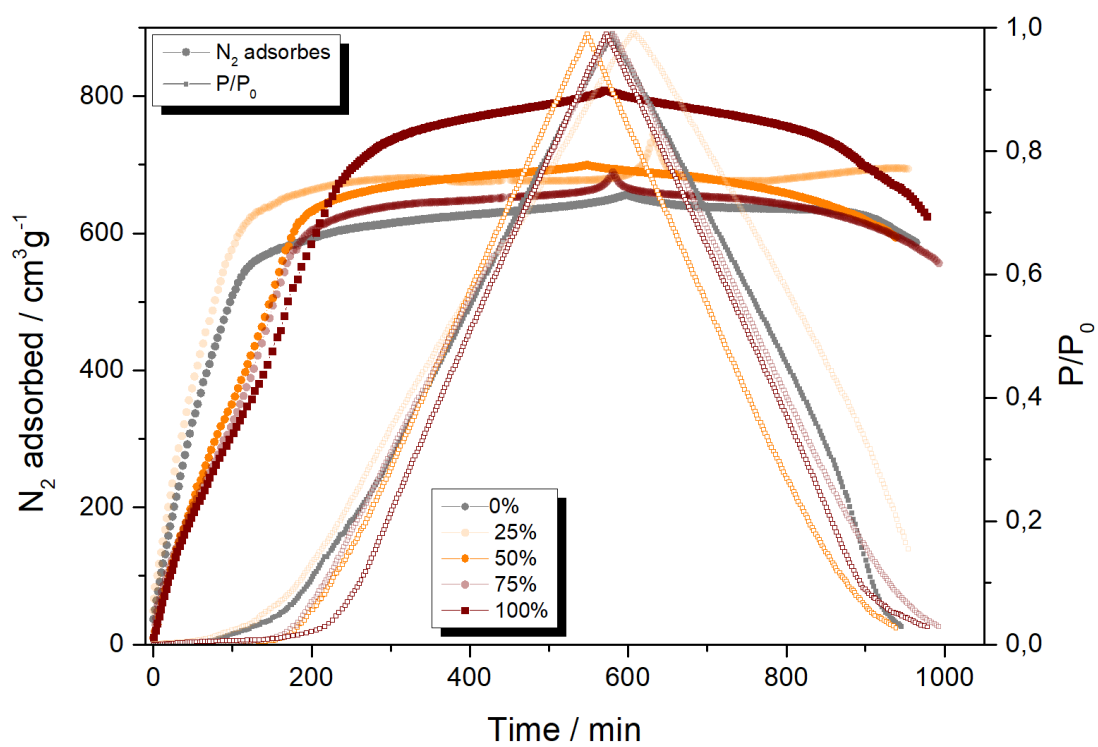


Figure S59: Kinetic profiles of the N_2 adsorption and desorption isotherms.

S.3.6 Scanning Electron Microscopy (SEM)

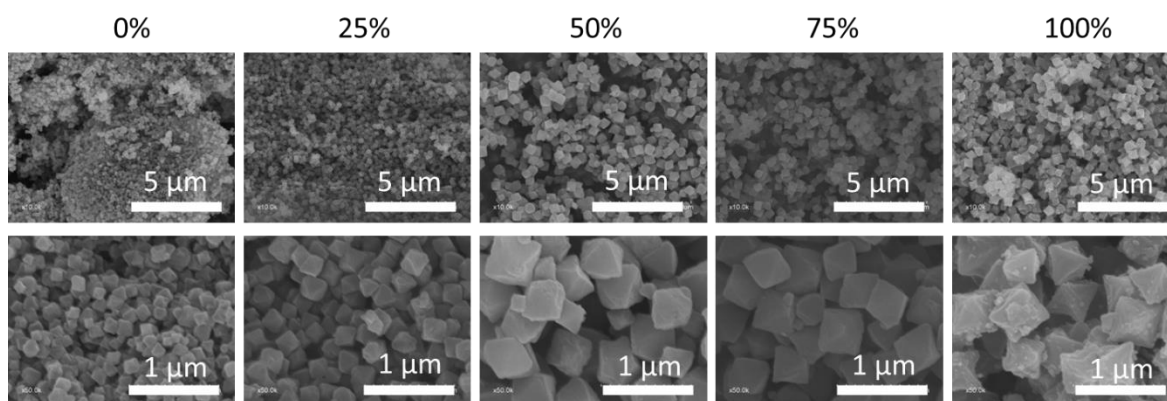


Figure S60: SEM images of MTV MOFs and their pristine analog MOFs.

Table S9: Particle size of the MOFs.

Sample	Particle size / nm	Standard deviation / nm
0%	173.22	22.40
25%	283.40	24.32
50%	633.32	68.29
75%	621.11	57.44
100%	675.96	60.84

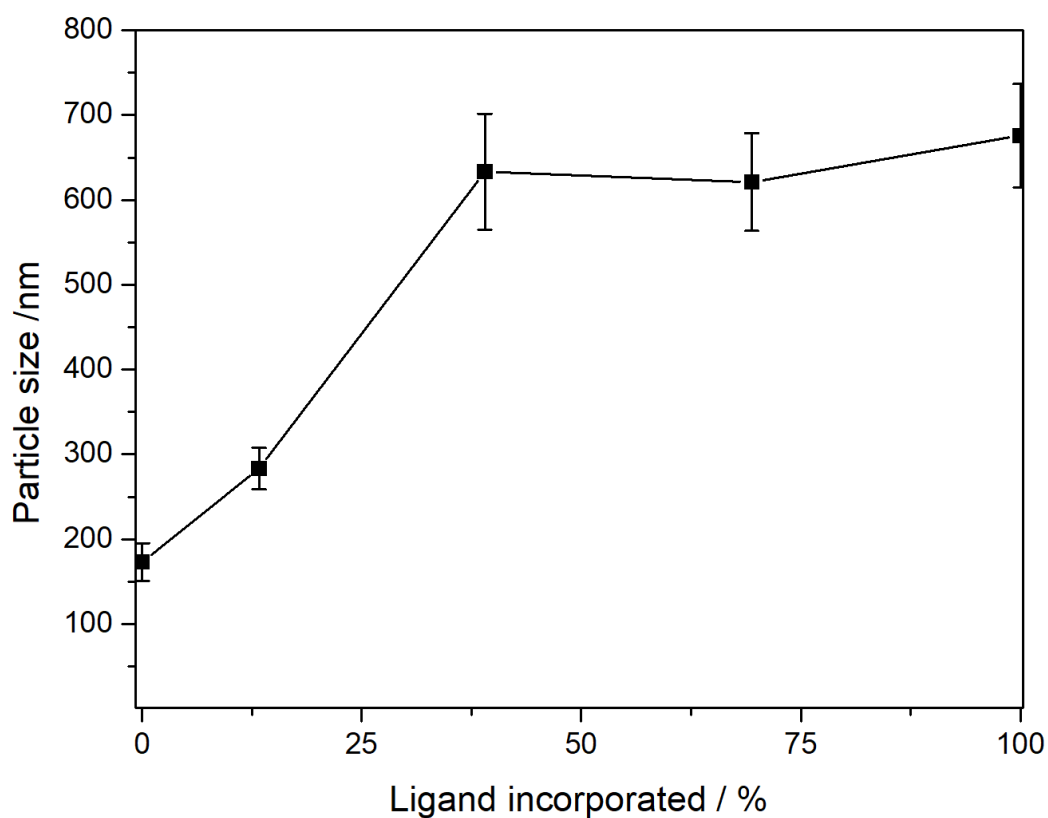


Figure S61: Variation of the particle size as a function of AzDC linker incorporated.

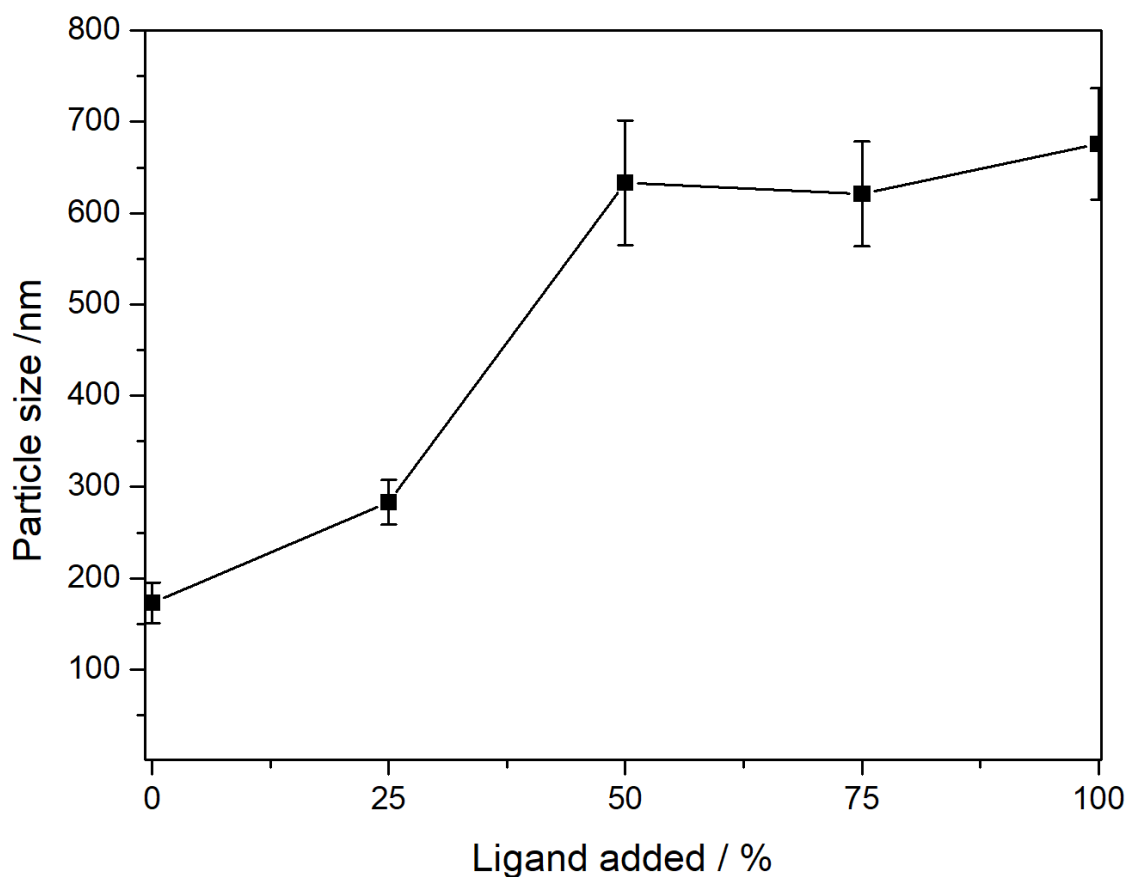


Figure S62: Variation of the particle size as a function of AzDC linker added to the synthesis.

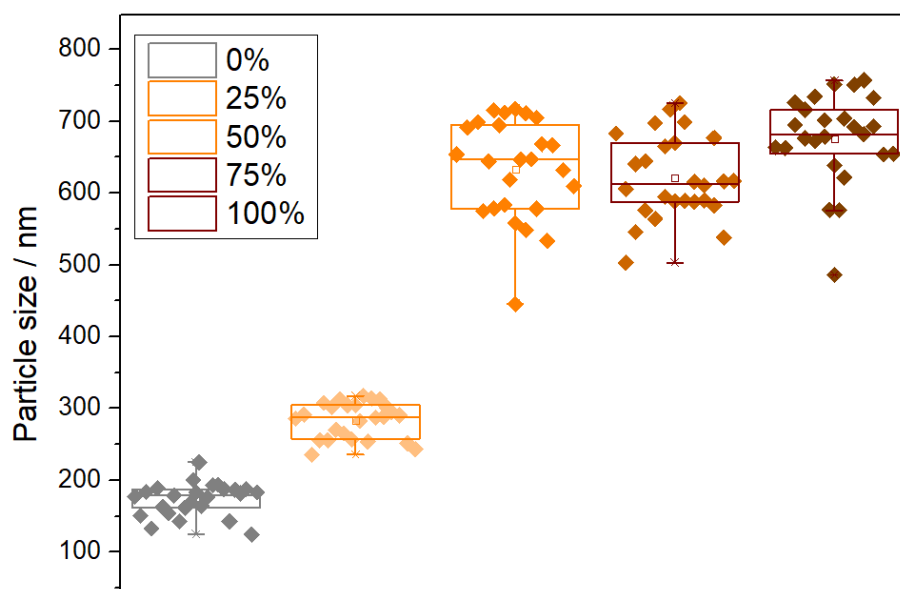


Figure S63: Box chart representation of MTV MOFs' particle sizes. Bin size of 20 nm. Average size and standard deviation. 25% and 75% quartiles.

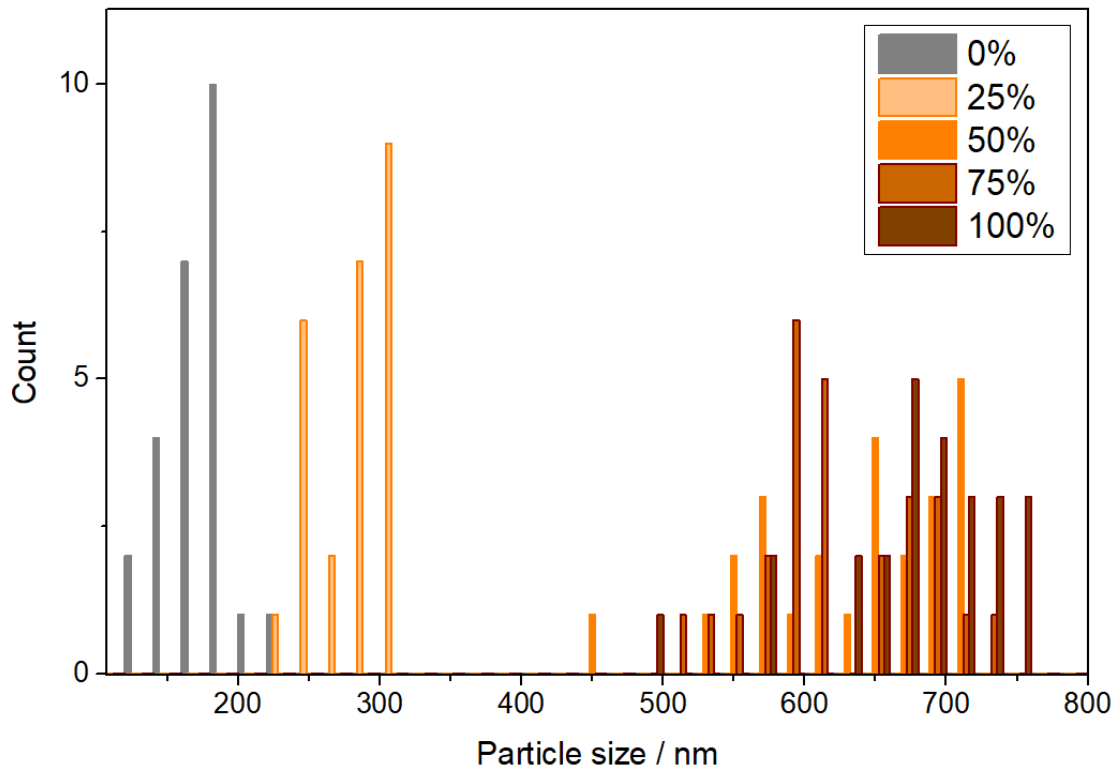


Figure S64: Histogram representation of MTVM MOFs' particle sizes. Bin size of 20 nm.

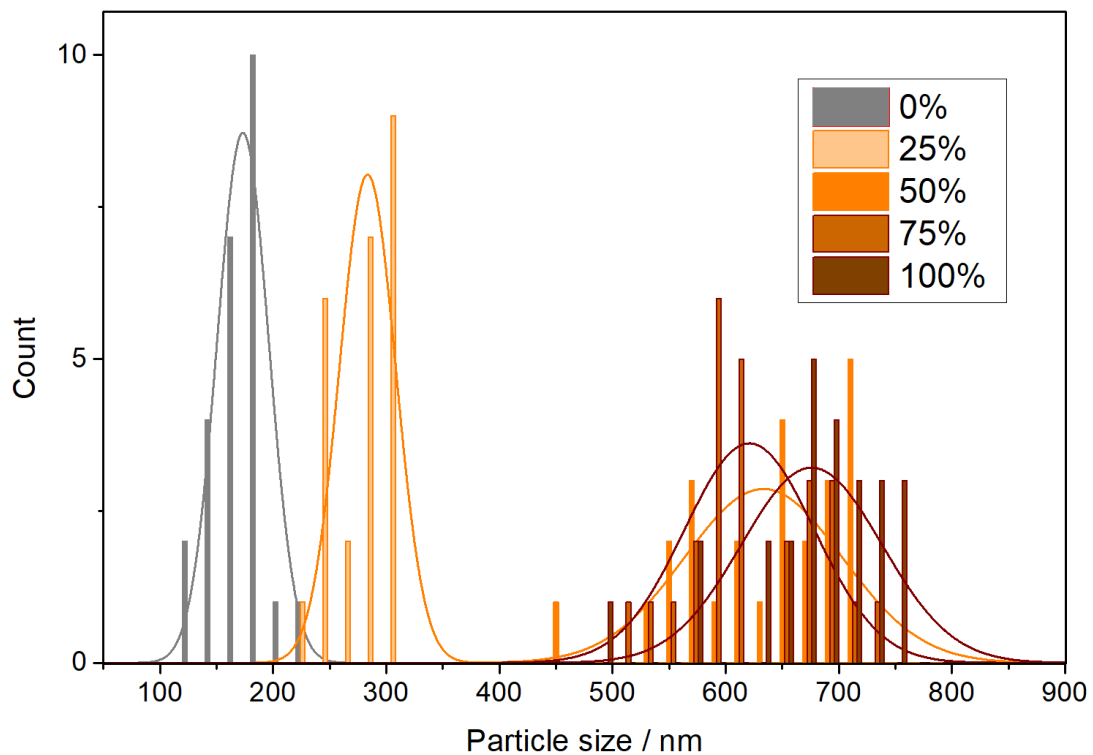


Figure S65: Histogram representation of MTVM MOFs' particle sizes, alongside normal distribution curves. Bin size of 20 nm.

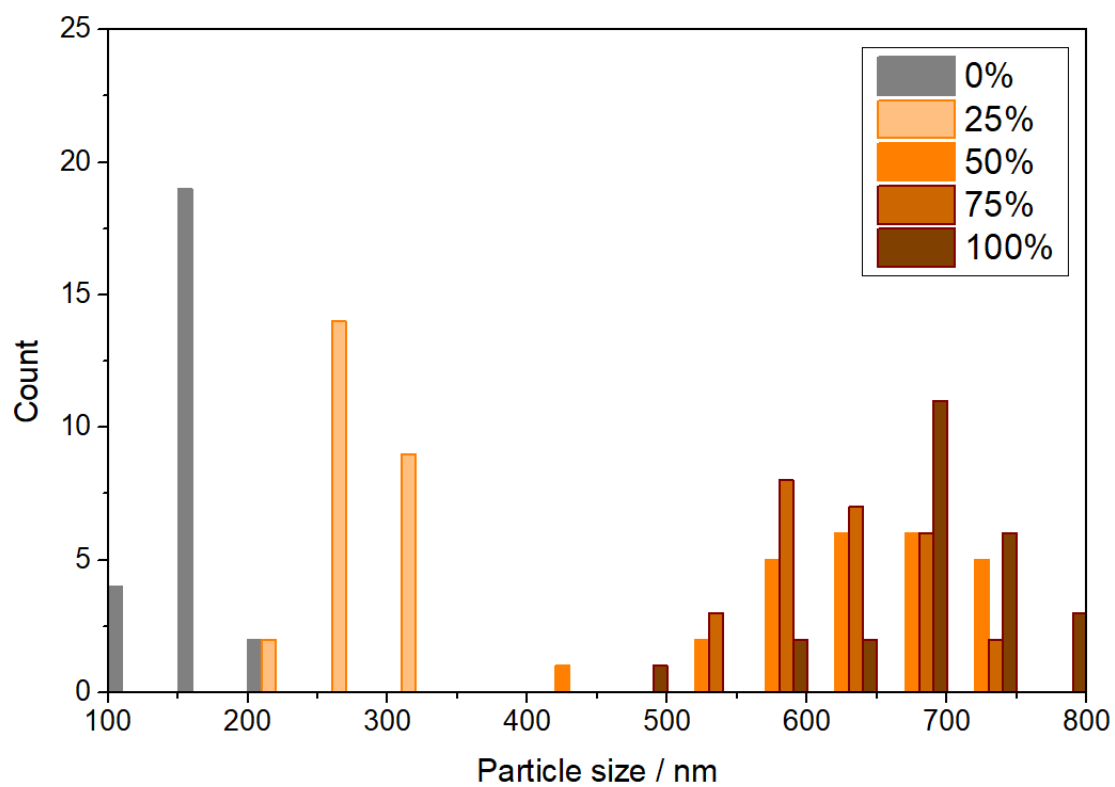


Figure S66: Histogram representation of MTVM MOFs' particle sizes. Bin size of 50 nm.

S.3.7 Z-potential

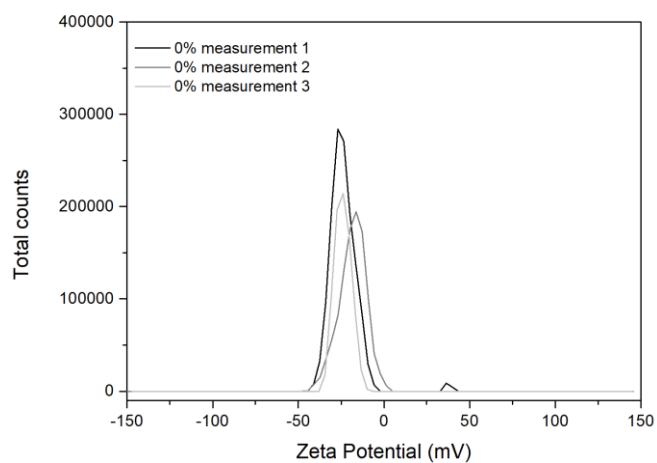


Figure S67: Z-potential of the 0% sample in water.

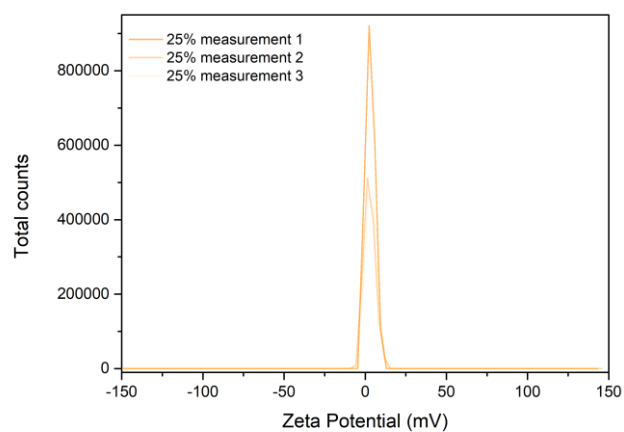


Figure S68: Z-potential of the 25% sample in water.

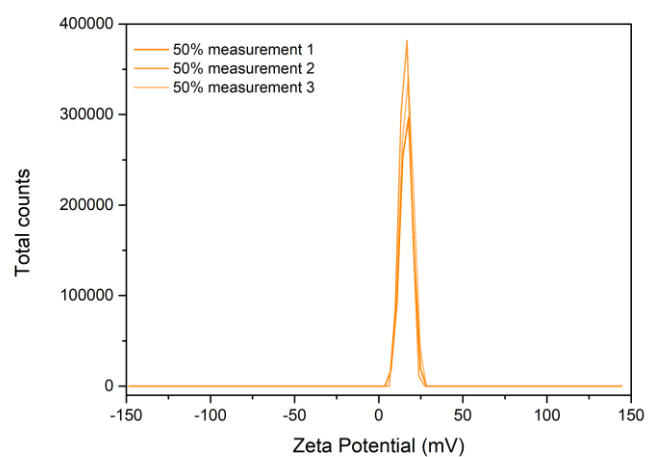


Figure S69: Z-potential of the 50% sample in water.

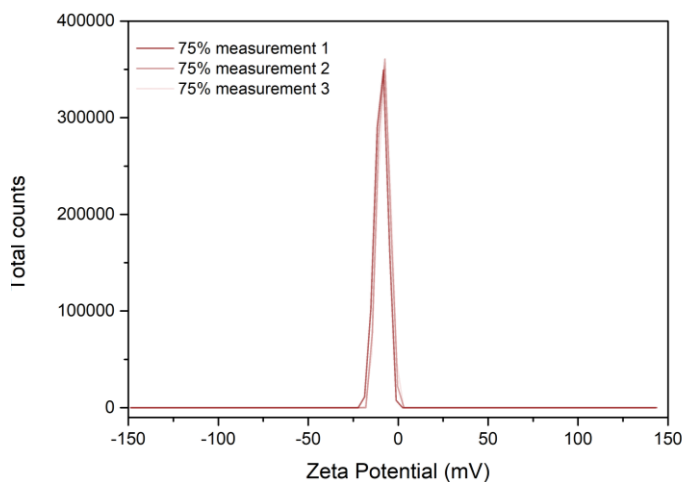


Figure S70: Z-potential of the 75% sample in water.

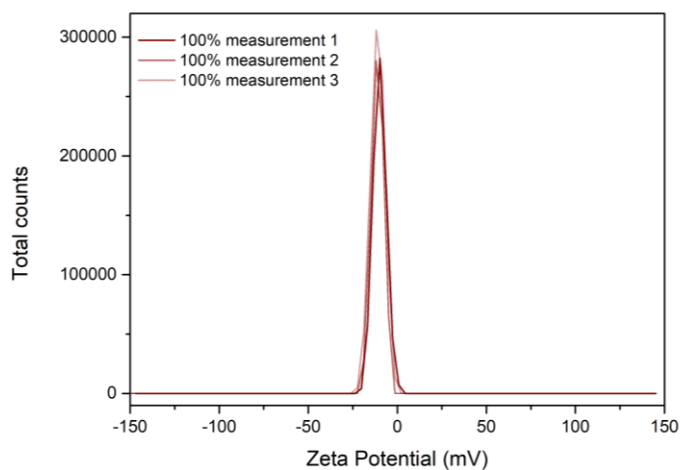


Figure S71: Z-potential of the 100% sample in water.

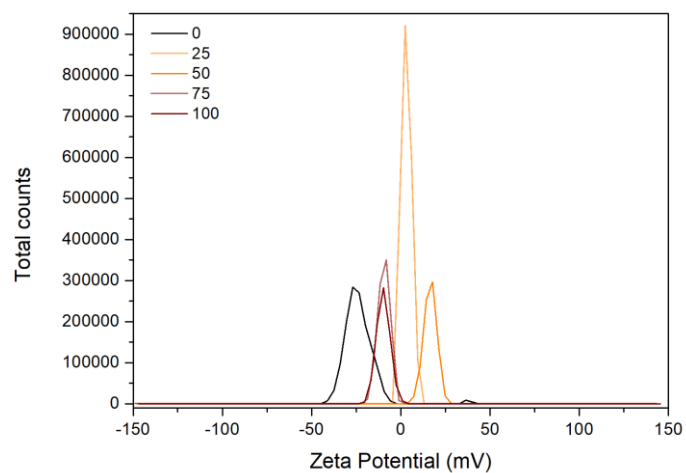


Figure S72: Comparison of the first measurement of Z-potential of MTV samples.

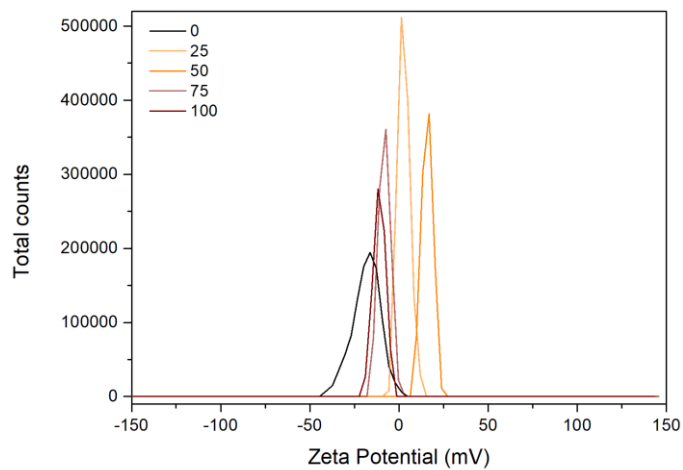


Figure S73: Comparison of the second measurement of Z-potential of MTV samples.

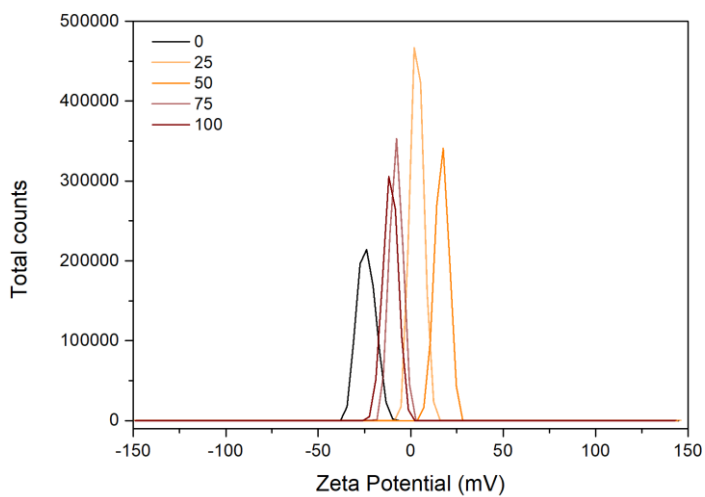


Figure S74: Comparison of the third measurement of Z-potential of MTV samples.

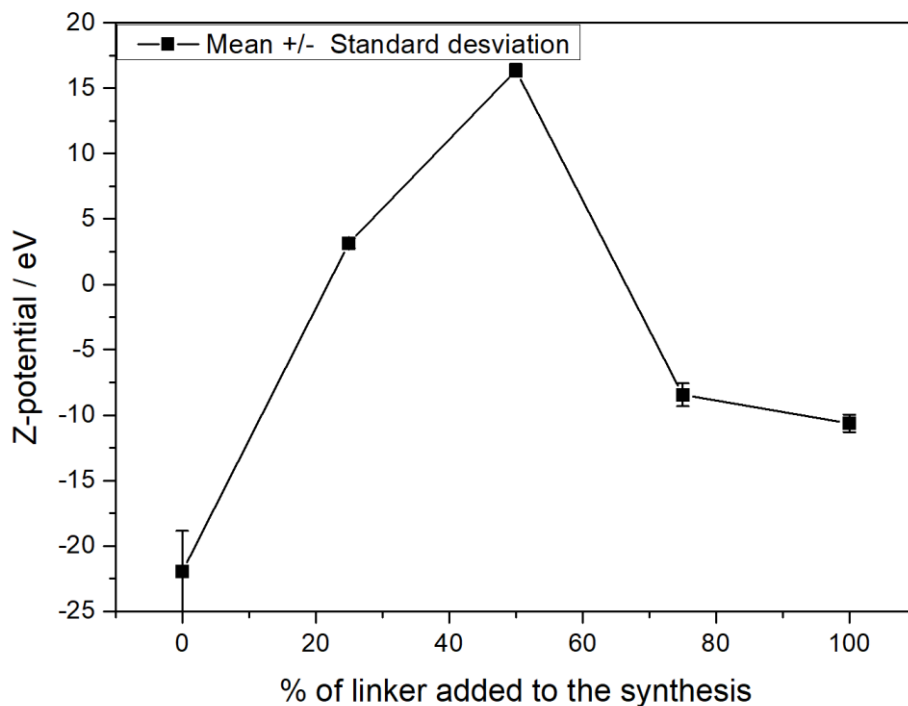


Figure S75: Comparison of the values of Z-potential of MTV samples.

Table S10: Comparison of the values of Z-potential of MTV samples.

Sample	Average Z-potential (eV)	Estandar deviation
0	-21.964	3.117
25	3.137	0.393
50	16.356	0.486
75	-8.445	0.886
100	-10.632	0.669

S.3.8 Dynamic Light Scattering (DLS)

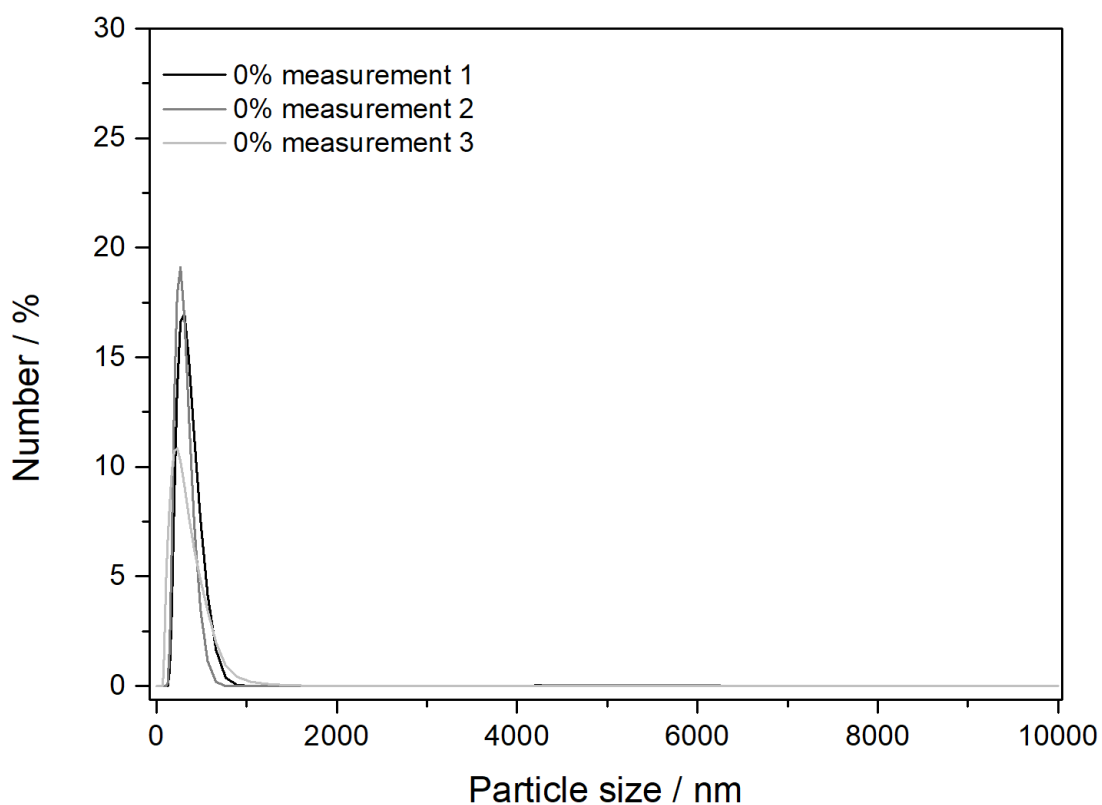


Figure S76: DLS measurements of the 0% samples in water.

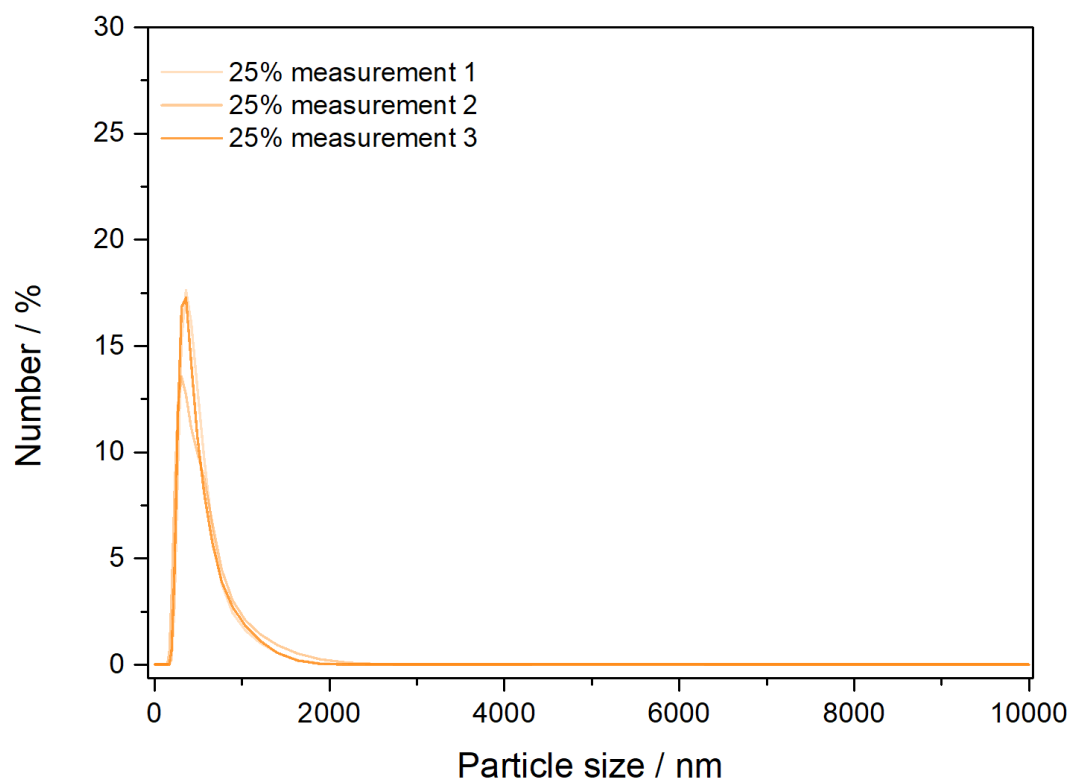


Figure S77: DLS measurements of the 25% samples in water.

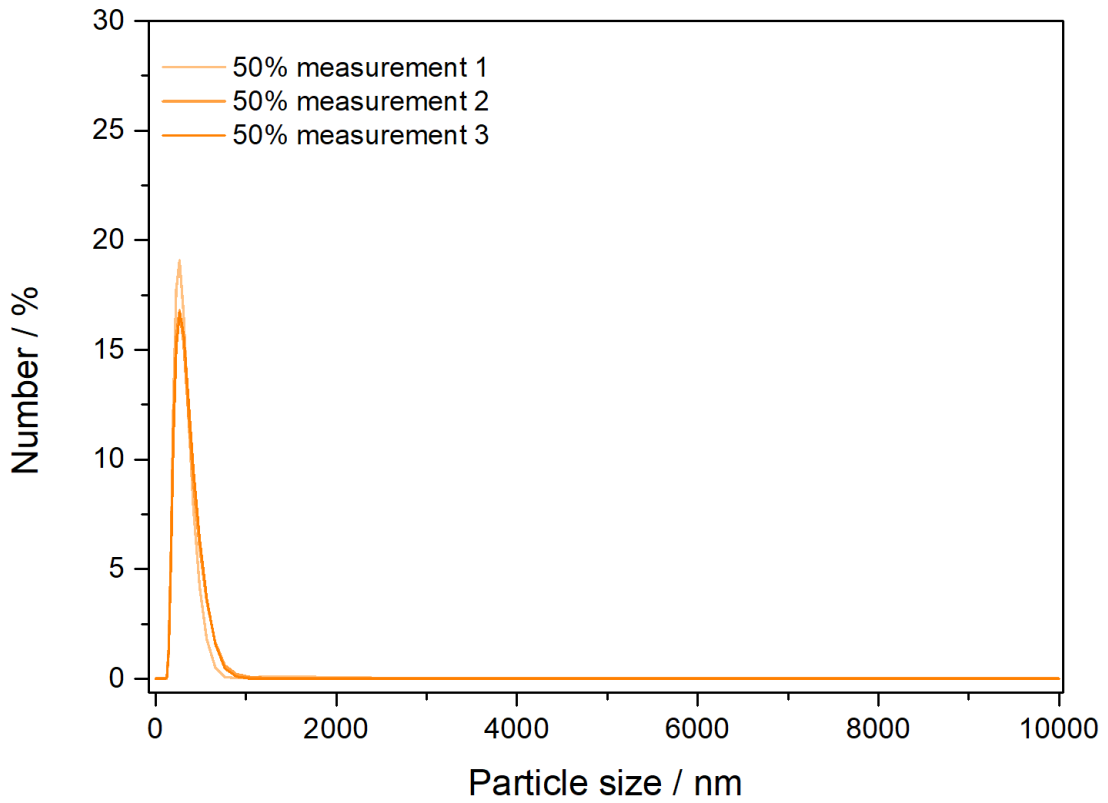


Figure S78: DLS measurements of the 50% samples in water.

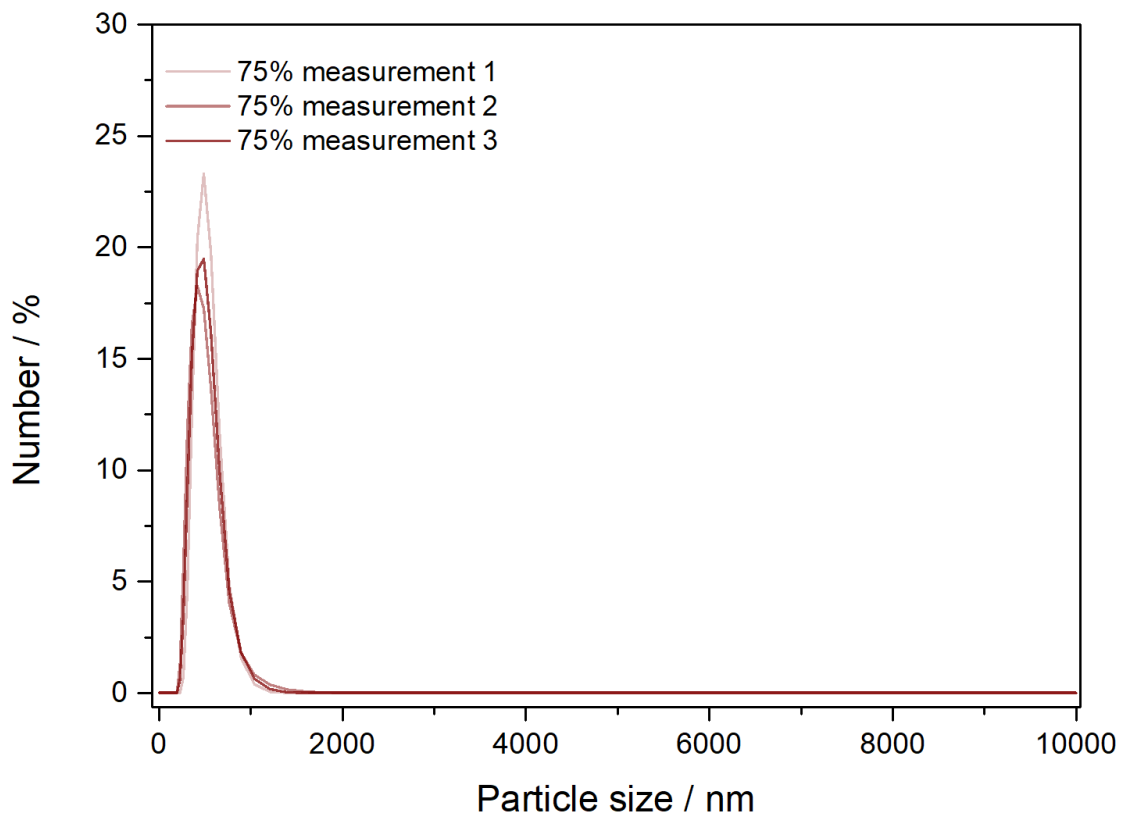


Figure S79: DLS measurements of the 75% samples in water.

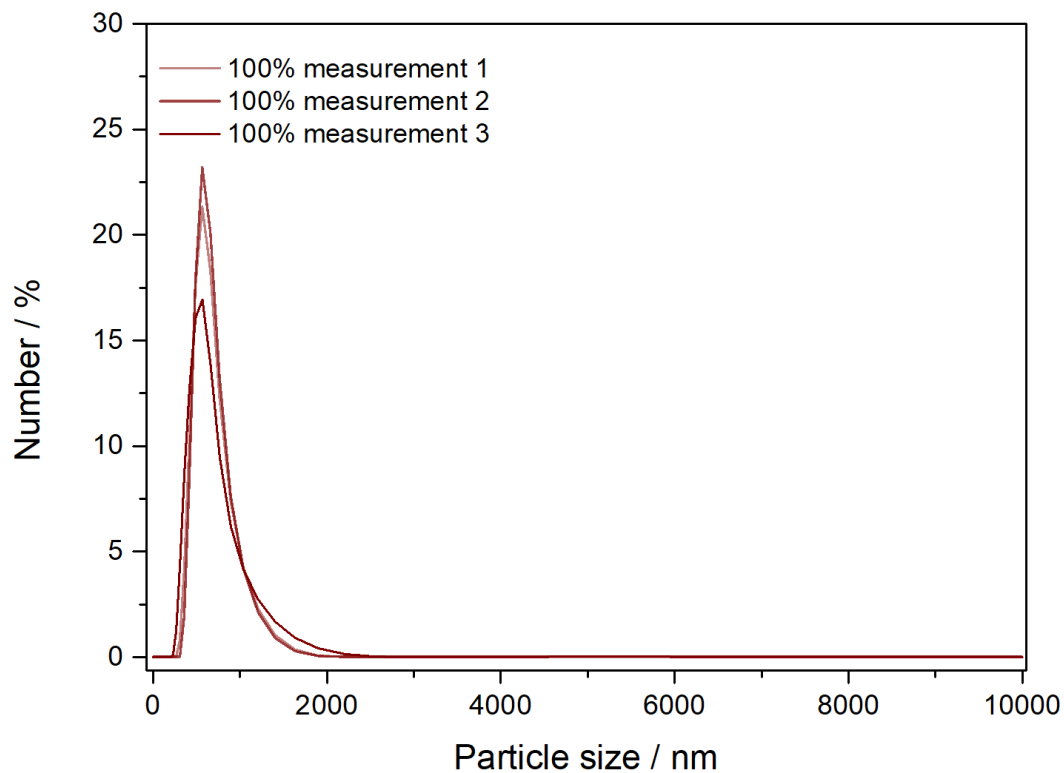


Figure S80: DLS measurements of the 100% samples in water.

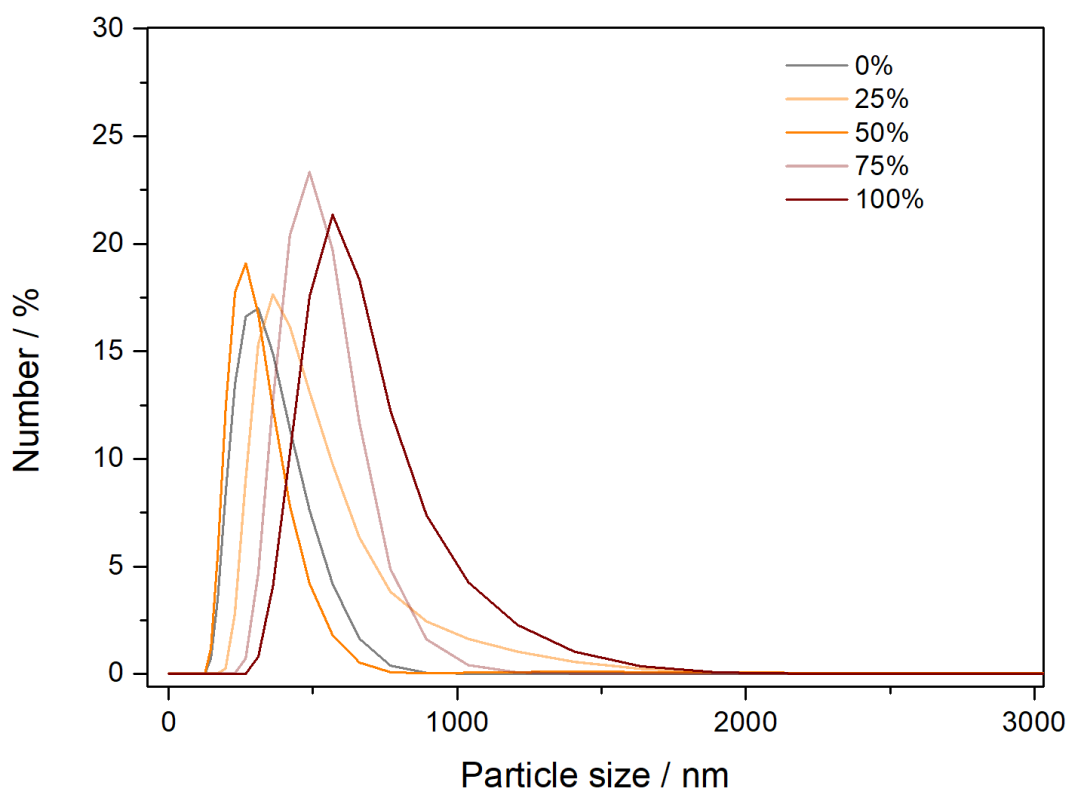


Figure S81: Comparison of the first DLS measurements of the MTV samples in water.

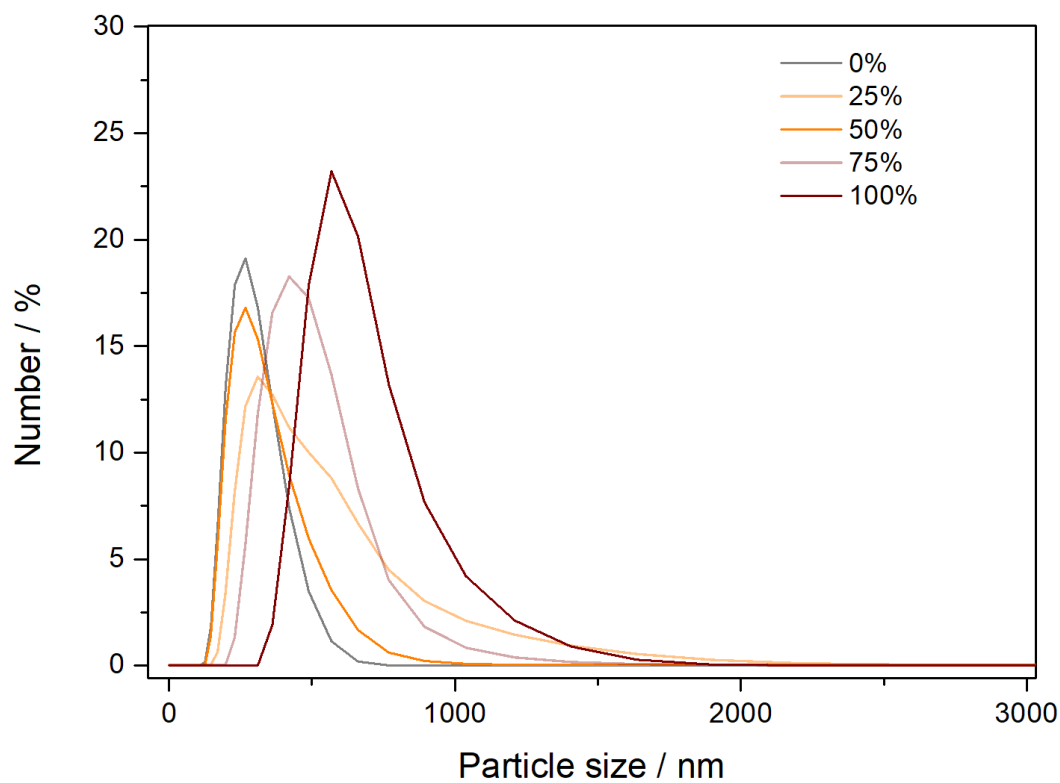


Figure S82: Comparison of the first DLS measurements of the MTV samples in water.

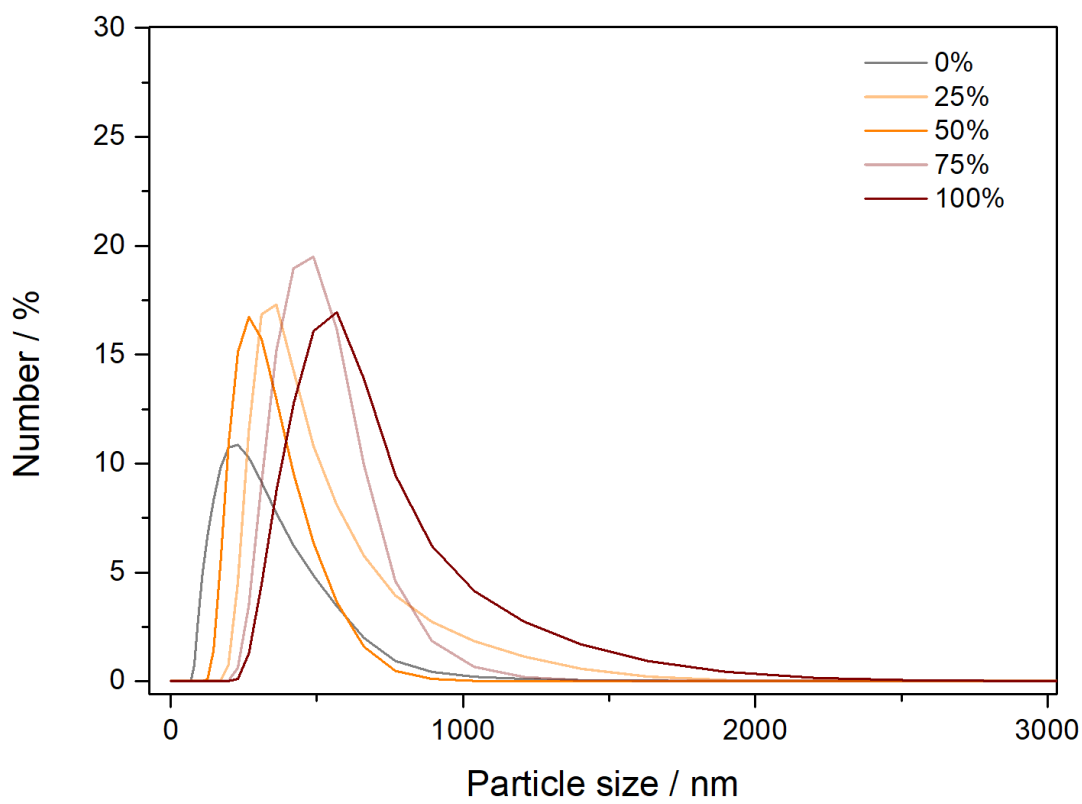


Figure S83: Comparison of the first DLS measurements of the MTV samples in water.

Table S11: Hydrodynamic diameter and polydispersity index of the samples.

Sample	Average particle size / nm	Standard deviation / nm	Mean particle size value / nm	PDI	PDI SD
0%	387.303	78.124	287	0.407	0.287
25%	940.964	28.948	365	0.566	0.051
50%	368.312	37.417	261	0.31	0.071
75%	603.098	25.717	483	0.197	0.026
100%	896.258	76.83	569	0.288	0.011

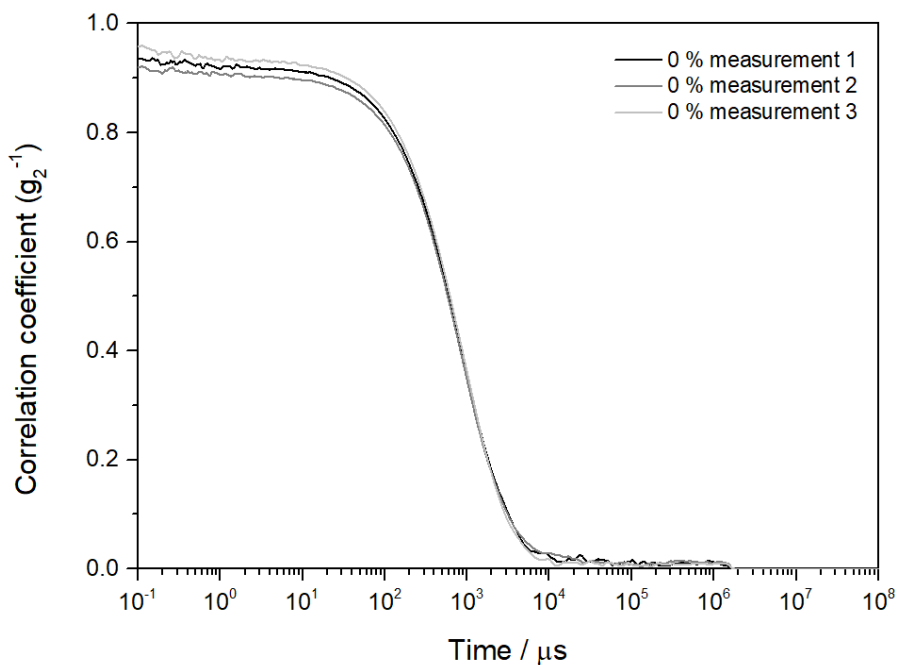


Figure S84: Correlograms of dispersions in water of 0% samples.

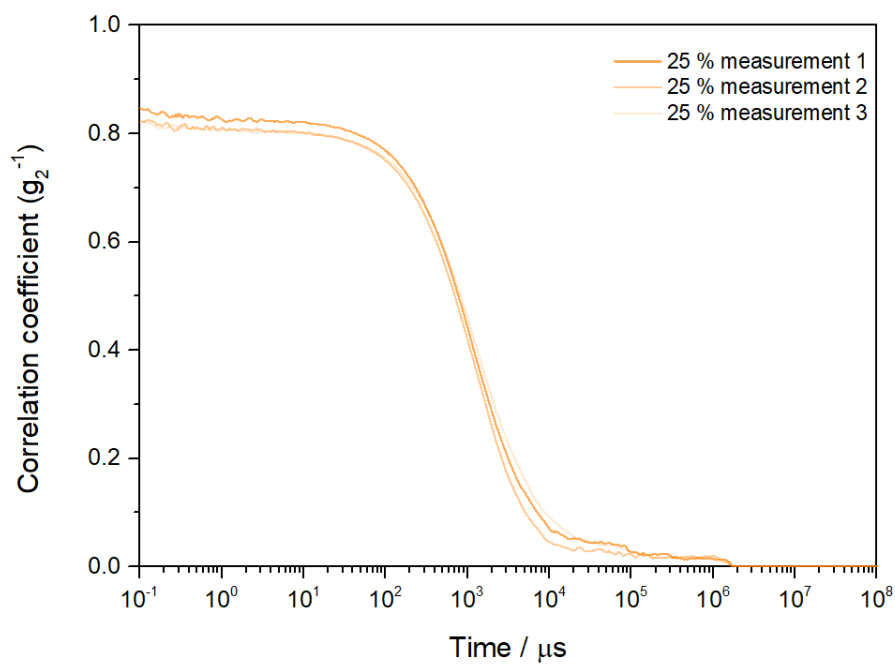


Figure S85: Correlograms of dispersions in water of 25% samples.

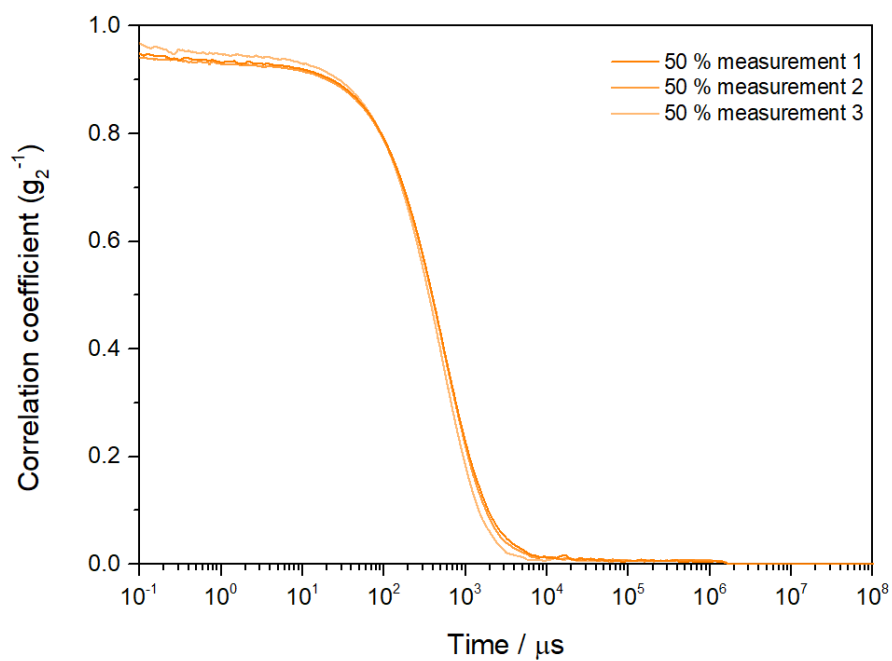


Figure S86: Correlograms of dispersions in water of 50% samples

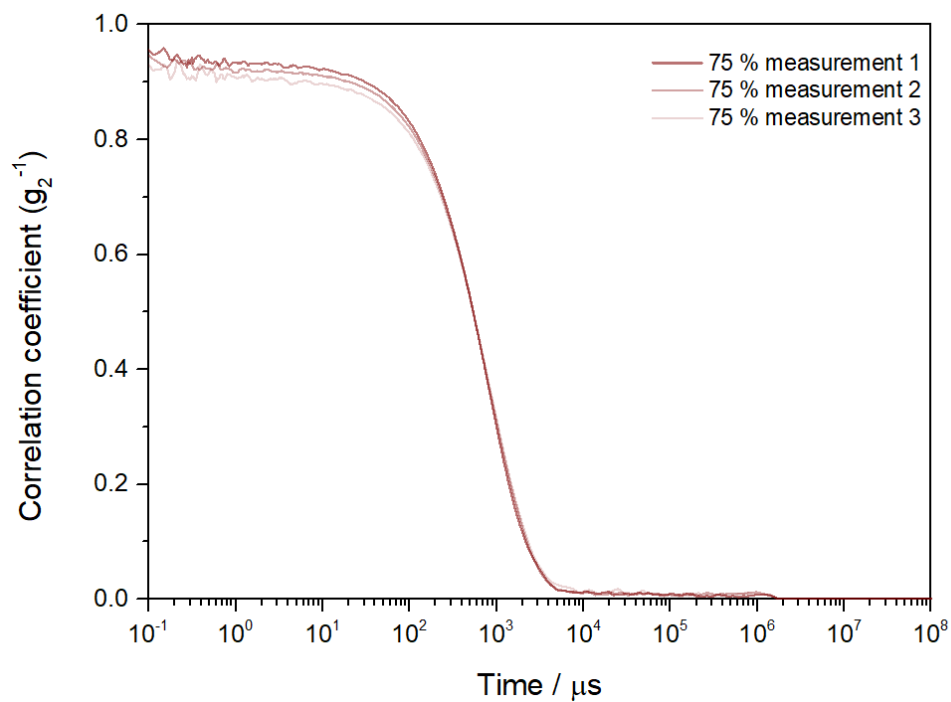


Figure S87: Correlograms of dispersions in water of 75% samples.

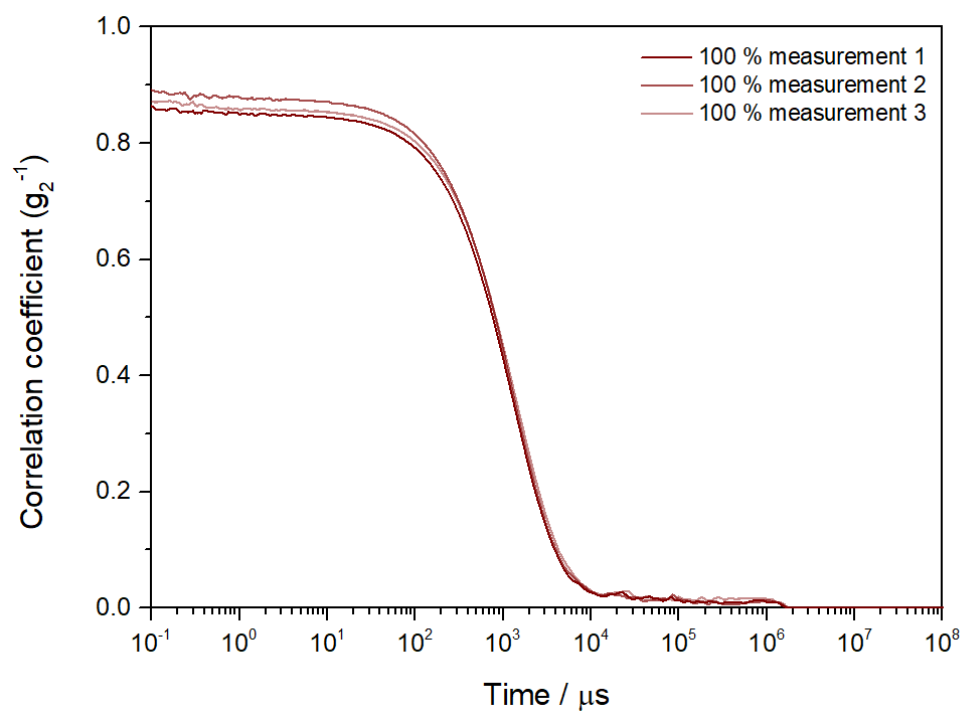


Figure S88: Correlograms of dispersions in water of 100% samples.

S.3.9 Lattice Strain

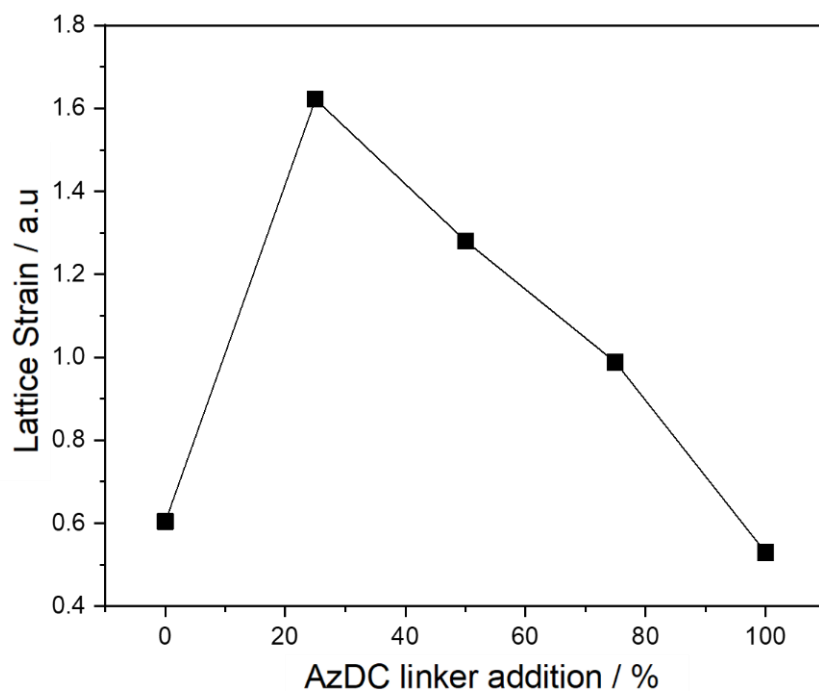


Figure S89: Lattice Strain as a function of the % of linker added.

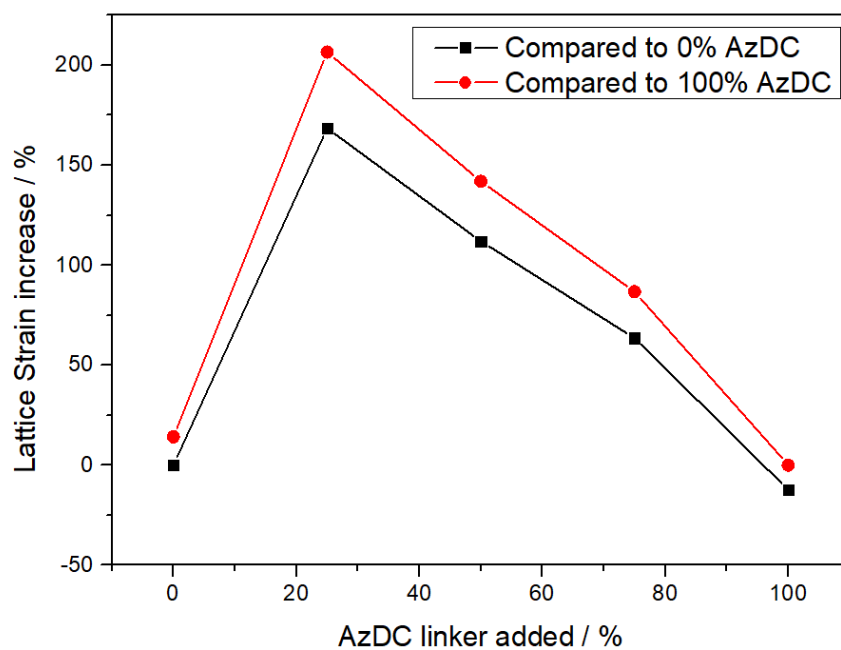


Figure S90: Percentage of lattice Strain increase as a function of the % of linker added.

S.3.10 Vibrational spectroscopy

S3.10a. Fourier transformed Infra-Red (FT-IR)

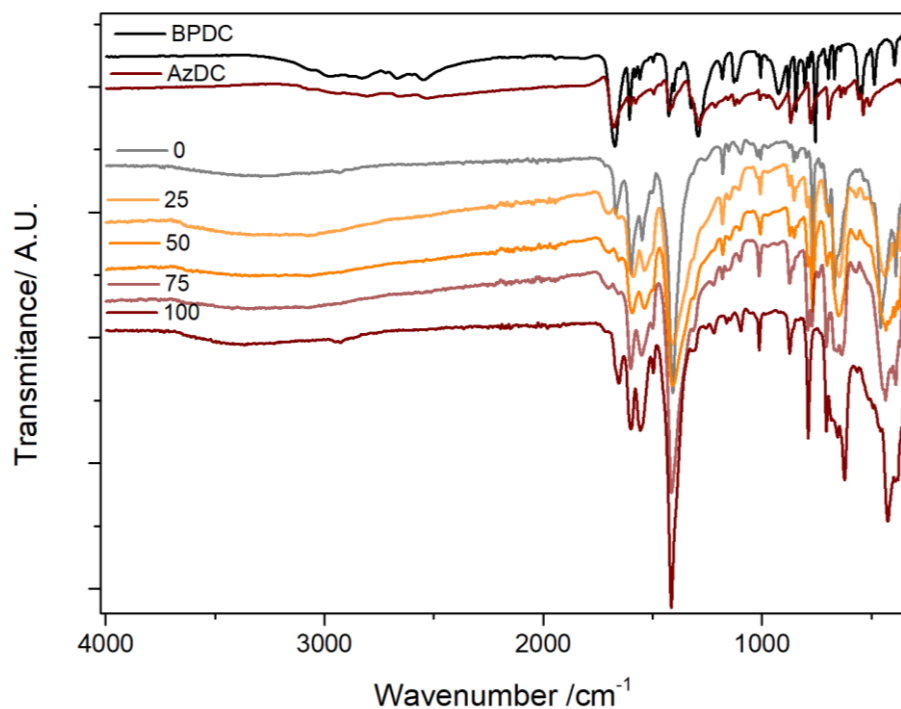


Figure S91: Raw FT-IR profiles of MTV MOFs compared to pristine single-linker MOFs and their respective ligands.

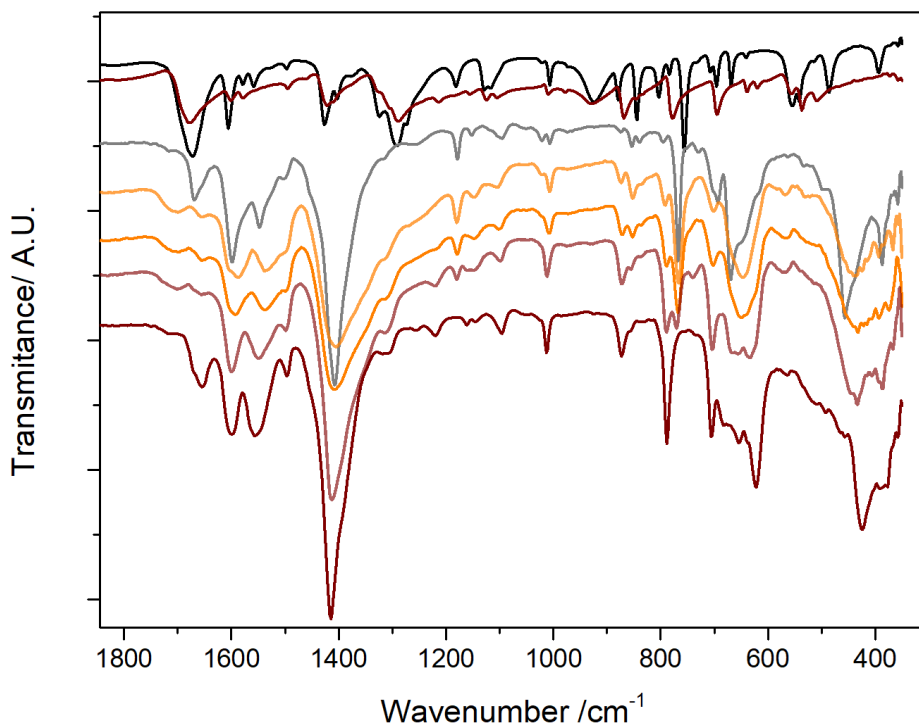


Figure S92: Amplification of FT-IR profiles of MTV MOFs compared to pristine single-linker MOFs and their respective ligands. showing incorporation due to the absence of free carboxylate signals. Legends from Figure S91 apply.

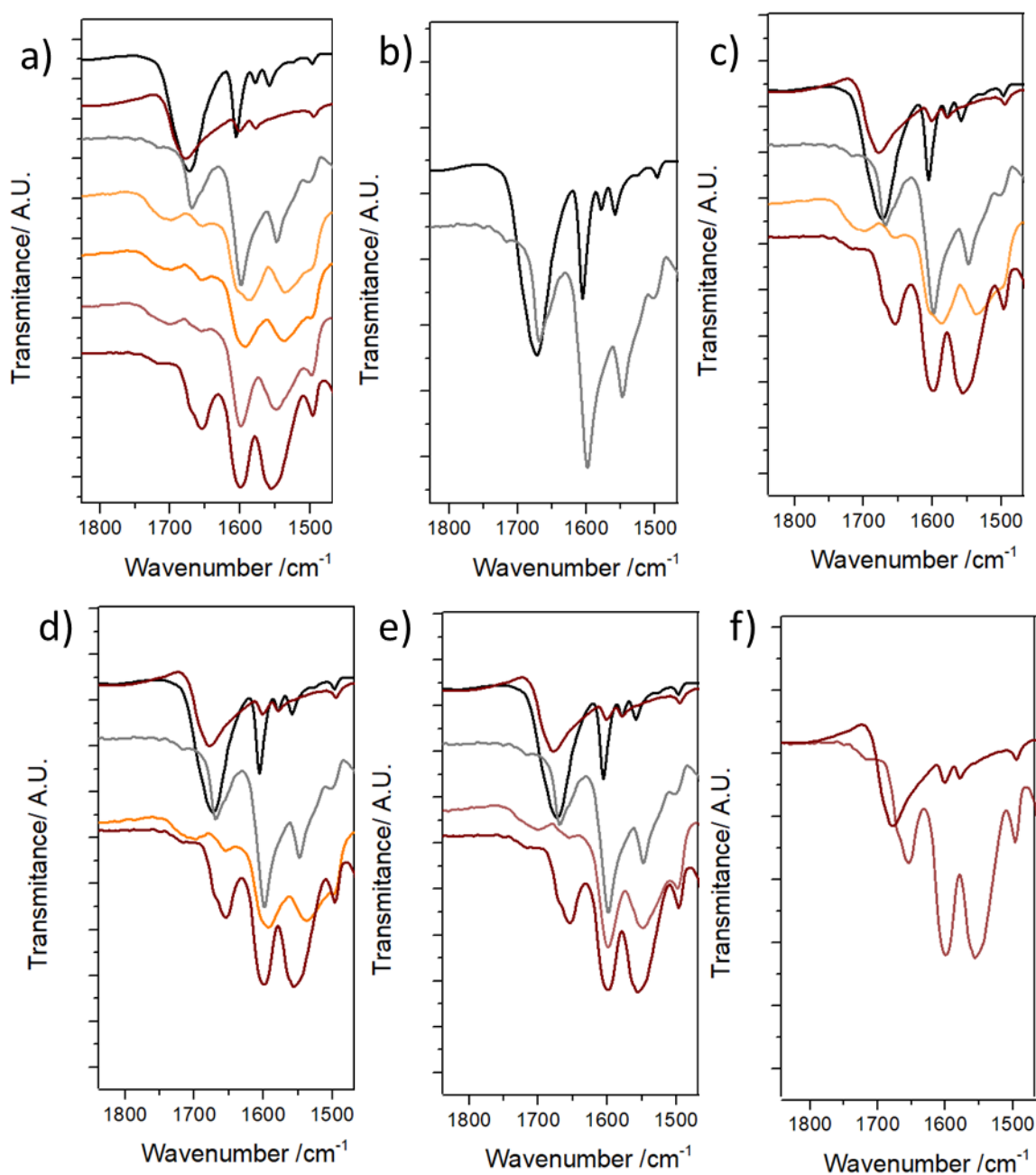


Figure S93: Amplification of FT-IR profiles of MTV MOFs compared to pristine single-linker MOFs and their respective ligands, in the carboxylate vibration region. Legends from Figure S91 apply. A) all the materials, b) 0% and its ligand, c) 25% and its ligands, d) 50% and its ligands, e) 75% and its ligands and f) 100% and its ligand. The appearance of new carboxylate signals that do not correspond to free linker or bond Zr-carboxylate suggests the presence of dangling linkers,

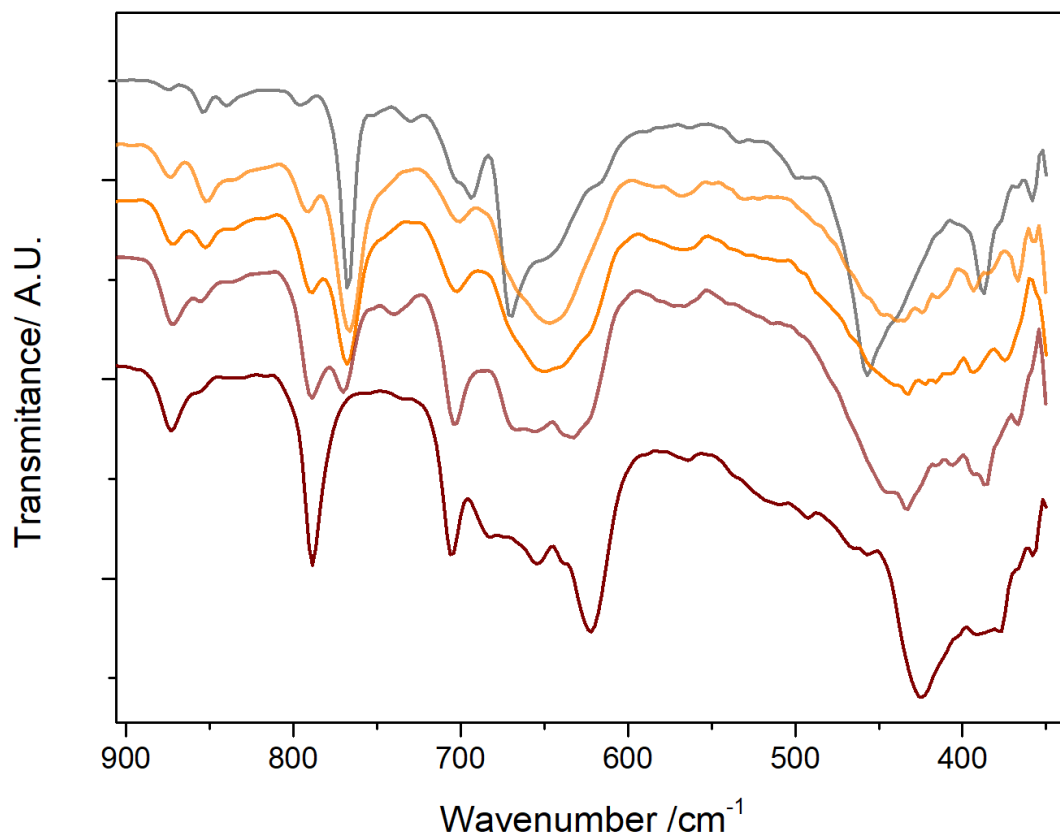


Figure S94: Amplification of FT-IR profiles of MTV MOFs compared to pristine single-linker MOFs and their respective ligands, showing structural distortion in the Zr_6 clusters. Legends from Figure S91 apply.

Table S12: Bond lengths extracted from calculated structures.

Atom 1	Atom 2	0% AzDC	25% AzDC	50% AzDC	75% AzDC	100% AzDC
Zr	Zr	3.4888	3.4154	3.4500	3.4306	3.4864
Zr	Zr	3.4914	3.3355	3.3954	3.4077	3.4684
Zr	Zr	3.4809	3.3591	3.4442	3.4679	3.4769
Zr	Zr	3.4880	3.3498	3.4305	3.4507	3.4709
Zr	O	2.1313	2.1285	2.1153	2.1201	2.1208
Zr	O	2.1284	2.1273	2.1204	2.1308	2.1194
Zr	O	2.1320	2.1382	2.1222	2.1251	2.1383
Zr	O	2.1320	2.1263	2.1208	2.1273	2.1338
Zr	O	2.2652	2.2527	2.3045	2.3571	2.2491
Zr	O	2.2682	2.3251	2.3759	2.5352	2.3019
Zr	O	2.2703	2.1688	2.1823	2.1830	2.2750
Zr	O	2.2673	2.1898	2.1896	2.1859	2.3037
Average distance Zr-Zr		3.4873	3.3650	3.4300	3.4392	3.4757
Average distance Zr-o		2.1993	2.1821	2.1914	2.2206	2.2053

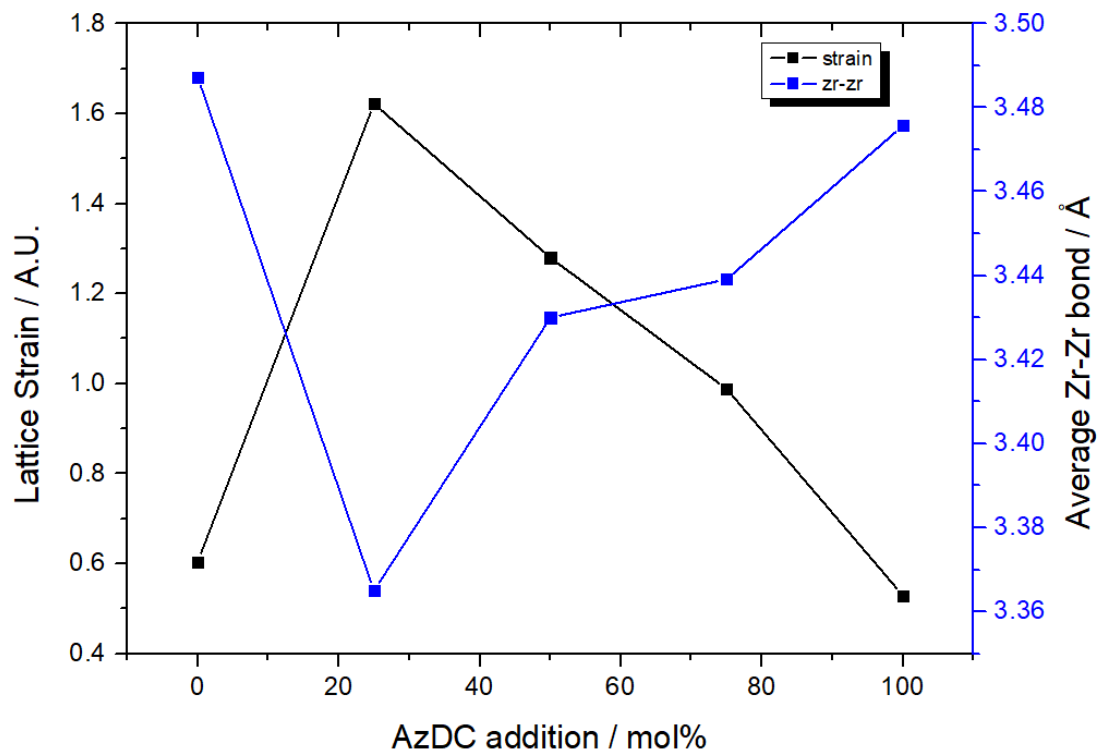


Figure S95: Lattice Strain and average Zr-Zr bond as a function of the % of linker added.

S3.10b. Raman

For the sample containing only the BPDC linker, vibrations associated with its functional groups can be observed, highlighting the vibrations of aromatic rings and carboxylate groups.^[10] The most intense modes are located at 1292 and 1612 cm^{-1} , corresponding to C–C inter-ring stretch and C=C aromatic stretch, respectively. Carboxylate-related bands are also observed, the C–O symmetric stretching at 1440 cm^{-1} , the C–O asymmetric stretching at 1524 cm^{-1} . The band at 440 cm^{-1} is ascribed to the asymmetric stretching of the μ_3 -OH groups (out of phase). As the AzDC linker is gradually introduced, there is a reversal in the intensity of the signals at ca. 1292 and 1612 cm^{-1} and a gradual emergence of peaks related to the 100% AzDC MOF, located at 1404, 1459, and 1497 cm^{-1} . In the literature, these signals are attributed to both C–N inter-ring and *trans* N=N group vibrations, as well as O–C–O vibrations.^[10–12] Additionally, there is a notable increase in the intensity of modes at 1134 and 1181 cm^{-1} . The band at ca. 1134 cm^{-1} is also attributed to C–N stretch in *cis* azobenzene, and C–C aromatic ring breathing. Thus, the masking of signals does not allow for unequivocally assignment.

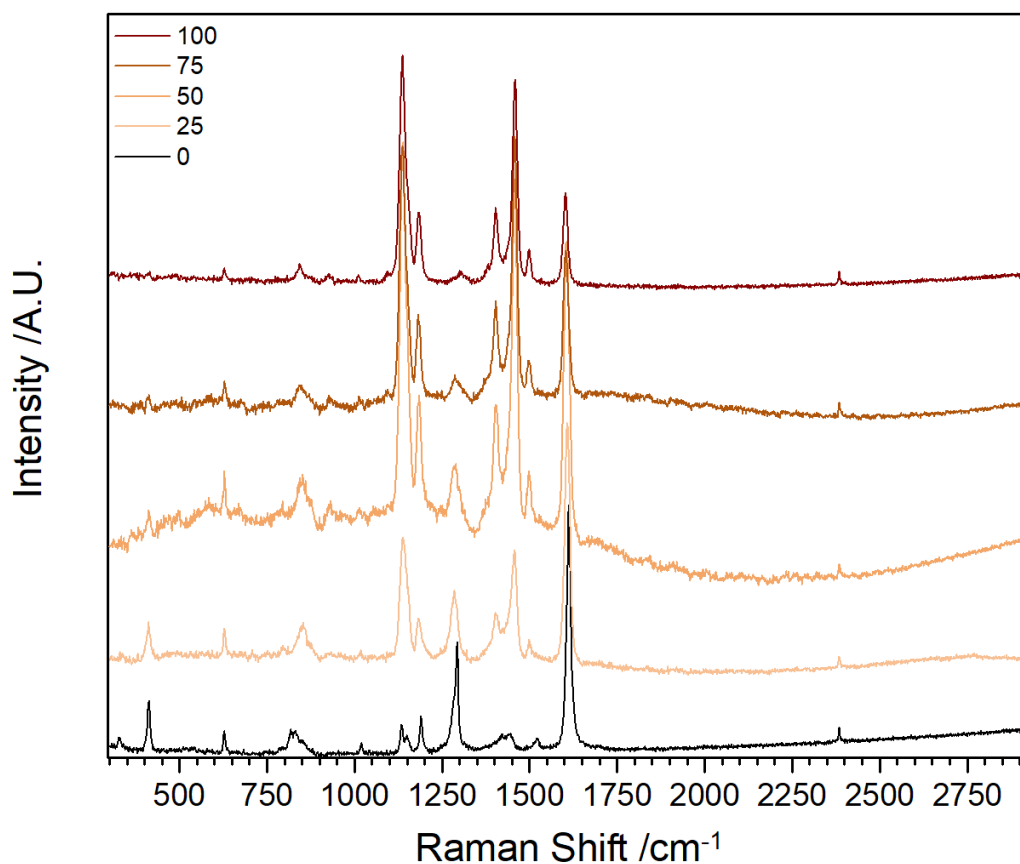


Figure S96: Raman spectra of the MOFs.

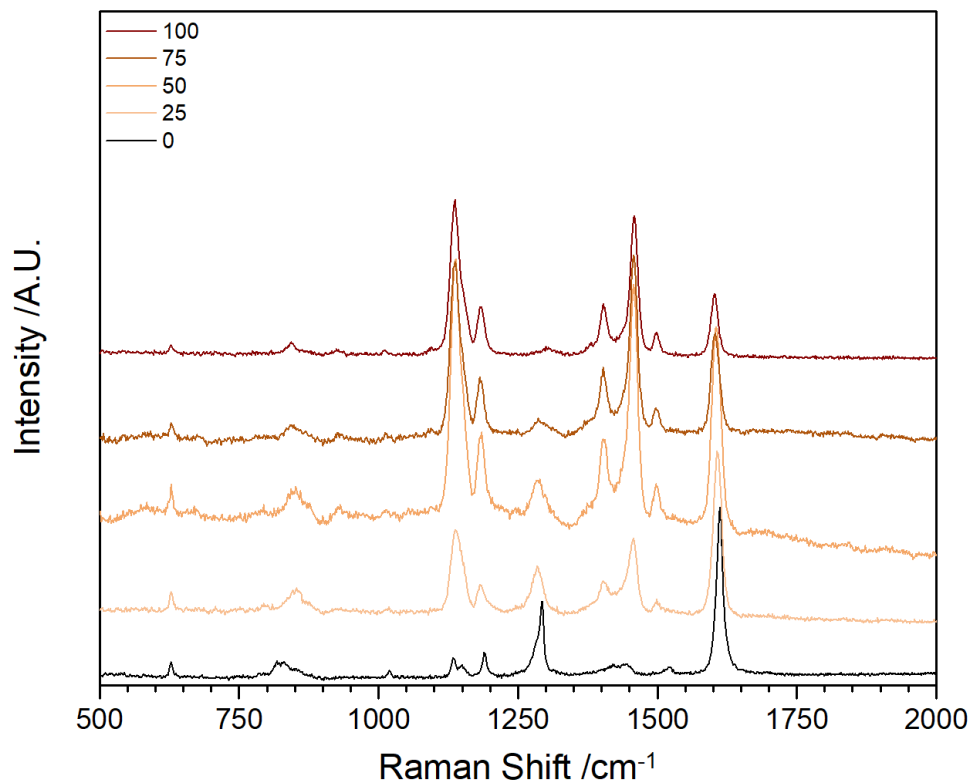


Figure S97: Amplification of the Raman spectra of the MOFs.

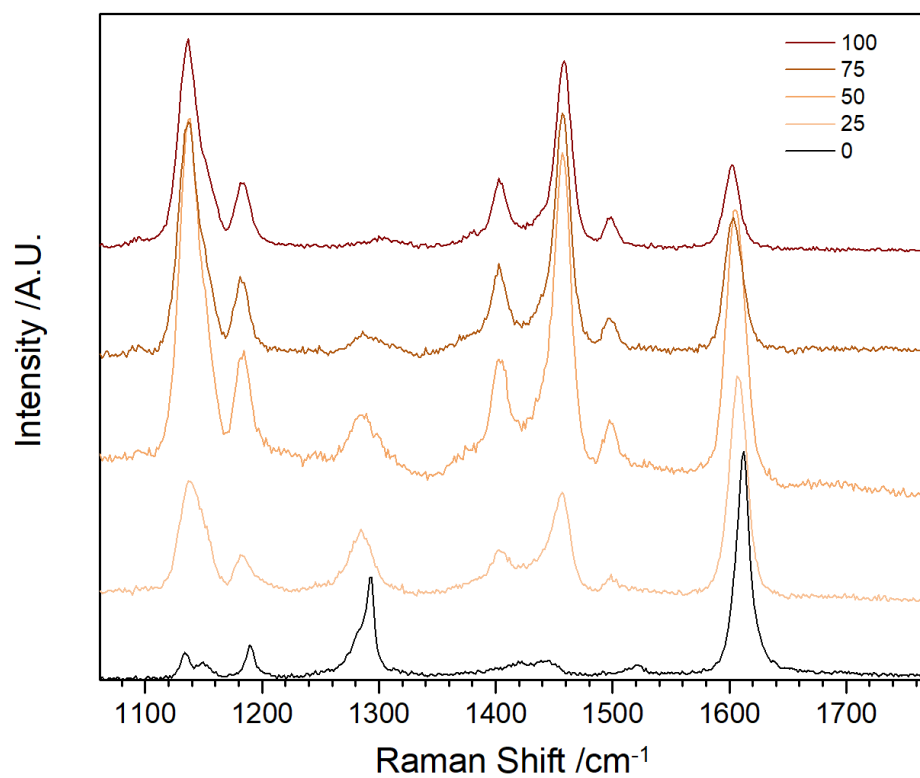


Figure S98: Amplification of the Raman spectra of the MOFs.

S.3.11 Solid-state UV-Vis

S.3.11a Dark conditions

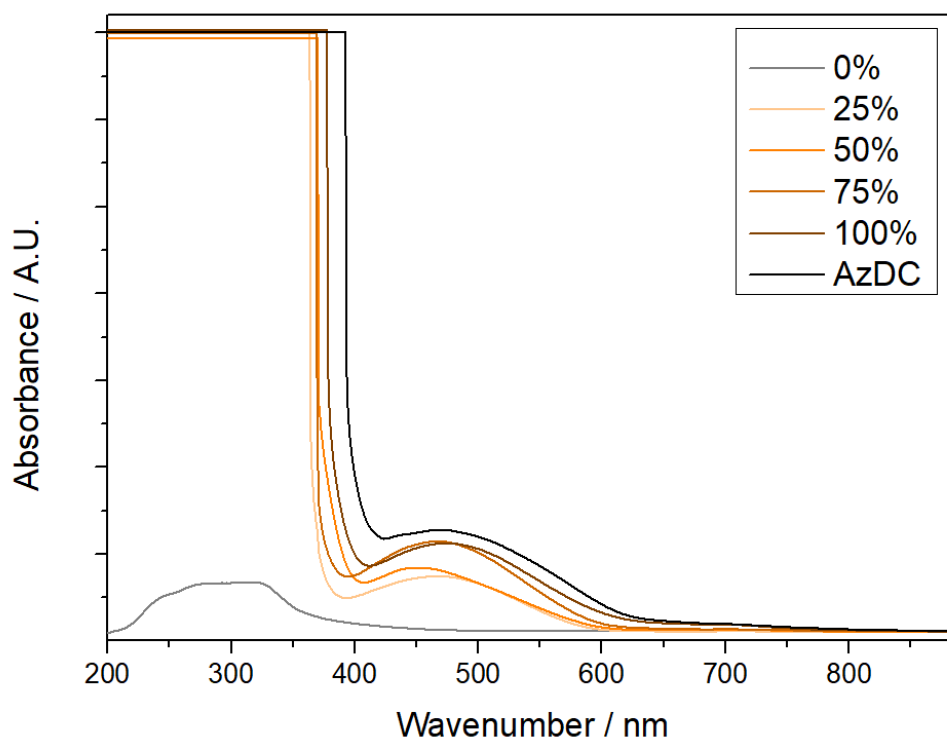


Figure S99: Solid state UV-Vis spectra of the samples.

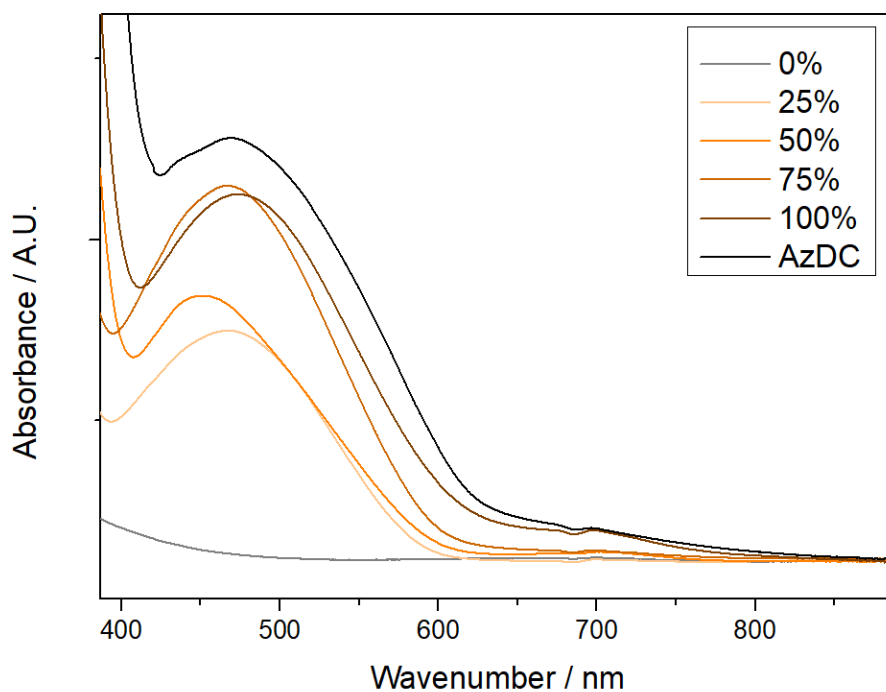


Figure S100: Amplification of the solid-state UV/Vis spectra to the samples.

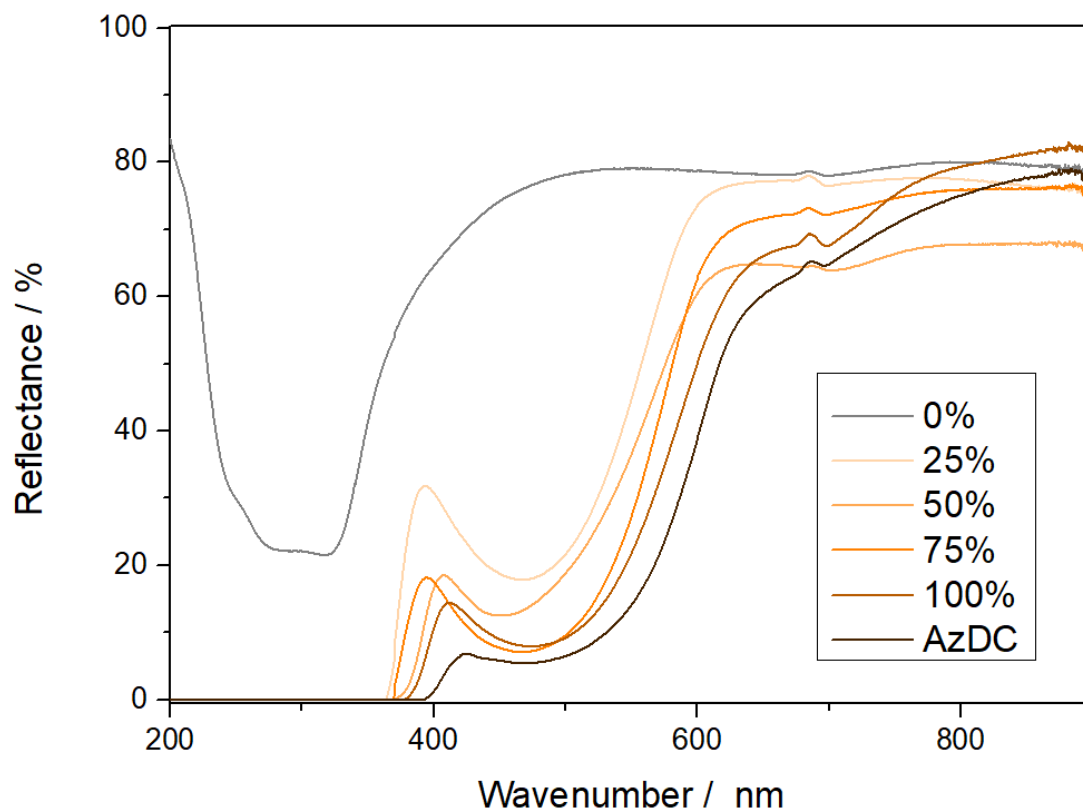


Figure S101: Diffuse reflectance UV-Vis spectra of the samples.

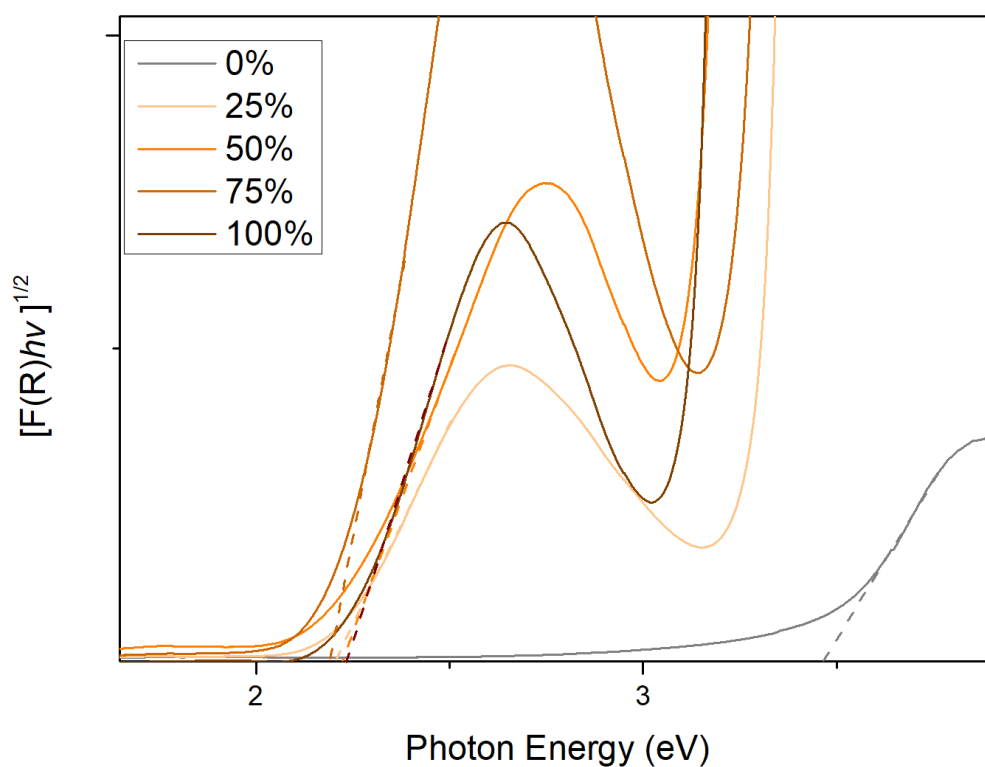


Figure S102: Tauc plot of the samples to extract the band gap.

S.3.11b Electronic structure calculations

For electronic structure calculations, we sampled the unit cell in the Γ -point approximation with a sufficiently large supercell.

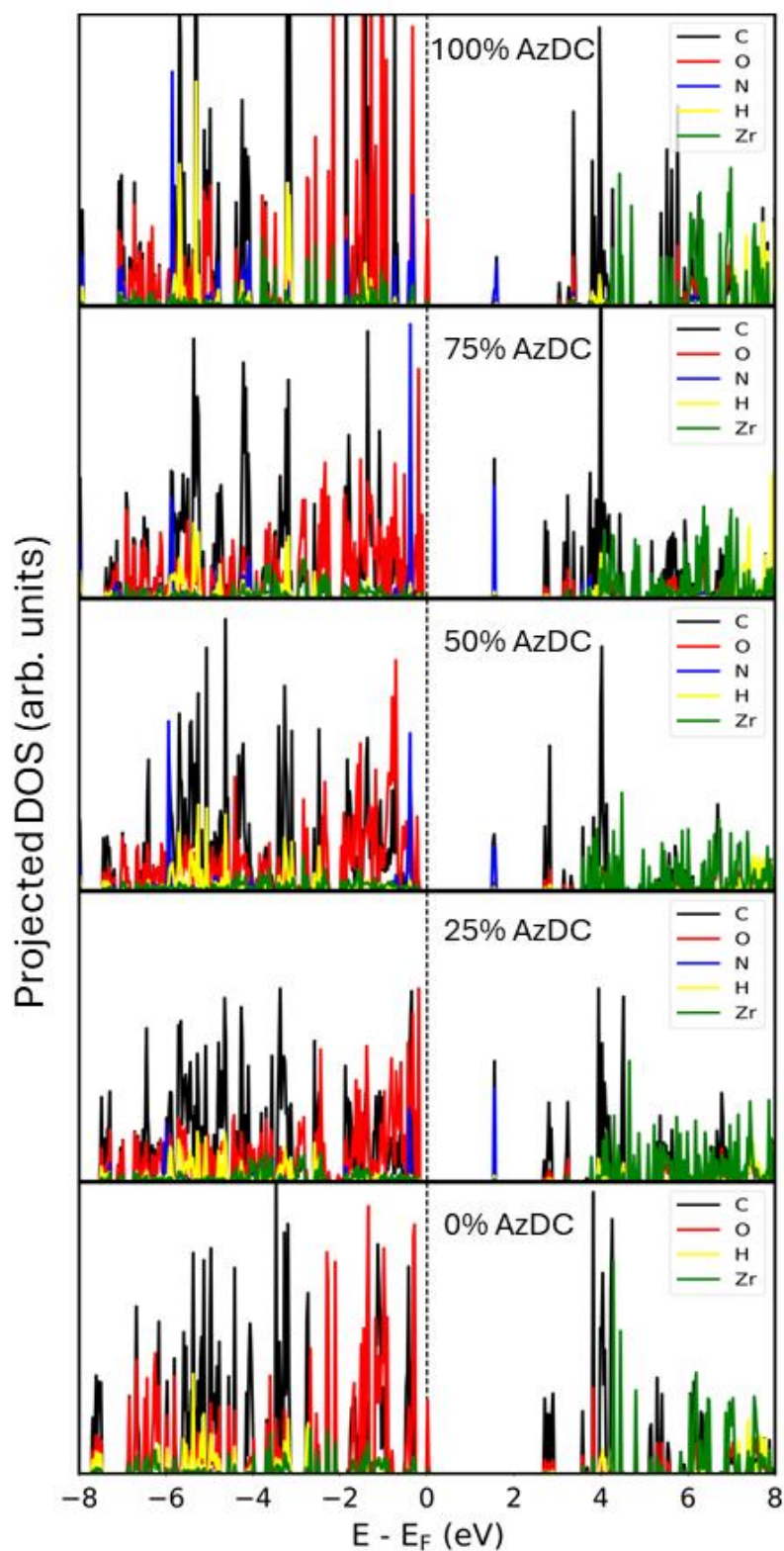


Figure S103: Projected density of states of the MTV series, showing that the decrease in band gap upon the introduction of AzDC is due to the azo group.

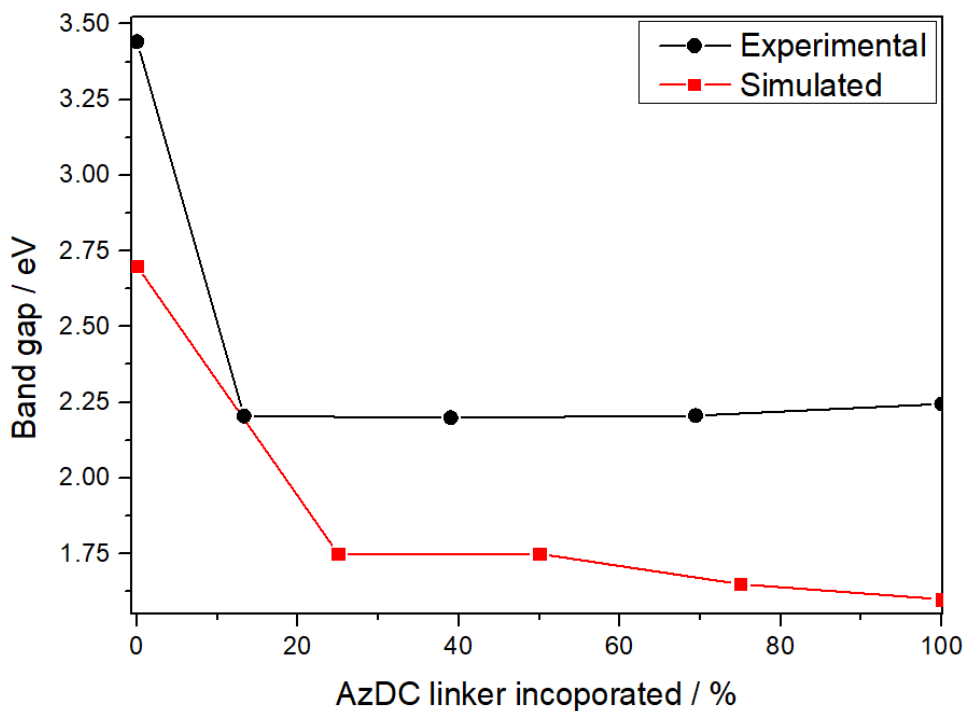


Figure S104: Comparison of band gap values of the MTV series as a function of the molar% of AzDC in the structure for calculated and experimental structures, showing similar trends.

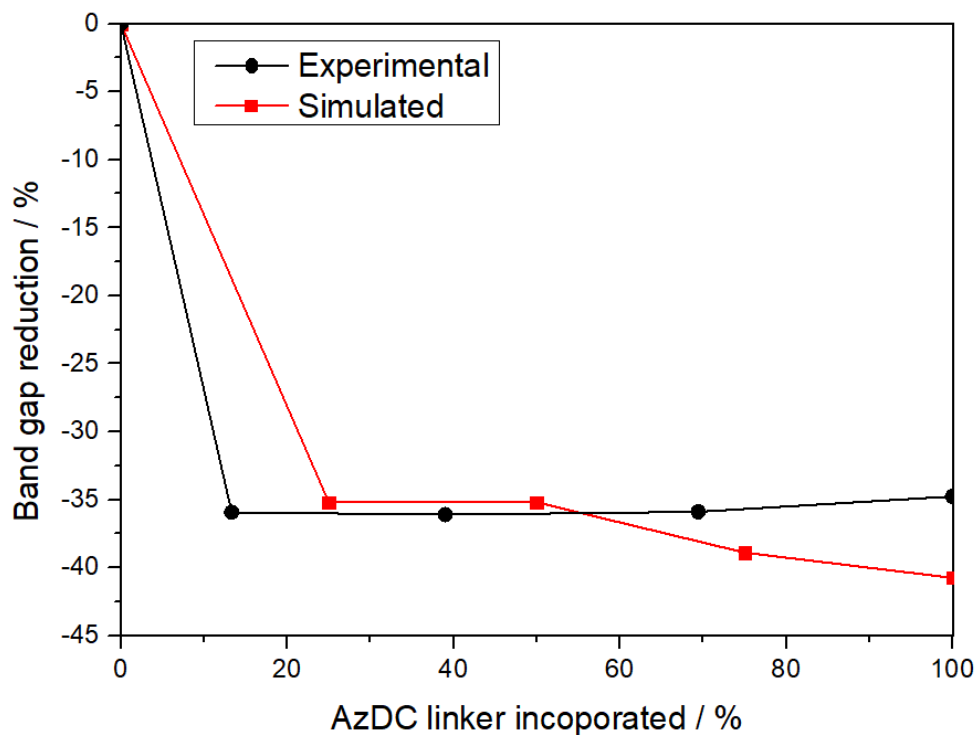


Figure S105: Comparison of the percentage of decrease in band gap values of the MTV series as a function of the molar% of AzDC in the structure for calculated and experimental structures, showing similar values.

S.3.11c After light irradiation

Light irradiation was performed with UV-c lamp for 60 minutes.

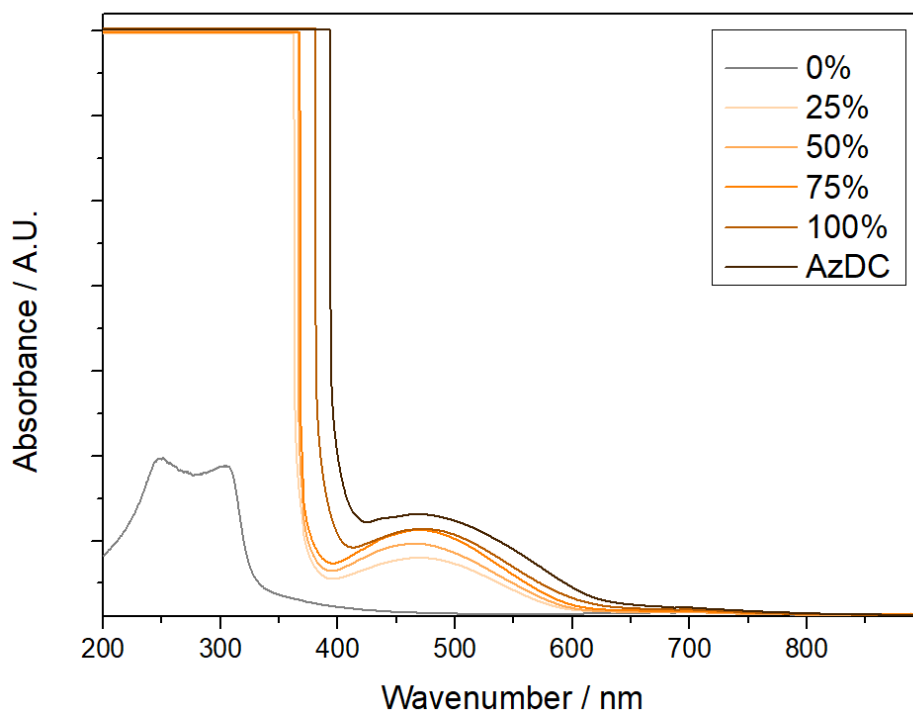


Figure S106: Solic state UV-Vis spectra of the samples, after 1 hour of light irradiation.

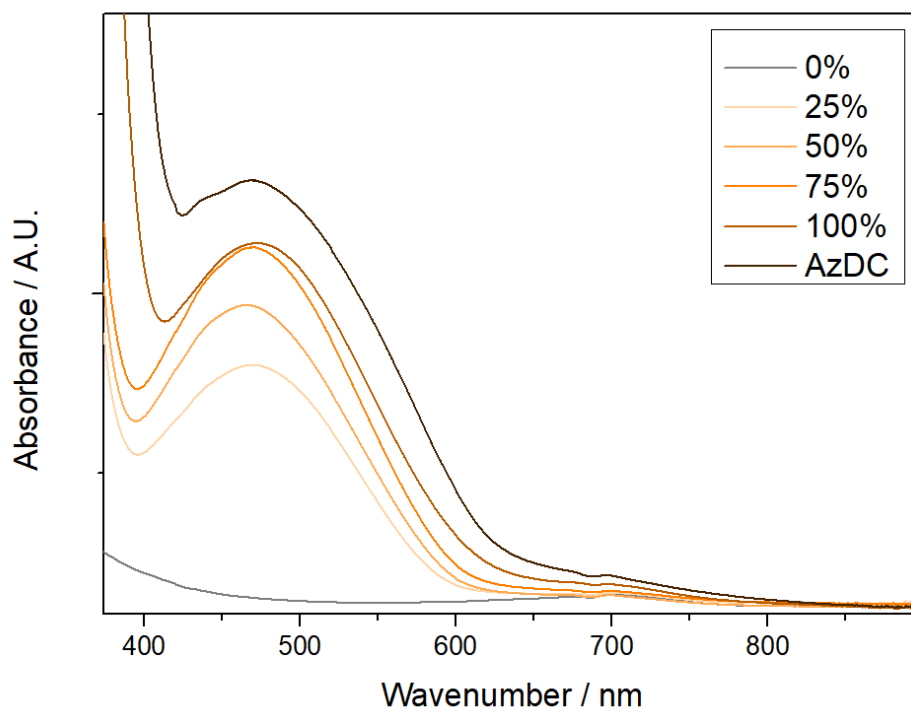


Figure S107: Solic state UV-Vis spectra of the samples, after 1 hour of light irradiation, showing a gradual increase in the intensity of the ca. 460 nm band with the incorporation of AzDC.

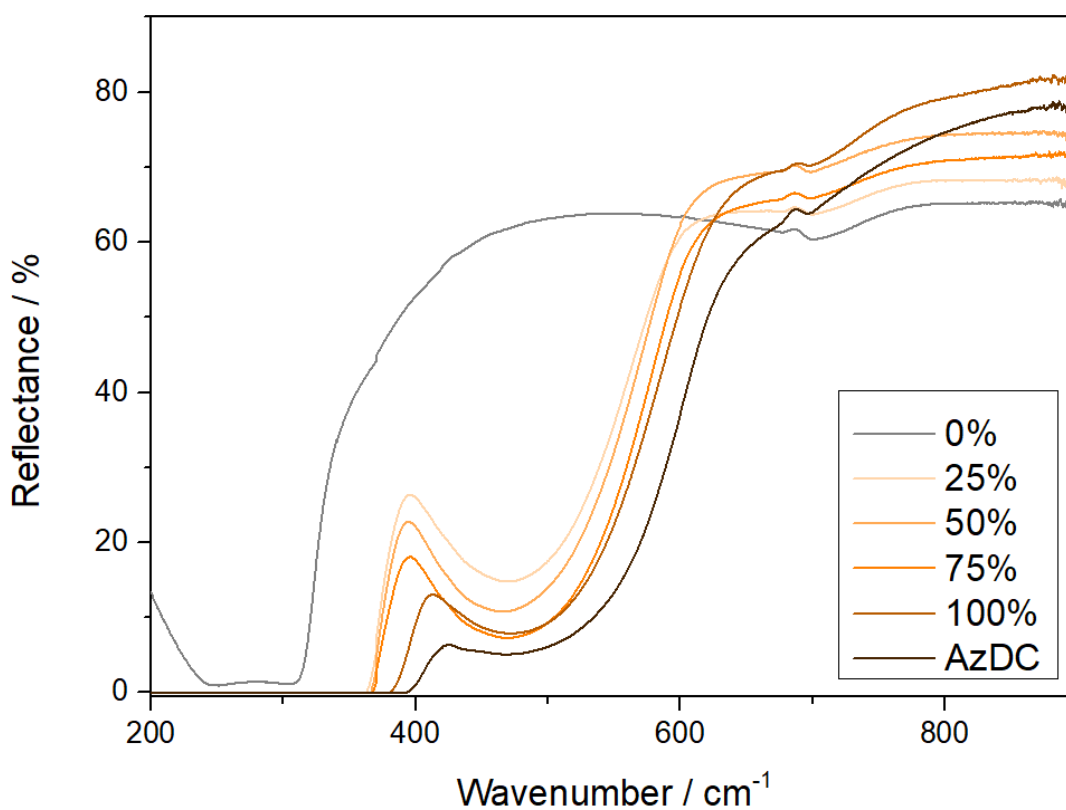


Figure S108: Diffuse reflectance UV-Vis spectra of the samples, after 1 hour under light.

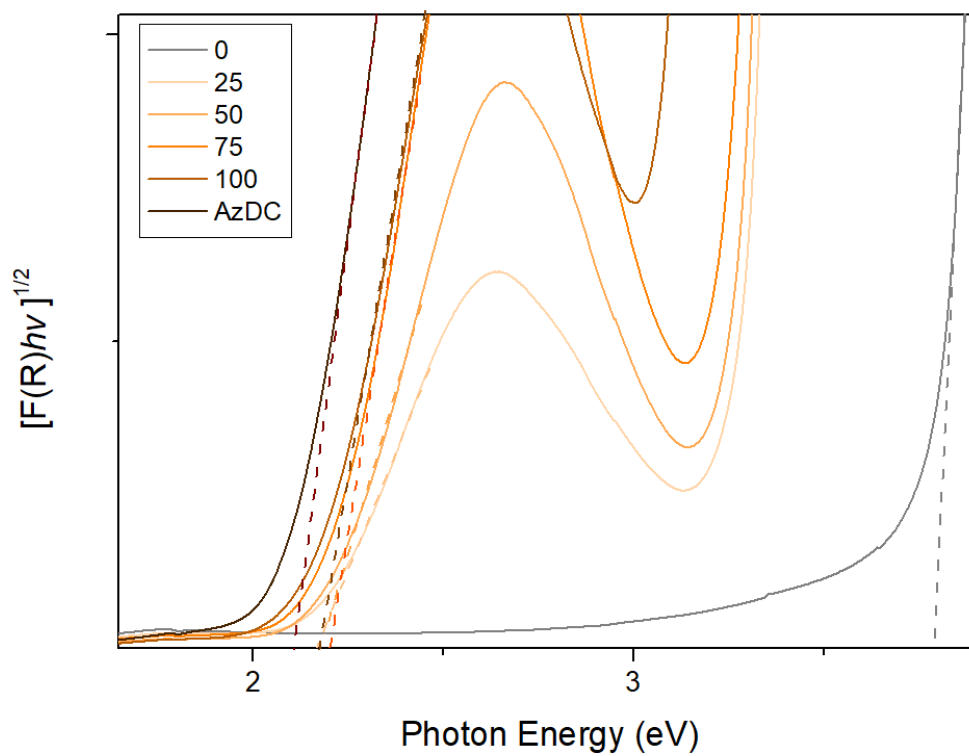


Figure S109: Tauc plot of the samples to extract the band gap, after 1 hour of light irradiation.

S.3.11d Band Gap (comparison before and after light irradiation)

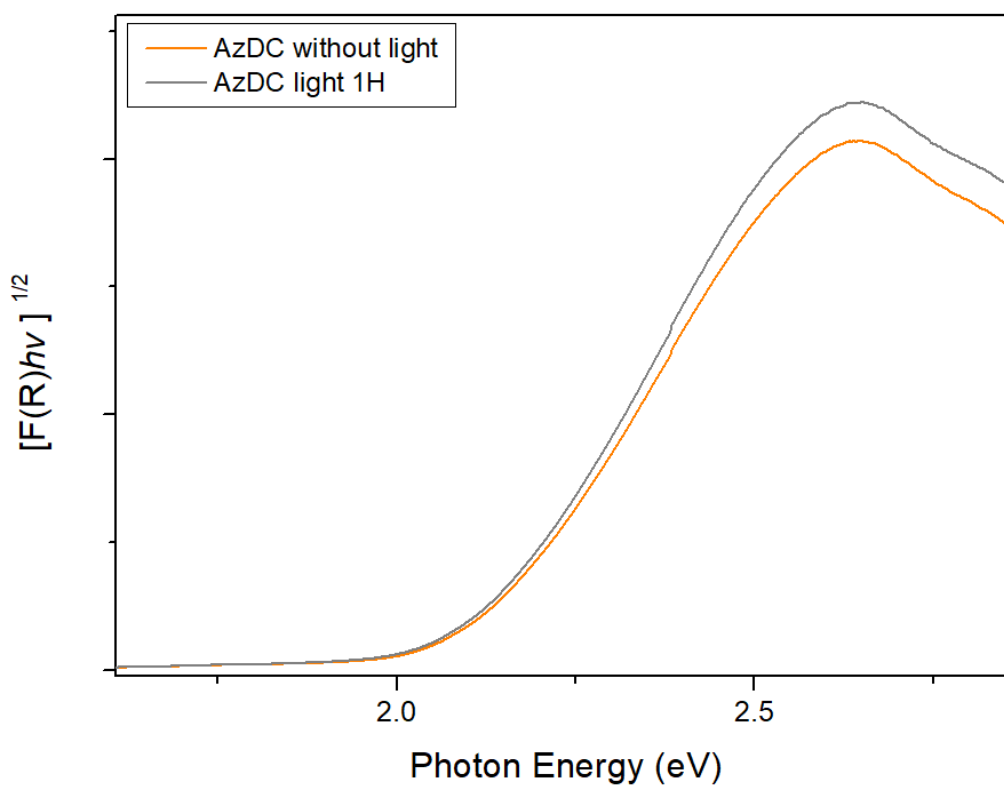


Figure S110: Tauc plot of the samples to extract the band gap, before and after 1 hour under light irradiation.

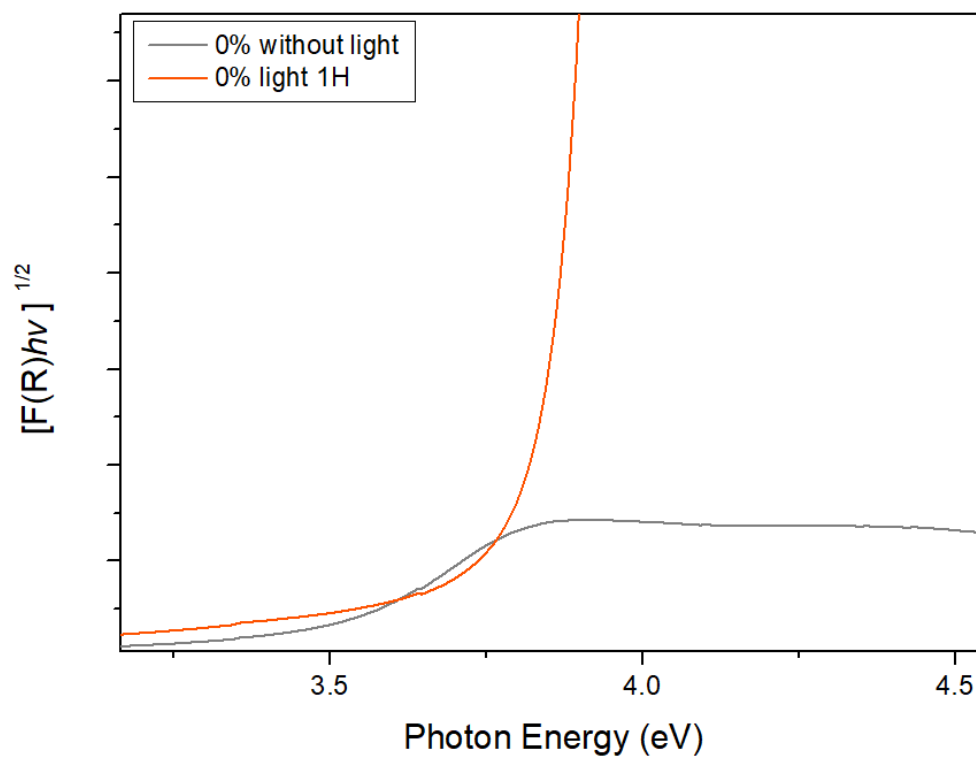


Figure S111: Tauc plot of the samples to extract the band gap, before and after 1 hour under light irradiation.

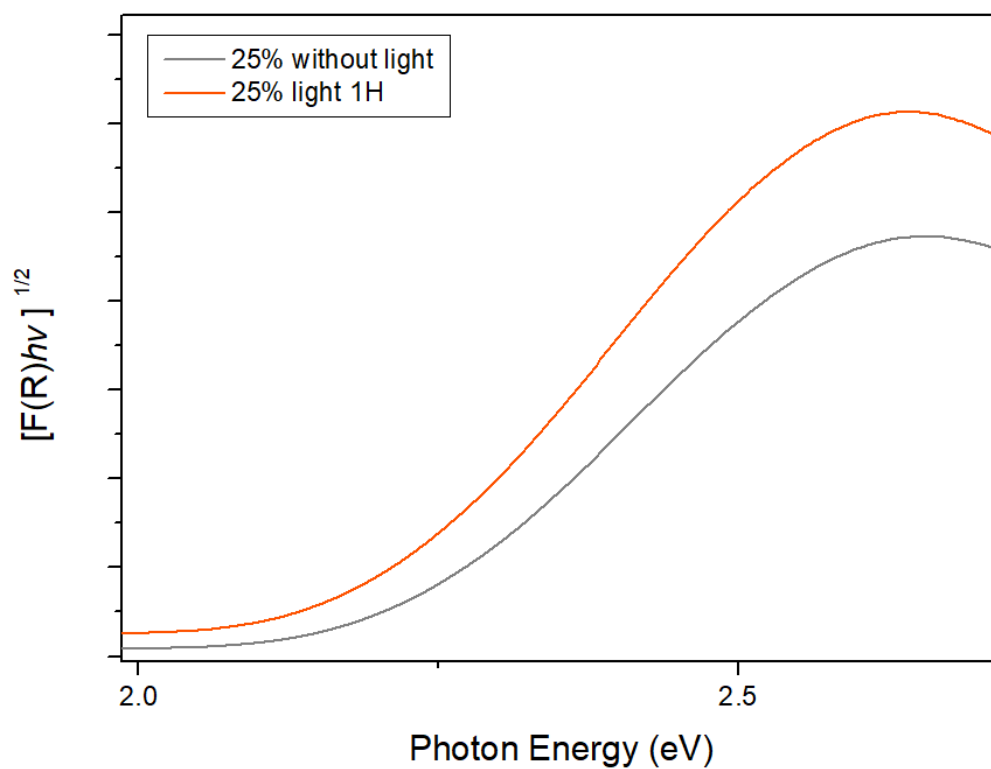


Figure S112: Tauc plot of the samples to extract the band gap, before and after 1 hour under light irradiation.

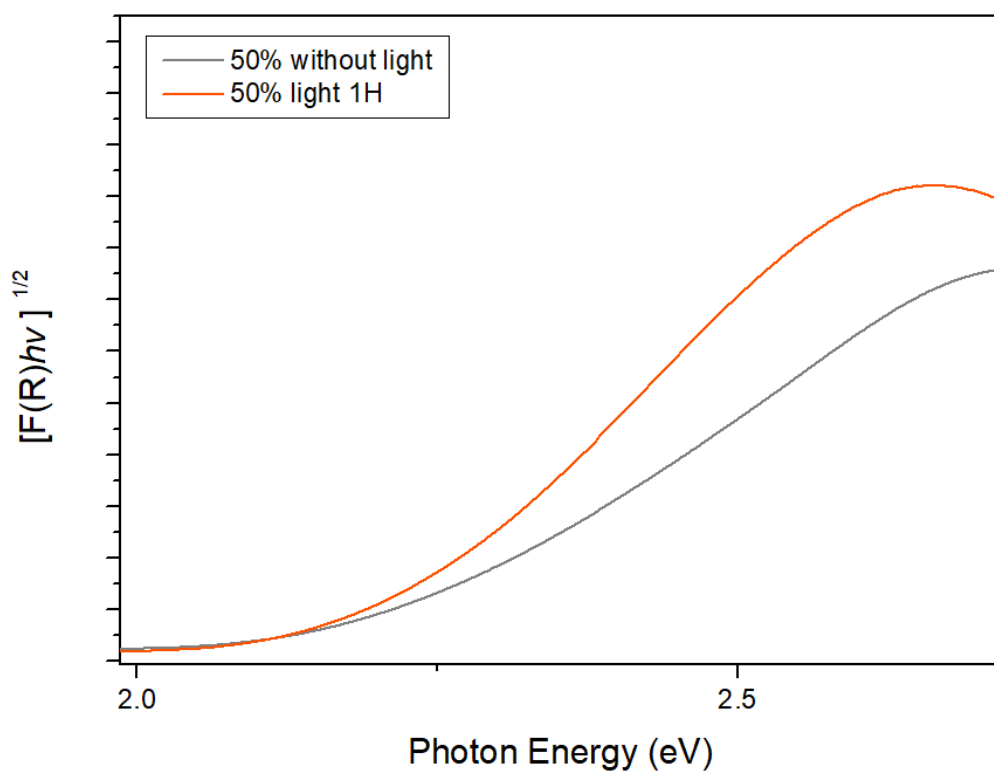


Figure S113: Tauc plot of the samples to extract the band gap, before and after 1 hour under light irradiation.

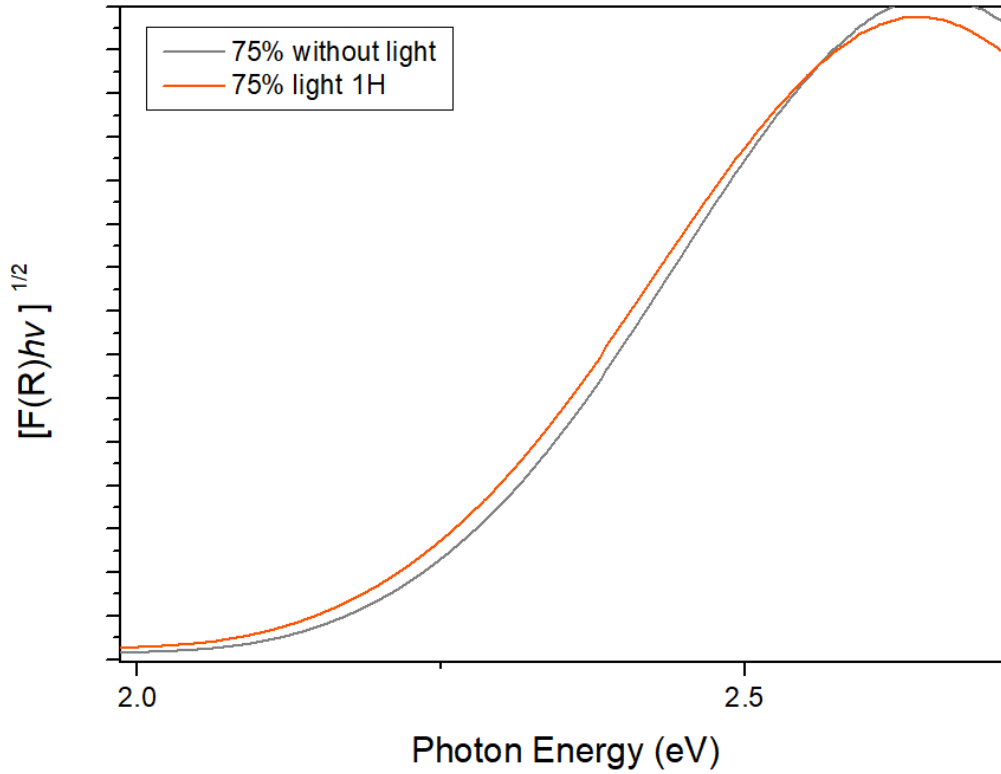


Figure S114: Tauc plot of the samples to extract the band gap, before and after 1 hour under light irradiation.

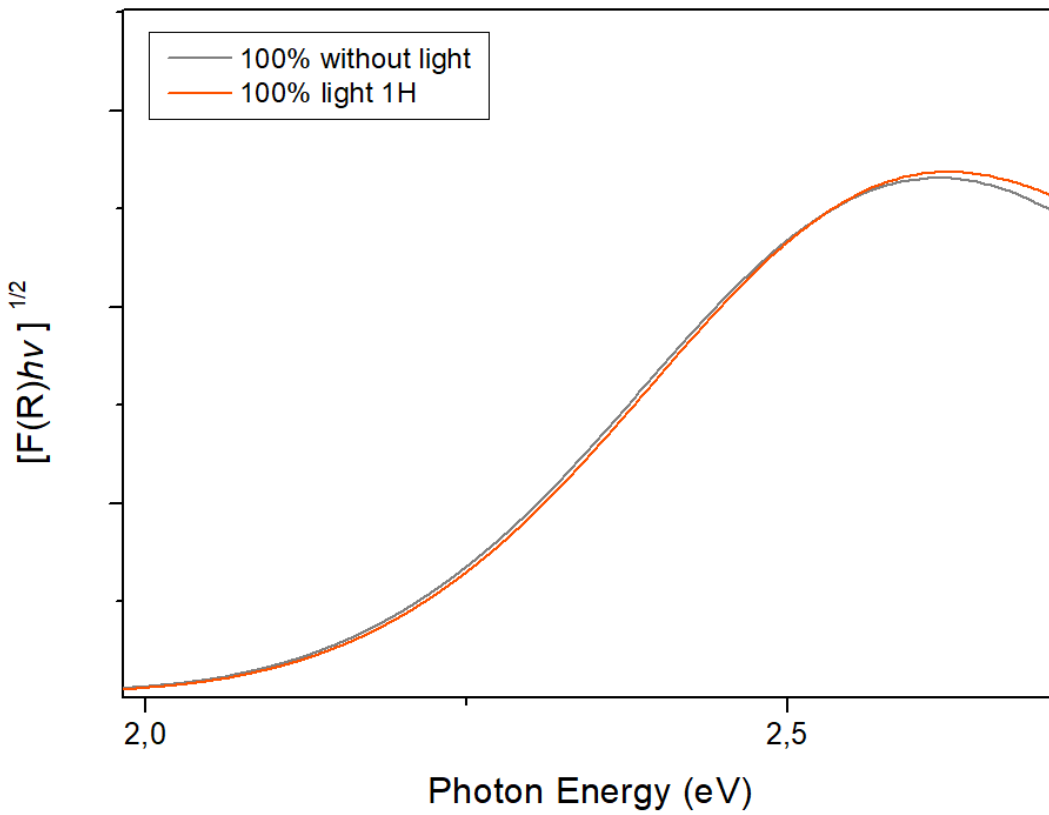


Figure S115: Tauc plot of the samples to extract the band gap, before and after 1 hour under light irradiation.

Table S13: Estimated band gap values.

Sample	Band Gap (eV)	Band Gap (eV) after light irradiation
Free AzDC	2.113	2.097
0%	3.441	3.896
25%	2.205	2.176
50%	2.199	2.170
75%	2.206	2.188
100%	2.174	2.181

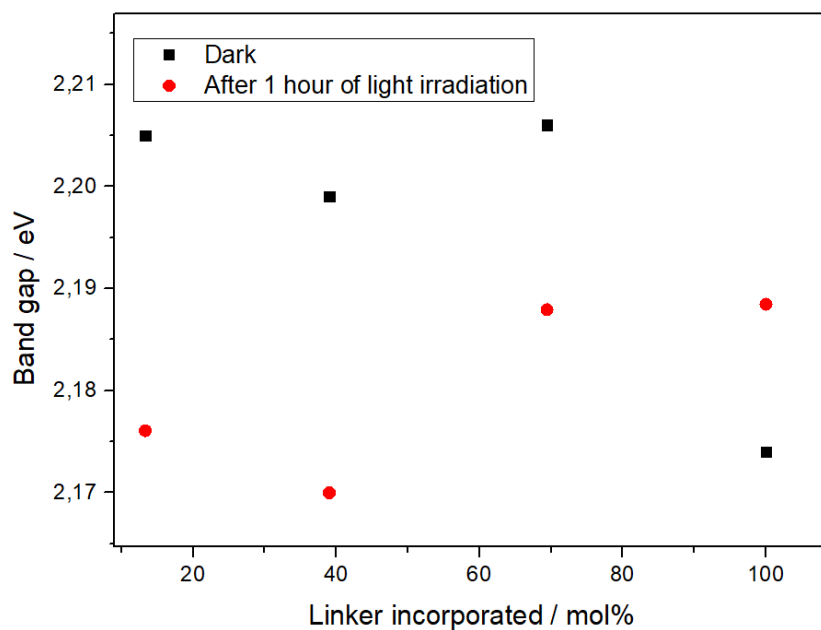


Figure S116: Optical band gap values as a function of the percentage of linker incorporated.

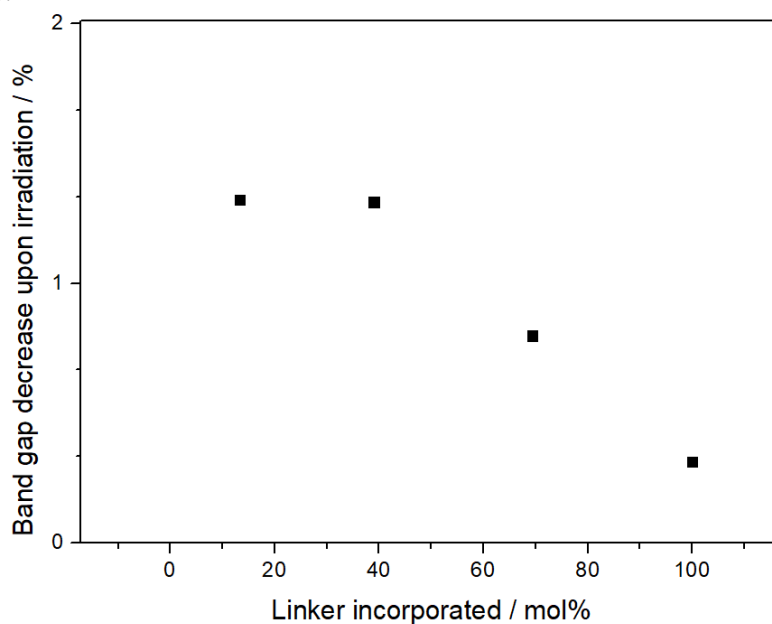


Figure S117: Decrease in optical band gap values upon light irradiation as a function of the percentage of linker incorporated.

S.3.11e UV-Vis in the dispersion

Unless otherwise stated, light irradiation was performed with UV-c lamp for 60 minutes.

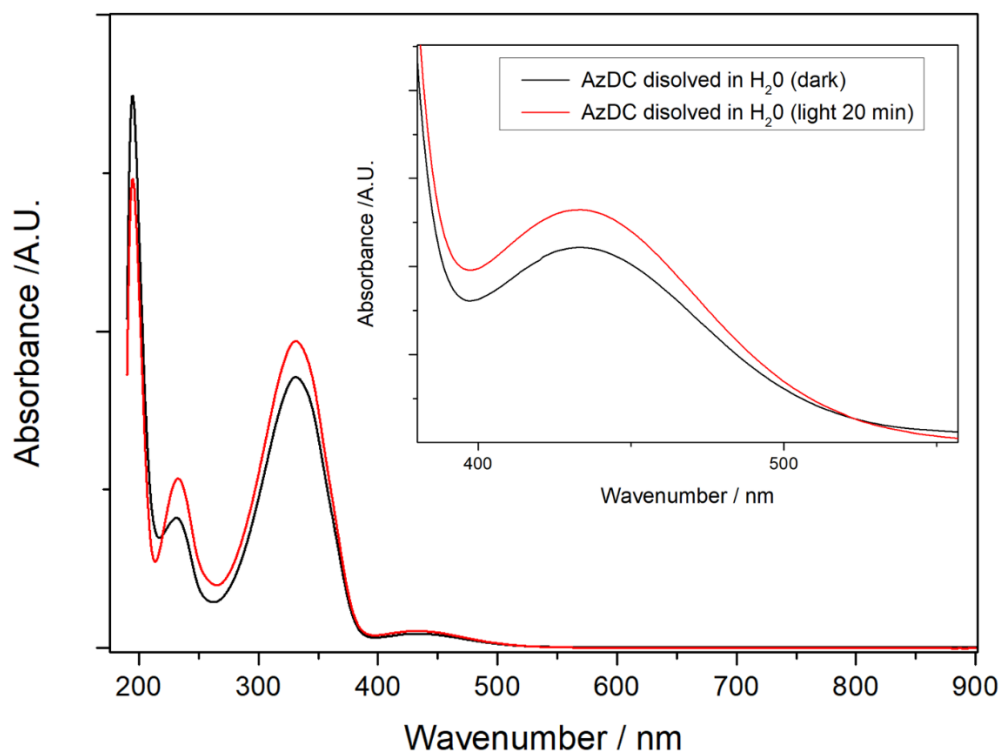


Figure S118: UV-Vis profile of AzDC dissolved in water, before and after light irradiation.

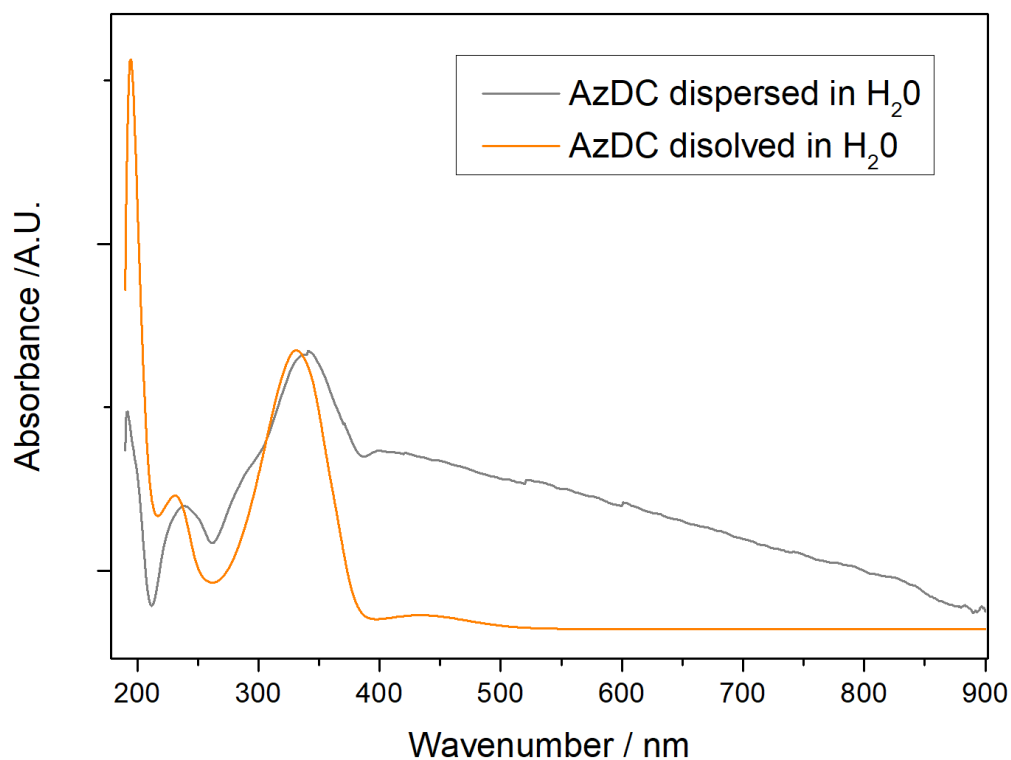


Figure S119: UV-Vis profile of AzDC dissolved and dispersed in water before light irradiation.

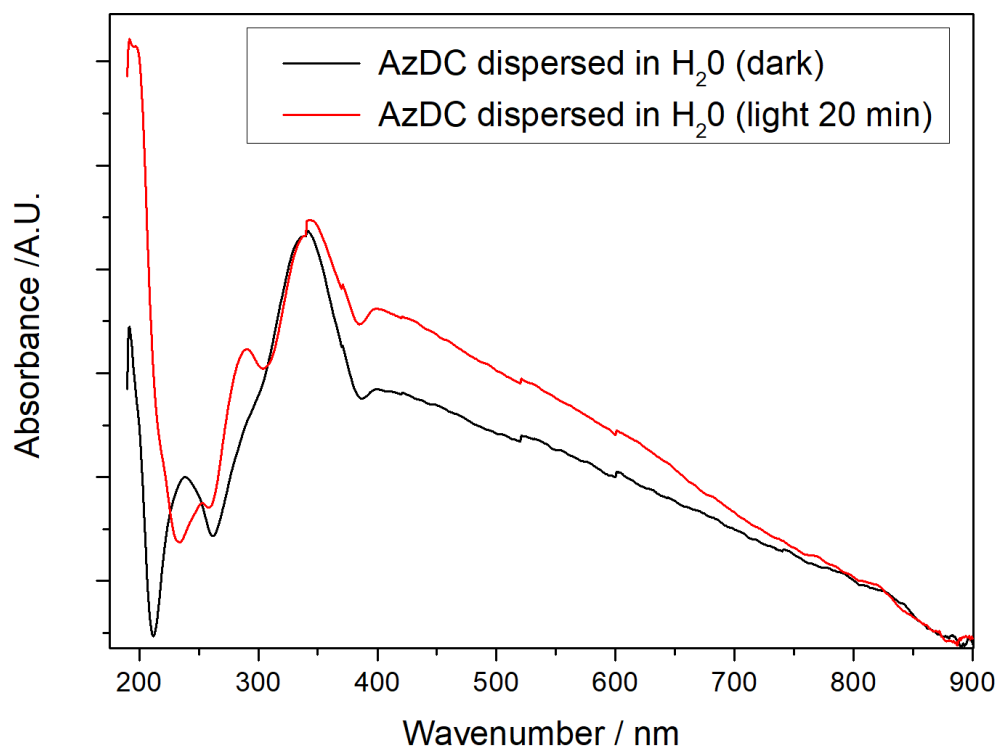


Figure S120: UV-Vis profile of AzDC dispersed in water, before and after light irradiation.

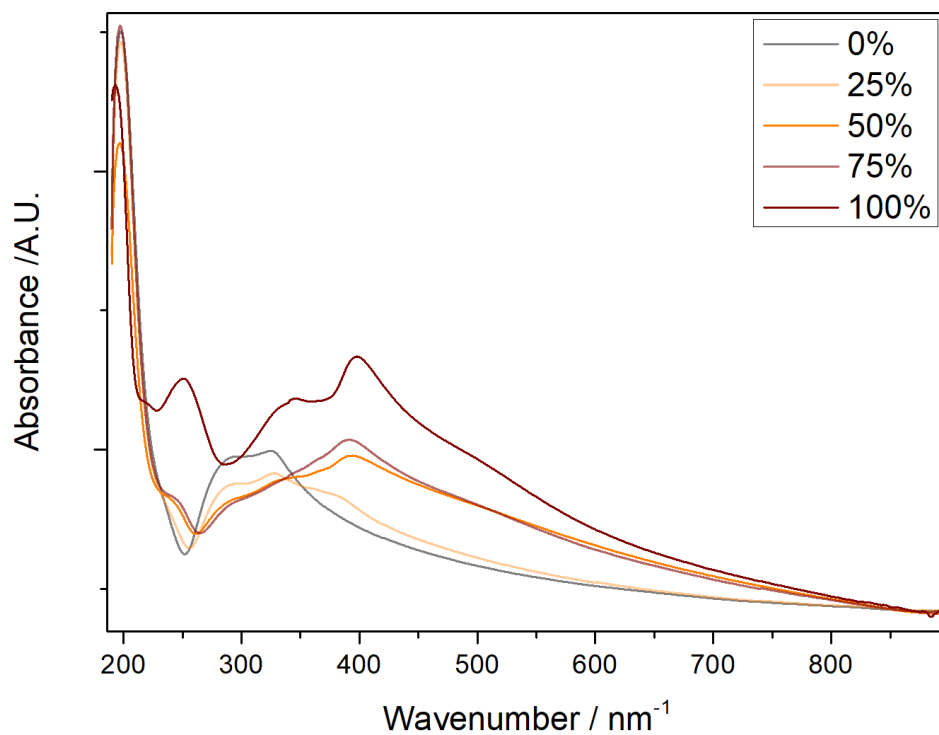


Figure S121: Raw UV-Vis profiles of MTVs MOF dispersed in H₂O without light irradiation, showing the presence of contributions from *cis* and *trans* AzDC conformations. The bands attributed to AzDC agree with the percentage of AzDC present in the samples.

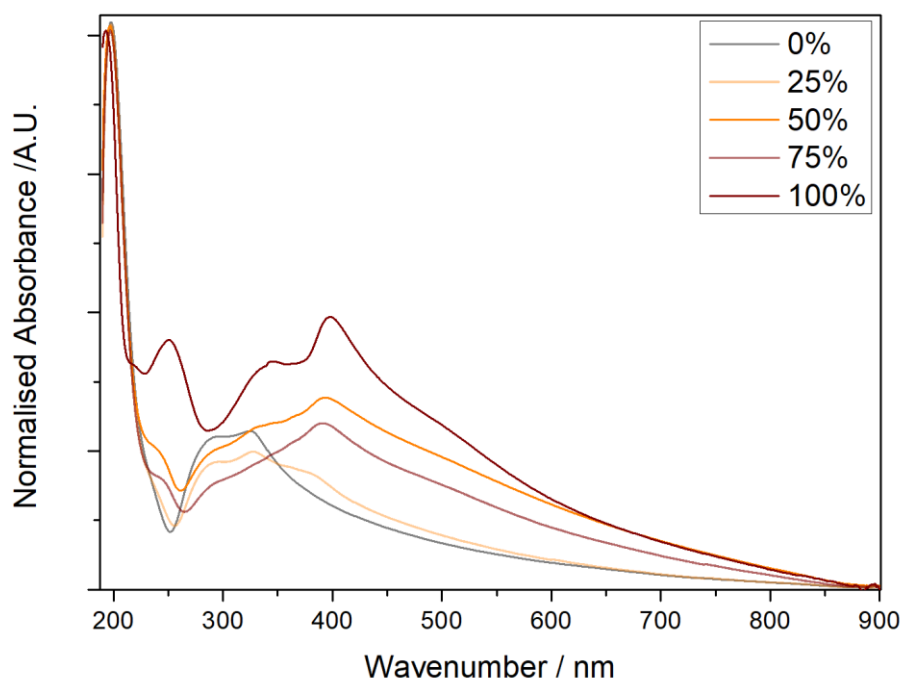


Figure S122: Normalised UV-Vis profiles of MTVs MOF dispersed in H₂O without light irradiation, showing the presence of contributions from *cis* and *trans* AzDC conformations. The *cis* contribution is more significant for MTV MOFs than for the pristine 100% AzDC. The spectra are normalized to the most intense signal at ca. 197 nm.

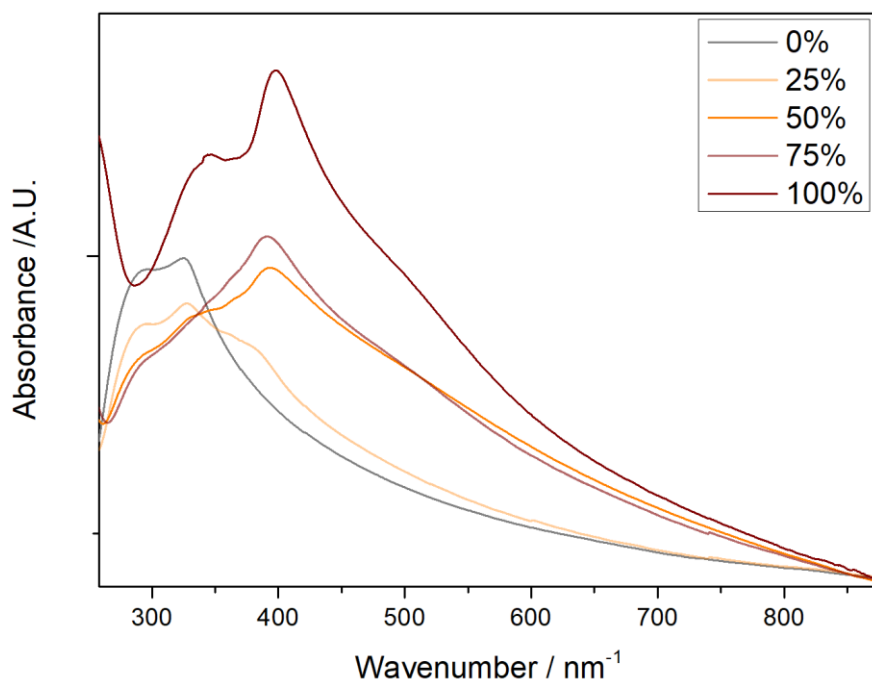


Figure S123: Normalised UV-Vis profile of MTVs MOF dispersed in H₂O without light irradiation, showing the presence of contributions from *cis* and *trans* AzDC conformations. The *cis* contribution is more significant for MTV MOFs than for the pristine 100% AzDC.

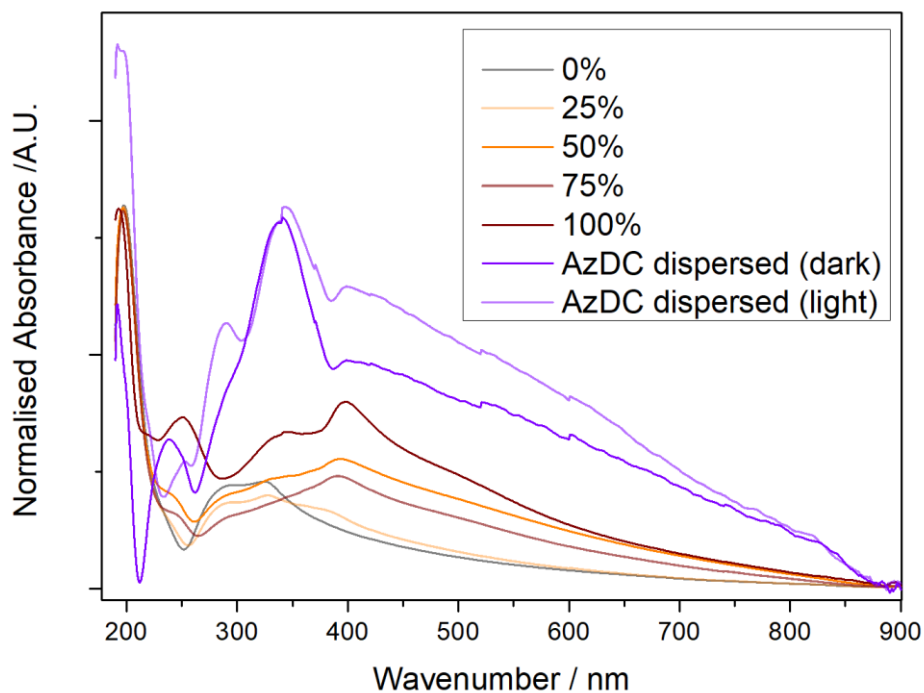


Figure S124: Normalised UV-Vis profile of MTVs MOF dispersed in H₂O without light irradiation, compared to AzDC in H₂O before and after light irradiation, showing the presence of contributions from *cis* and *trans* AzDC conformations. The *cis* contribution is more significant for MTV MOFs than for the pristine 100% AzDC.

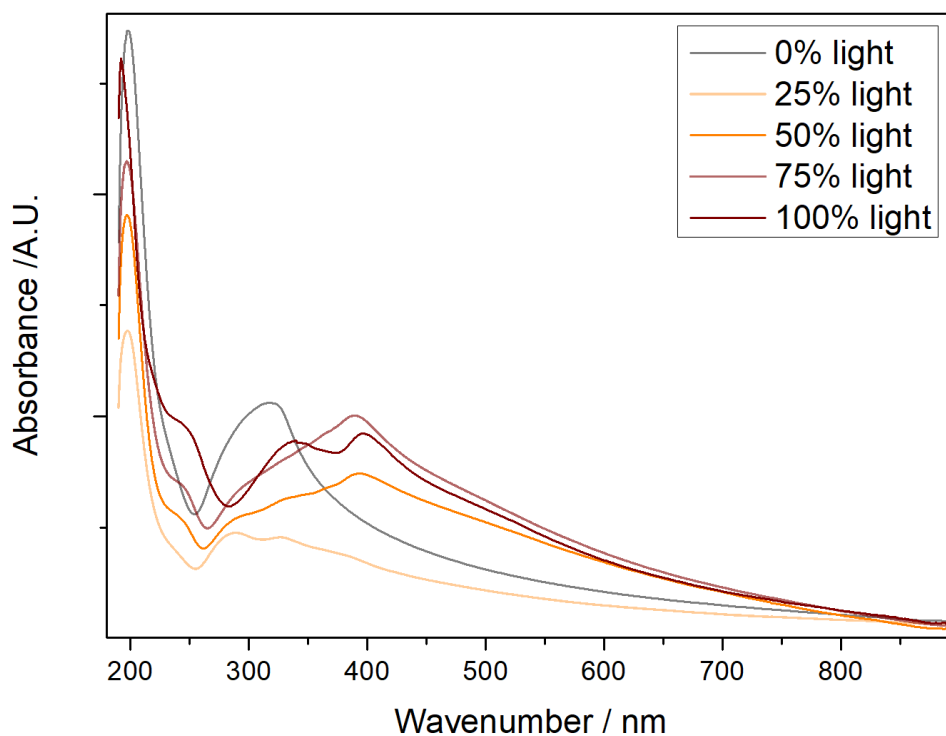


Figure S125: Raw UV-Vis profiles of MTVs MOF dispersed in H₂O after 2 hours of light irradiation, showing an increase in the presence of contributions from *cis* AzDC conformations. The bands attributed to AzDC agree with the percentage of AzDC present in the samples.

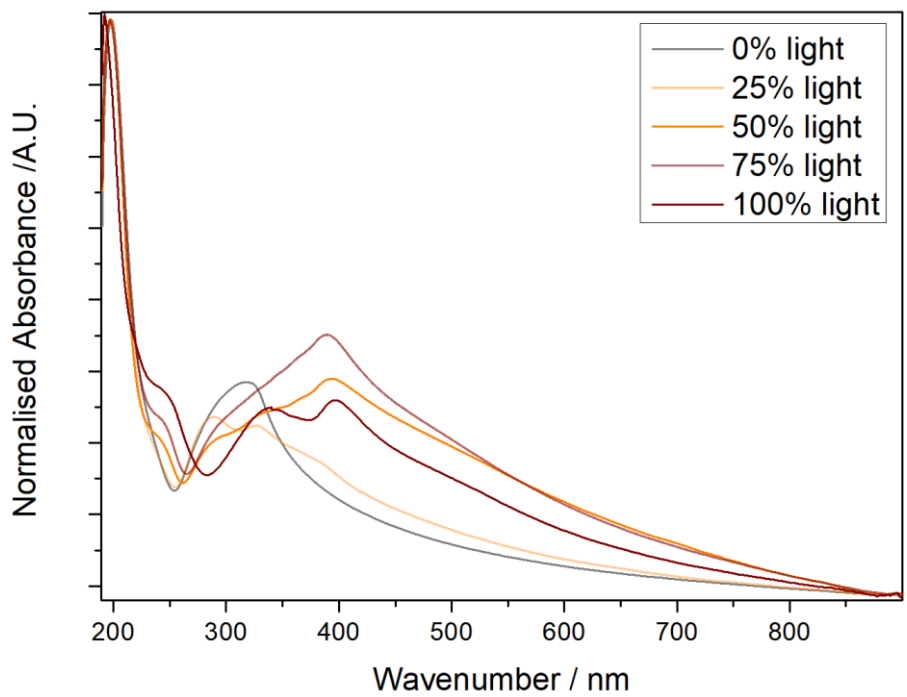


Figure S126: Normalised UV-Vis profiles of MTVs MOF dispersed in H₂O after 2 hours of light irradiation, showing an increase in the presence of contributions from *cis* AzDC conformations.

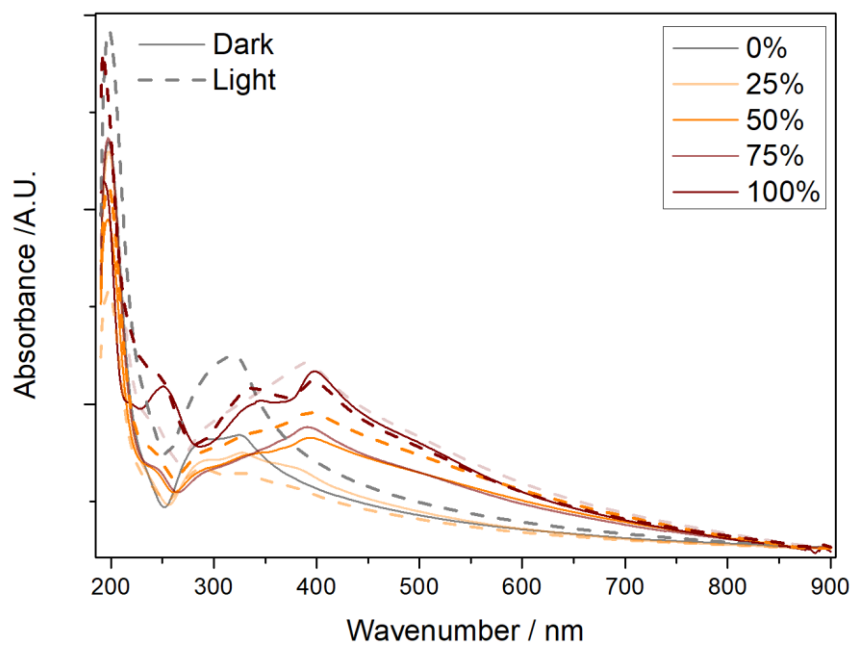


Figure S127: Comparison of raw UV-Vis profiles of MTVs MOF dispersed in H₂O before and after 2 hours of light irradiation, showing an increase in the presence of contributions from *cis* AzDC conformations.

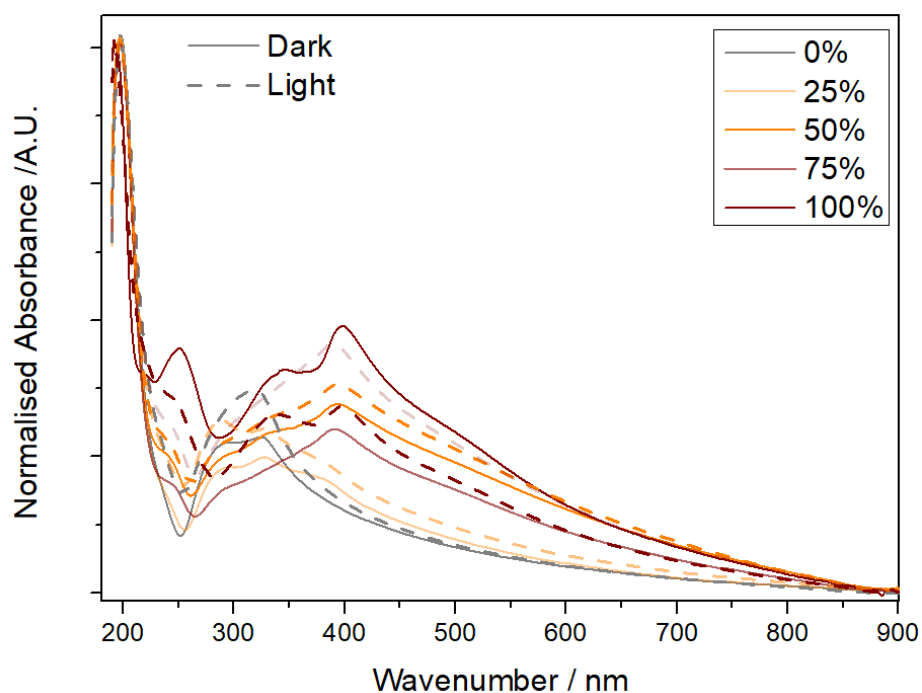


Figure S128: Comparison of normalised UV-Vis profiles of MTVs MOF dispersed in H₂O before and after 2 hours of light irradiation, showing an increase in the presence of contributions from *cis* AzDC conformations.

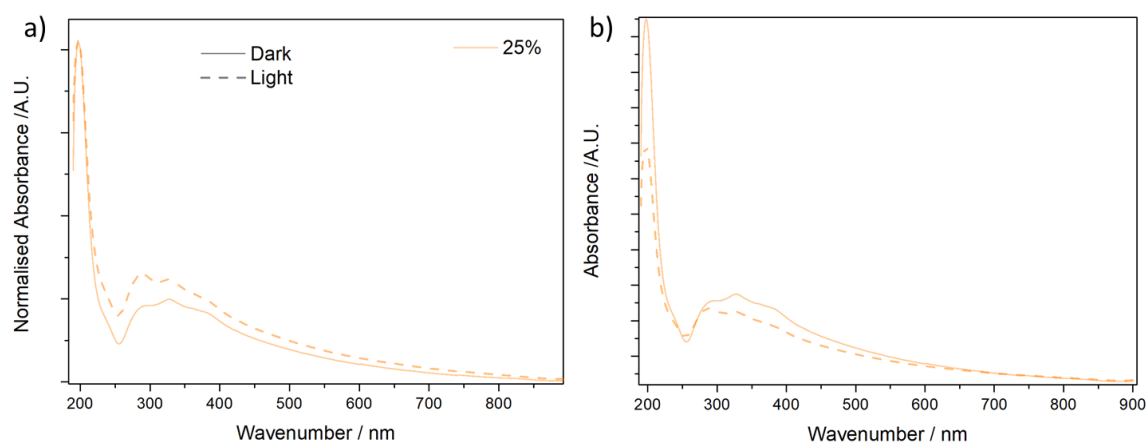


Figure S129: Comparison of a) normalised and b) raw UV-Vis profiles of 25% AzDC MOF dispersed in H₂O before and after 2 hours of light irradiation, showing an increase in the presence of contributions from *cis* AzDC conformations.

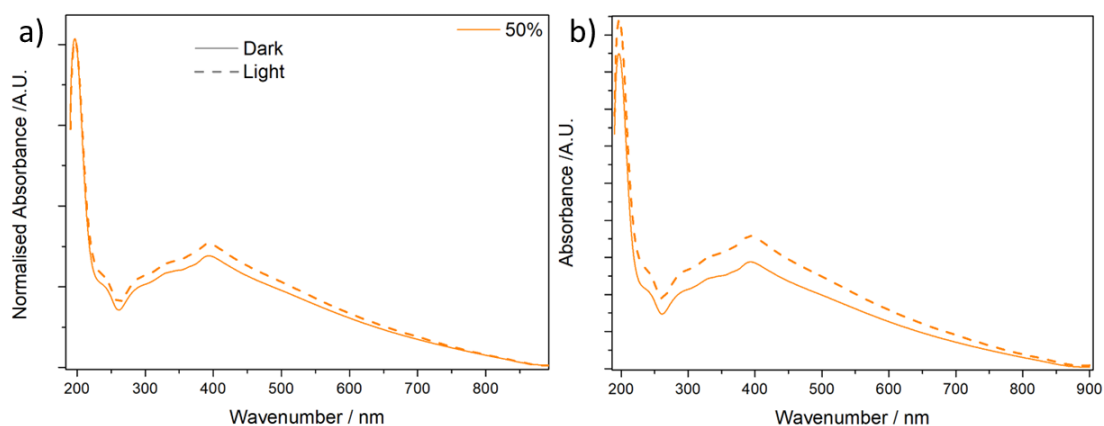


Figure S130: Comparison of a) normalised and b) raw UV-Vis profiles of 50% AzDC MOF dispersed in H₂O before and after 2 hours of light irradiation, showing an increase in the presence of contributions from *cis* AzDC conformations.

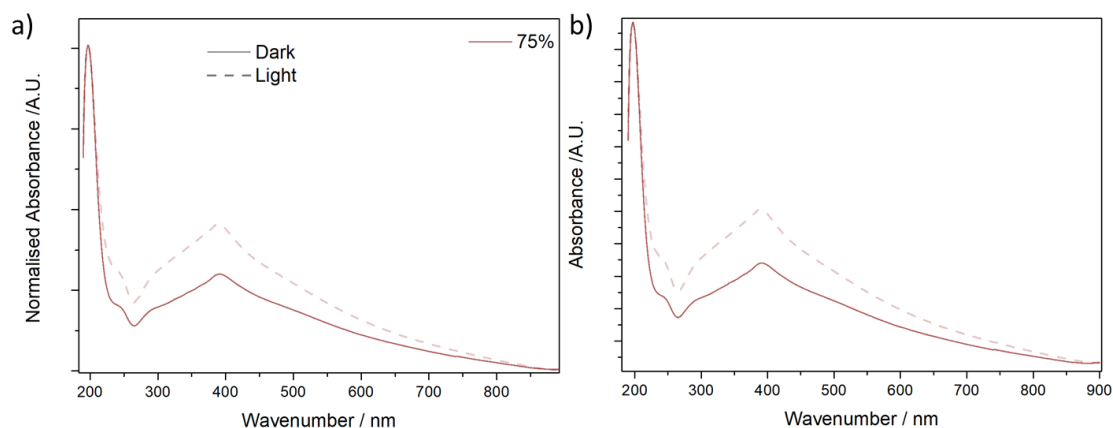


Figure S131: Comparison of a) normalised and b) raw UV-Vis profiles of 75% AzDC MOF dispersed in H₂O before and after 2 hours of light irradiation, showing an increase in the presence of contributions from *cis* AzDC conformations.

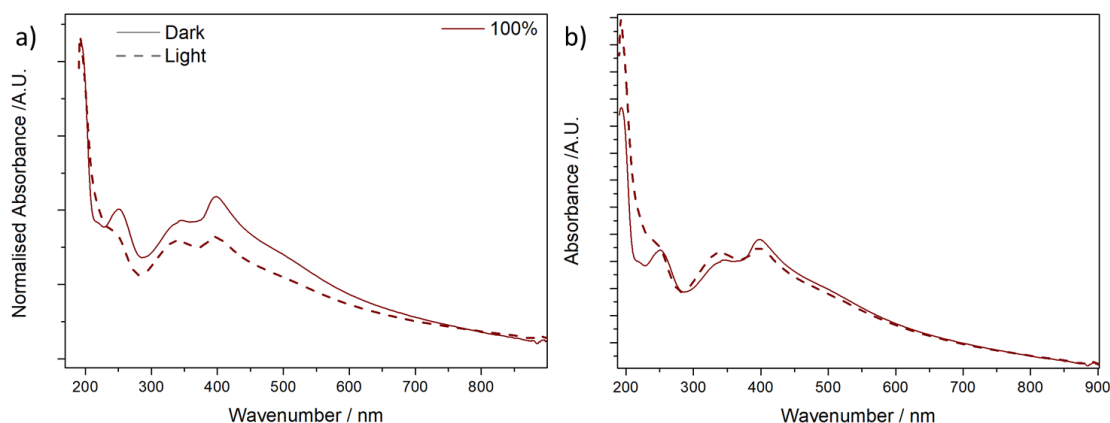


Figure S132: Comparison of a) normalised and b) raw UV-Vis profiles of 100% AzDC MOF dispersed in H₂O before and after 2 hours of light irradiation, showing an increase in the presence of contributions from *cis* AzDC conformations.

S.3.12 Photoluminescence

Photoluminescence (PL) emissions were measured at room temperature using a MonoSpec 27 Jarrel-Ash monochromator coupled with a Hamamatsu R446 photomultiplier using excited by a Innova Argon-ion laser. ($\lambda_{exc} = 350.7 \text{ nm}$; 2.57 eV . 200 mW , 2 minutes). The PL emission spectra were deconvoluted using Voigt-type functions with PeakFit™ software.

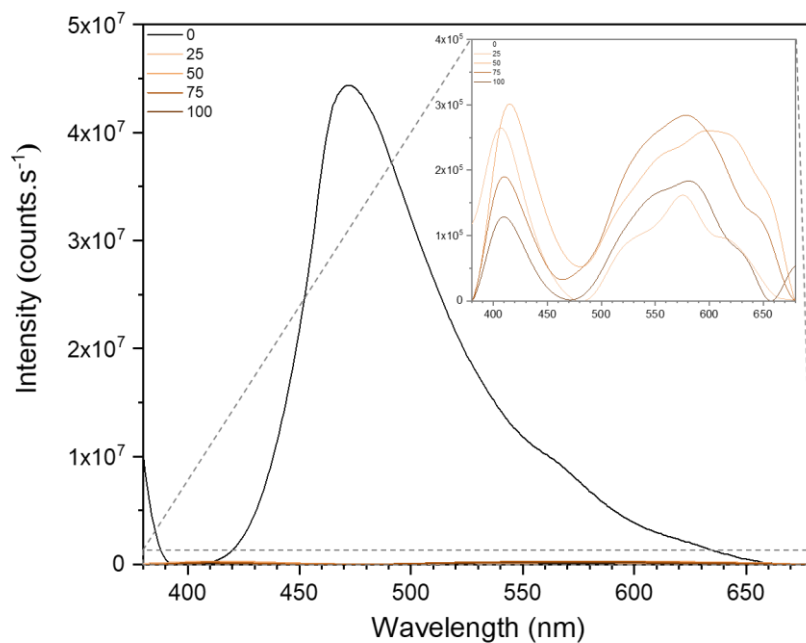


Figure S133: PL emission spectra for the samples.

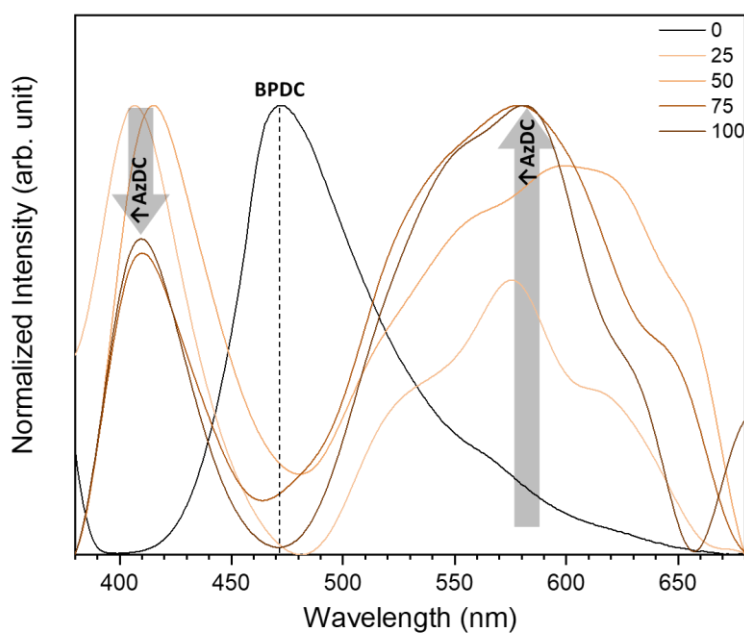


Figure S134: Normalized PL emission spectra for the samples.

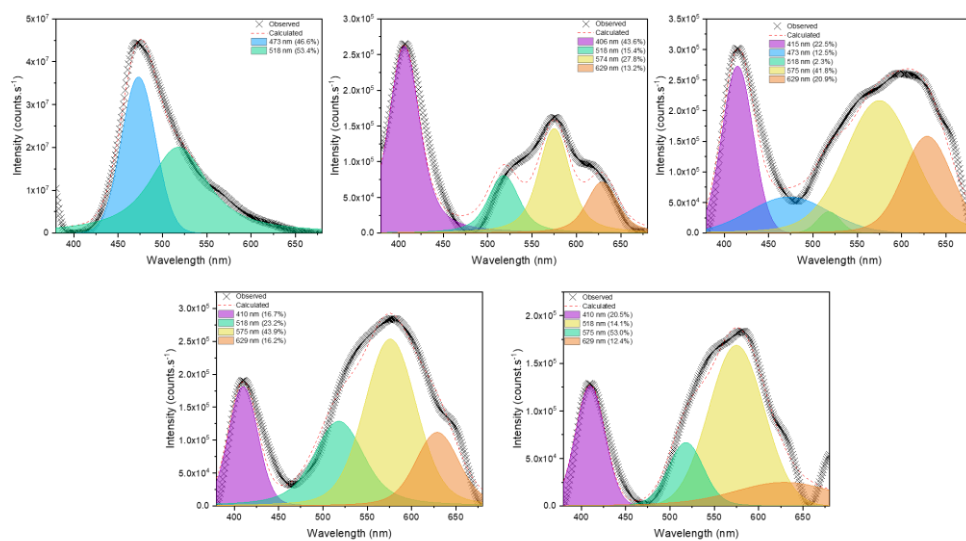


Figure S135. PL deconvolution spectra of the samples **A) 0%. B) 25%. C). 50%. D) 75%. E) 100%.**

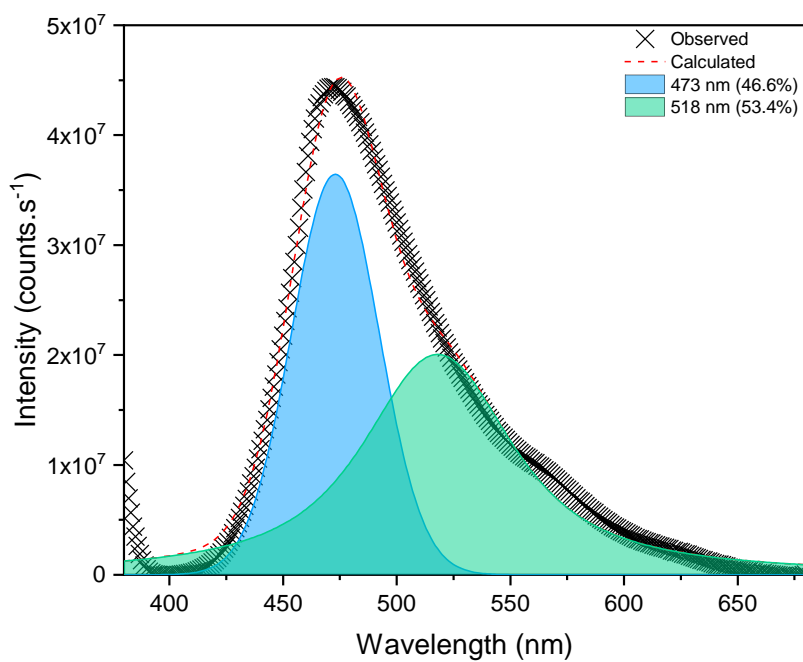


Figure S136. PL deconvolution spectra of 0% AzDC.

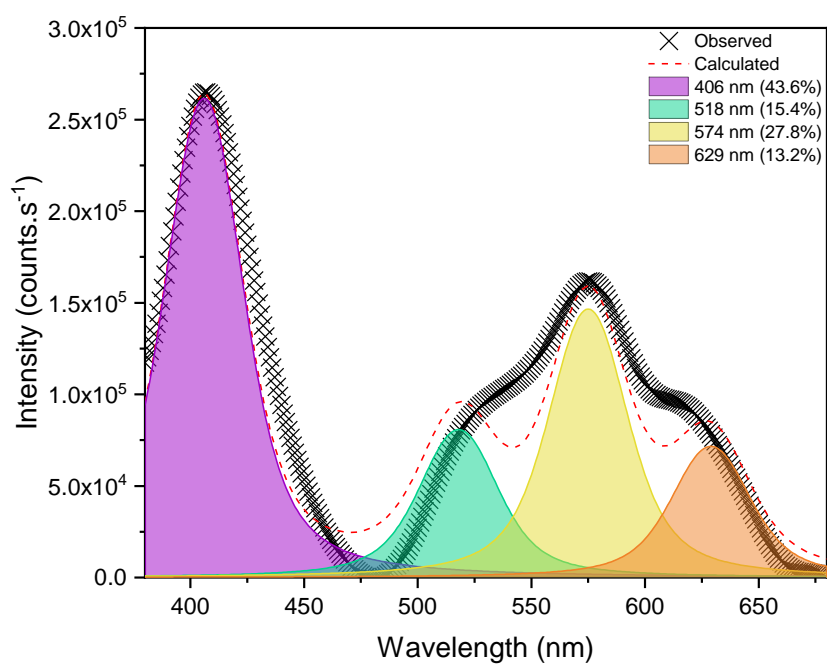


Figure S137. PL deconvolution spectra of 25% AzDC.

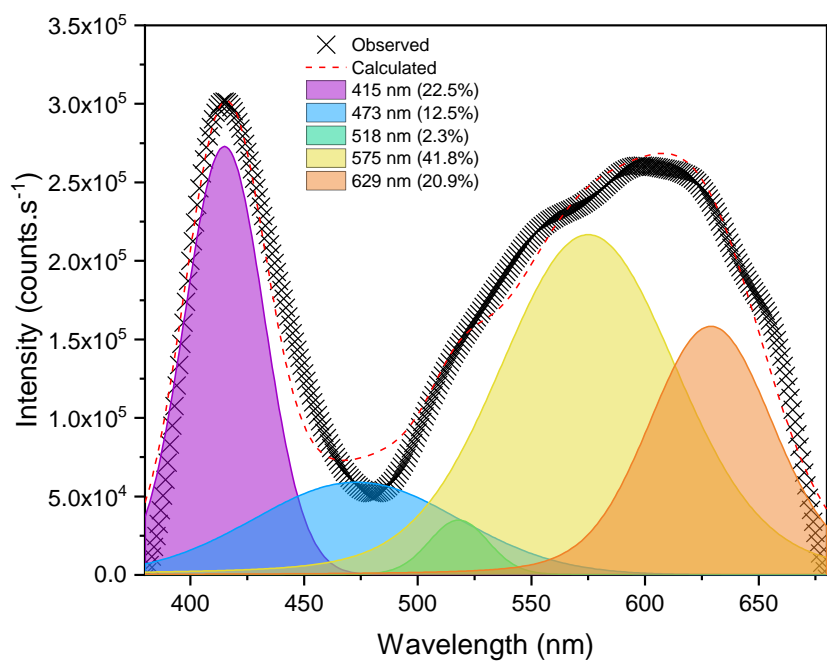


Figure S138. PL deconvolution spectra of 50% AzDC.

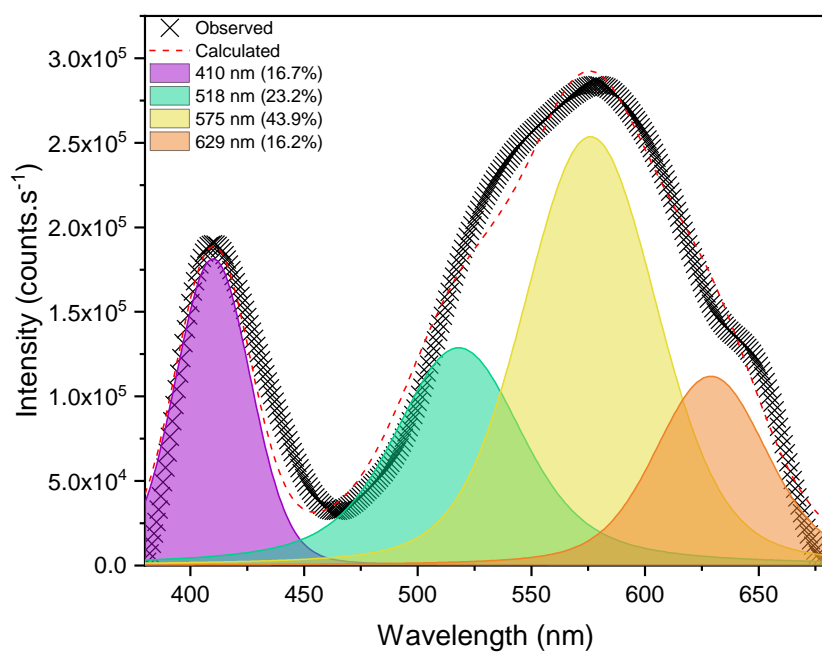


Figure S139. PL deconvolution spectra of 75% AzDC.

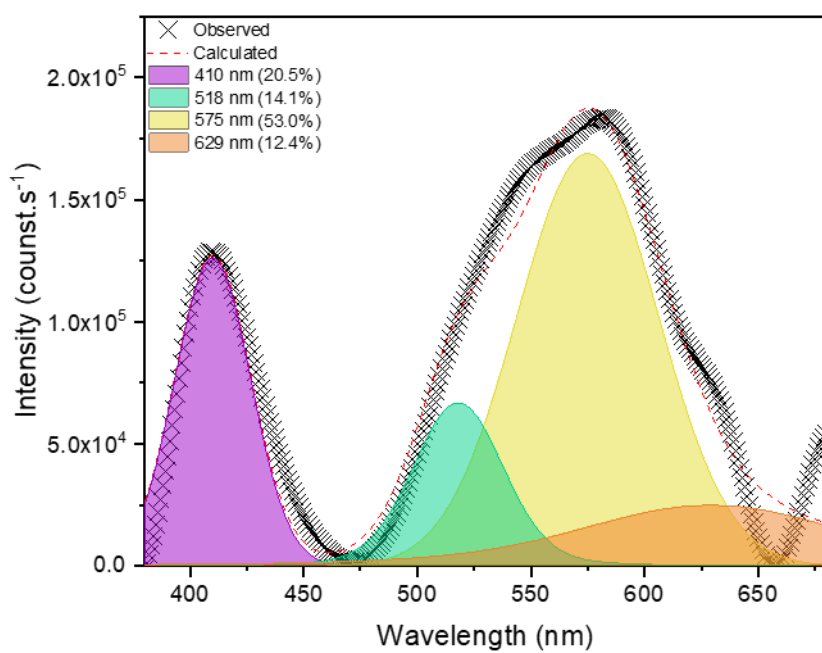


Figure S140. PL deconvolution spectra of 100% AzDC.

S.4.References

- [1] C. L. Hobday, R. J. Marshall, C. F. Murphie, J. Sotelo, T. Richards, D. R. Allan, T. Düren, F. Coudert, R. S. Forgan, C. A. Morrison, S. A. Moggach, T. D. Bennett, *Angew. Chem. Int. Ed.* **2016**, *55*, 2401.
- [2] T. D. Kühne, M. Iannuzzi, M. D. Ben, V. V. Rybkin, P. Seewald, F. Stein, T. Laino, R. Z. Khaliullin, O. Schütt, F. Schiffmann, D. Golze, J. Wilhelm, S. Chulkov, M. H. Bani-Hashemian, V. Weber, U. Borštnik, M. Taillefumier, A. S. Jakobovits, A. Lazzaro, H. Pabst, T. Müller, R. Schade, M. Guidon, S. Andermatt, N. Holmberg, G. K. Schenter, A. Hehn, A. Bussy, F. Belleflamme, G. Tabacchi, A. Glöß, M. Lass, I. Bethune, C. J. Mundy, C. Plessl, M. Watkins, J. VandeVondele, M. Krack, J. Hutter, *J. Chem. Phys.* **2020**, *152*, 194103.
- [3] J. Hutter, M. Iannuzzi, F. Schiffmann, J. VandeVondele, *Wiley Interdiscip. Rev.: Comput. Mol. Sci.* **2014**, *4*, 15.
- [4] J. P. Perdew, K. Burke, M. Ernzerhof, *Phys. Rev. Lett.* **1996**, *77*, 3865.
- [5] C. Hartwigsen, S. Goedecker, J. Hutter, *Phys. Rev. B* **1998**, *58*, 3641.
- [6] S. Goedecker, M. Teter, J. Hutter, *Phys. Rev. B* **1995**, *54*, 1703.
- [7] J. VandeVondele, J. Hutter, *J. Chem. Phys.* **2007**, *127*, 114105.
- [8] S. Grimme, J. Antony, S. Ehrlich, H. Krieg, *J. Chem. Phys.* **2010**, *132*, 154104.
- [9] I. A. Lázaro, *Eur. J. Inorg. Chem.* **2020**, 2020, 4284.
- [10] P. H. M. Andrade, M. Moreau, N. Henry, M. T. Bakouche, S. Duval, C. Volkringer, T. Loiseau, M. Hureau, A. Moissette, *J. Phys. Chem. C* **2023**, *127*, 4618.
- [11] C. M. Stuart, R. R. Frontiera, R. A. Mathies, *J. Phys. Chem. A* **2007**, *111*, 12072.
- [12] A. Modrow, D. Zargarani, R. Herges, N. Stock, *Dalton Trans.* **2011**, *40*, 4217.